5-2007

Spectroscopic Investigations of Complex Transition Metal Oxides

Jinbo Cao
University of Tennessee - Knoxville

Recommended Citation

Cao, Jinbo, "Spectroscopic Investigations of Complex Transition Metal Oxides. " PhD diss., University of Tennessee, 2007.
https://trace.tennessee.edu/utk_graddiss/132

To the Graduate Council:

I am submitting herewith a dissertation written by Jinbo Cao entitled "Spectroscopic Investigations of Complex Transition Metal Oxides." I have examined the final electronic copy of this dissertation for form and content and recommend that it be accepted in partial fulfillment of the requirements for the degree of Doctor of Philosophy, with a major in Chemistry.

Janice L. Musfeldt, Major Professor

We have read this dissertation and recommend its acceptance:

Charles Feigerle, Ziling Xue, Elbio Dagotto

Accepted for the Council:
Dixie L. Thompson

Vice Provost and Dean of the Graduate School

(Original signatures are on file with official student records.)

To the Graduate Council:

I am submitting herewith a dissertation written by Jinbo Cao entitled "Spectroscopic Investigation of Complex Transition Metal Oxides". I have examined the final electronic copy of this dissertation for form and content and recommend that it be accepted in partial fulfillment of the requirements for the degree of Doctor of Philosophy, with a major in Chemistry.

Janice L. Musfeldt

Major Professor

We have read this dissertation
and recommend its acceptance:

Charles Feigerle

Ziling Xue

Elbio Dagotto

Accepted for the Council:

Carolyn Hodges

Vice Provost and Dean of the
Graduate School

(Original signatures are on file with official student records.)

Spectroscopic Investigations of Complex Transition Metal Oxides

A Dissertation
Presented for the
Doctor of Philosophy Degree
The University of Tennessee, Knoxville

Jinbo Cao
May 2007

Acknowledgments

I would like to thank my advisor, Professor Janice L. Musfeldt, for her valuable guidance and advice, patience, encouragement, and support through my graduate studies at the University of Tennessee. Thank you for the time you have given and for being an ideal professional and scholarly role model.

I also thank Professor Charles Feigerle, Ziling Xue, and Elbio Dagotto for serving on my committee and reviewing my work.

I would like to express my acknowledgment to everybody in our research group during the past five years: Andi Barbour, Bo Luttrell, Jason Haraldsen, Jongwoo Choi, Luciana Vergara, Ram Rai, Roman Wesołowski, Sonal Brown, and Tatiana Brinzari, for their collaboration, encouragement, discussions, and assistance. I would also like to thank Alexandre Revcolevschi, Charlie C. Torardi, David J. Singh, Gavin Lawes, James R. Thompson, Jurek Krzystek, M. Stanley Whittingham, Mike Whangbo, Mircea Apostu, Natasha Chernova, Ramanathaan Suryanarayanan, Ronald Tackett, Samuel Lutta, Sergei Zvyagin, Stephen E. Nagler, Tanusri Dasgupta-Saha, Xing Wei, and Yongjie Wang for excellent collaboration and hard work on many projects.

Finally, I would like to express my special thanks to my parents, brother, and my wife for their love, care, and support.

Abstract

In this dissertation, I present spectroscopic studies of several model electronic and magnetic materials. Compounds of interest include VO_x nanoscrolls, $VOHPO_4 \cdot \frac{1}{2}H_2O$, and $(La_{0.4}Pr_{0.6})_{1.2}Sr_{1.8}Mn_2O_7$. These materials are attractive systems for the investigation of optical gap tuning, lattice and charge dynamics, spin-lattice-charge coupling, and hydrogen bonding effects. I measured the optical properties of VO_x nanoscrolls and the ion-exchanged derivatives to investigate the lattice and charge degrees of freedom. Selected V-O-V stretching modes sharpen and redshift with increasing amine size, which are microscopic manifestations of strain. We observed bound carrier localization in the metal exchanged nanoscrolls, indicating they are weakly metallic in their bulk form. I also investigated the variable temperature vibrational properties of single crystals of the S = 1/2 Heisenberg antiferromagnet $VOHPO_4 \cdot \frac{1}{2}H_2O$. In order to explain the activation and polarization dependence of the singlet-to-triplet gap in the far-infrared response, we invoke a dynamic Dzyaloshinskii-Moriya mechanism and we identify the low-energy phonons that likely facilitate this coupling. Vibrational mode splitting of $VOHPO_4 \cdot \frac{1}{2}H_2O$ also points toward a weak local symmetry breaking near 180 K, and the low-temperature redshift of V-O and H-O related modes demonstrates enhanced low-temperature hydrogen bonding. Finally, I measured the magneto-optical response of $(La_{0.4}Pr_{0.6})_{1.2}Sr_{1.8}Mn_2O_7$ to investigate the microscopic aspects of the magnetic field driven spin-glass insulator to ferromagnetic metal transition. Application of a magnetic field recovers the ferromagnetic state with an overall redshift of the electronic structure, growth of the bound carrier localization associated with ferromagnetic domains, development of a pseudogap, and softening of the Mn-O stretching and bending modes that indicate a structural change. By exploiting the electronic mechanisms, we can induce large high energy magnetodielectric contrast in $(La_{0.4}Pr_{0.6})_{1.2}Sr_{1.8}Mn_2O_7$. The dielectric contrast is over 100% near 0.8 eV at 4.2 K. Remnants of the transition also drive the high energy magnetodielectric effect at room temperature.

Contents

List of Tables

List of Figures

Chapter 1

Introduction: Emerging Problems in Transition Metal Oxides

Transition metal oxides display rich and fascinating properties including superconductivity, novel magnetism, unusual optical properties, and emerging engineering applications. These properties originate from low-dimensionality, a competition between near degenerate states, nanoscale charge and spin texture, the unique nature of the outer d electrons on transition metal centers, the special metal-oxygen bonding networks, structural phase transitions, and strong spin-lattice-charge coupling. [1–11] Competition between phases has become a central issue in complex oxides especially in presence of frustration or quenched disorder. Figure 1.1 shows several examples of how near degenerate states can be tuned with chemical composition, temperature, pressure, or applied magnetic field. Enormous physical property changes can therefore be achieved by small chemical and physical perturbations. Fundamental investigation of electrical, optical, and magnetic properties of model oxides that exhibit these effects can bring us closer to a microscopic understanding of these phenomena.

The discovery of nanoscale materials provides the exciting opportunity to investigate bulk versus nanoscale chemistry using molecular-level strain as the tuning

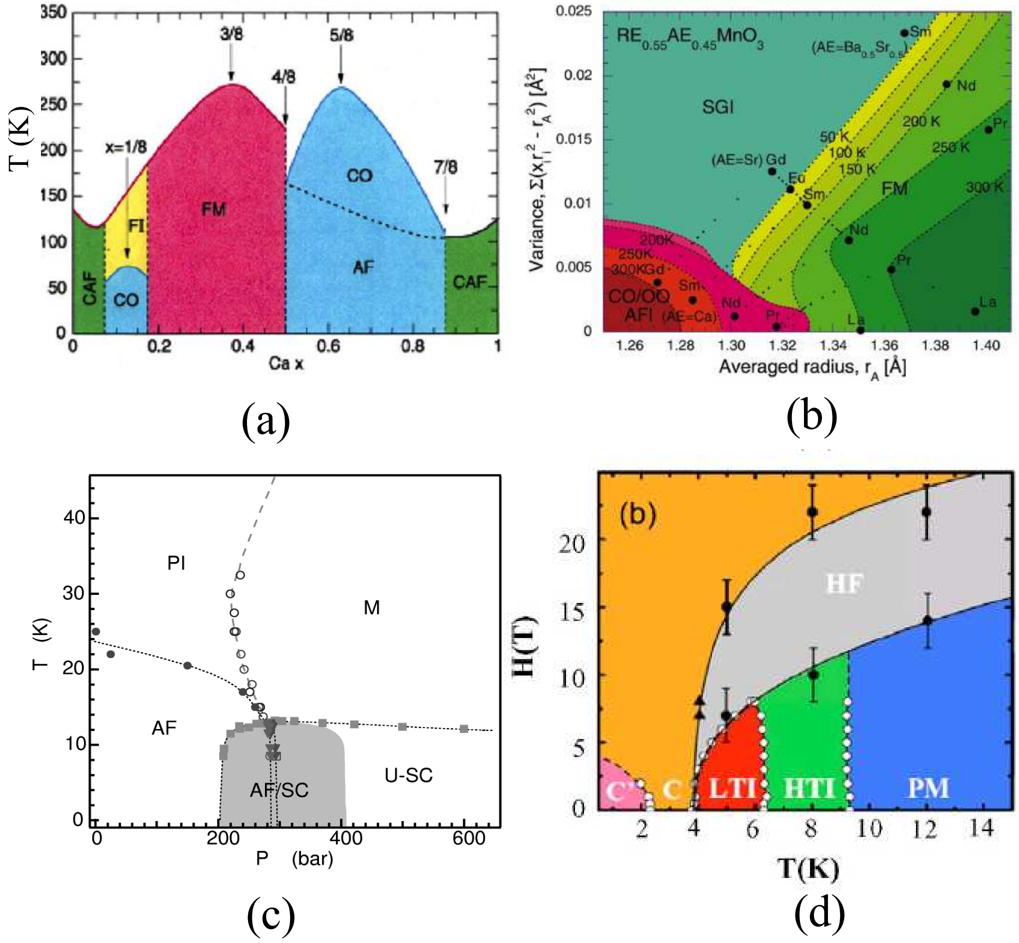

(a)

(b)

(c)

(d)

Figure 1.1: (a) The complex phase diagram of $La_{1-x}Ca_xMnO_3$ with an abundance of physical properties, such as ferromagnetism (F), antiferromagnetism (AF), paramagnetism (P), canted antiferromagnetism (CAF), colossal magnetoresistance (CMR), and charge ordering (CO). (after Ref. [10]) (b) The global phase diagram of $RE_{1-x}AE_xMnO_3$ (x=0.45) crystals in the plane of effective one-electron bandwidth (r_A) and the magnitude of quenched disorder (σ^2). (after Ref. [8]) (c) Temperature vs. pressure phase diagram of κ-$(ET)_2Cu[N(CN)_2]Cl$. The shaded area represents two regions of inhomogeneous phase coexistence. (after Ref. [11]) (d) $H - T$ phase diagram of $Ni_3V_2O_8$ for $H \parallel b$, emphasizing the cascade of phase transitions in the low temperature regime. (after Ref. [9])

parameter. [12] Recently, many inorganic nanoscale materials including MoS_2, WS_2, BN, TiO_2, $NiCl_2$, VO_x, and NbS_2 have been reported, with beautiful nanomorphologies, functional structures, and interesting lattice curvature. [12–24] Figure 1.2 displays representative TEM images of WS_2 nanoparticles, WS_2 nanotubes, vanadate nanoscrolls, and $BiFeO_3$ nanotubes. [25–28] These nanostructures offer molecular level control of size, shape, mechanical response, as well as unusual electric, optical, and magnetic properties due to confinement and finite length scale effects. The physics of nanomaterials, especially the experimental understanding of the energy and momentum relaxation processes by the lateral dimensions and the modified interaction between phonons and electrons by the nanostructures remains a rich area for investigation.

To develop a comprehensive understanding of low-dimensional and nanoscale transition metal oxides, a lot of careful and detailed experiments have to be done. Spectroscopies are one of the most powerful techniques that allow us to determine various physical properties of complex materials using electromagnetic radiation. Traditionally, the electromagnetic spectrum is divided into several well-known spectral regions, including radio waves, microwaves, infrared, optical (visible and ultraviolet light), x-rays, and γ-rays. They correspond to different energy scales and are sensitive to different kinds of excitations. Infrared and optical spectroscopies are perfect probes to investigate local microscopic properties, often the origin of unusual bulk or macroscopic properties. According to formal selection rules, there must be a change in electric dipole moment during the vibrational transition for a material to absorb infrared radiation. However, some of the symmetric oscillations or magnetic excitations can be activated due to symmetry breaking and various kinds of coupling mechanisms such as electron-phonon or spin-phonon coupling.

Careful spectroscopic measurements allow us to obtain information on the vi-

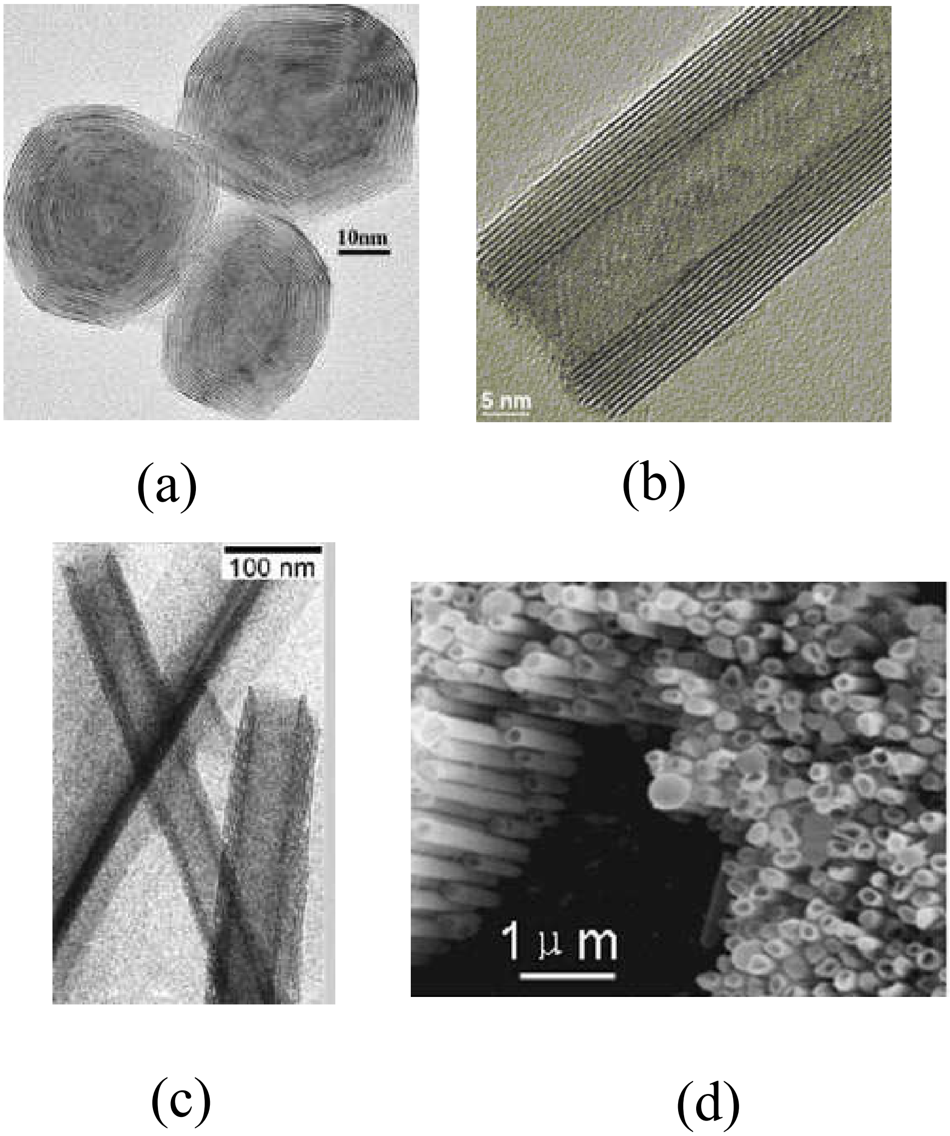

Figure 1.2: (a) TEM images of WS_2 nanoparticles (b) TEM images of WS_2 nanotubes (c) TEM images of vanadate nanoscrolls (d) TEM images of $BiFeO_3$ nanotubes. (after Ref. [25–28])

brational, electronic, and magnetic degrees of freedom. Vibrational modes can be excited to higher energy states by infrared light. Collective excitations for density waves and other broken-symmetry ground states can be observed in the far-infrared (or even microwave and radio frequency) range. The energy gap in superconductor is expected in an energy range comparable to the superconducting transition temperature, that is, between microwave frequencies and the far-infrared radiation. Both charge localization and Drude free carrier electronic response exist in the low energy electromagnetic regime. Many collective magnetic excitations in low-dimensional magnets could also be observed by far-infrared radiation, activated via spin-phonon coupling. Optical spectroscopy, at the same time, is a complementary technique for the investigation of charge degrees of freedom in complex oxides. If infrared and optical reflectance is done over a wide frequency range, a Kramers-Kronig analysis can correlate the measured data to the complex dielectric function, $\epsilon(\omega)$. [29] The dielectric tensor is directly related to the dispersive and lossy response of a solid. We can also extract the optical constants including optical conductivity ($\sigma_1(\omega)$), plasma frequency (ω_p), effective mass ($m^*(\omega)$), oscillator strength (S), and relaxation time ($\tau(\omega)$). These parameters often provide insight on the intrinsic properties of solids. Infrared and optical techniques have been successfully applied to investigate lattice and charge dynamics, structural phase transitions, and high energy magnetodielectric effects in complex solids. [9,30–37] Figure 1.3 displays an overview of the electromagnetic spectrum along with the physical properties investigated in the compounds of interest here.

In this dissertation, I present the reflectance and transmittance spectra of several model transition metal oxides over a wide spectral range as a function of both temperature as well as magnetic field. Compounds of interest have included VO_x nanoscrolls, $VOHPO_4{\cdot}\frac{1}{2}H_2O$, and $(La_{0.4}Pr_{0.6})_{1.2}Sr_{1.8}Mn_2O_7$. [38–44] My analysis of

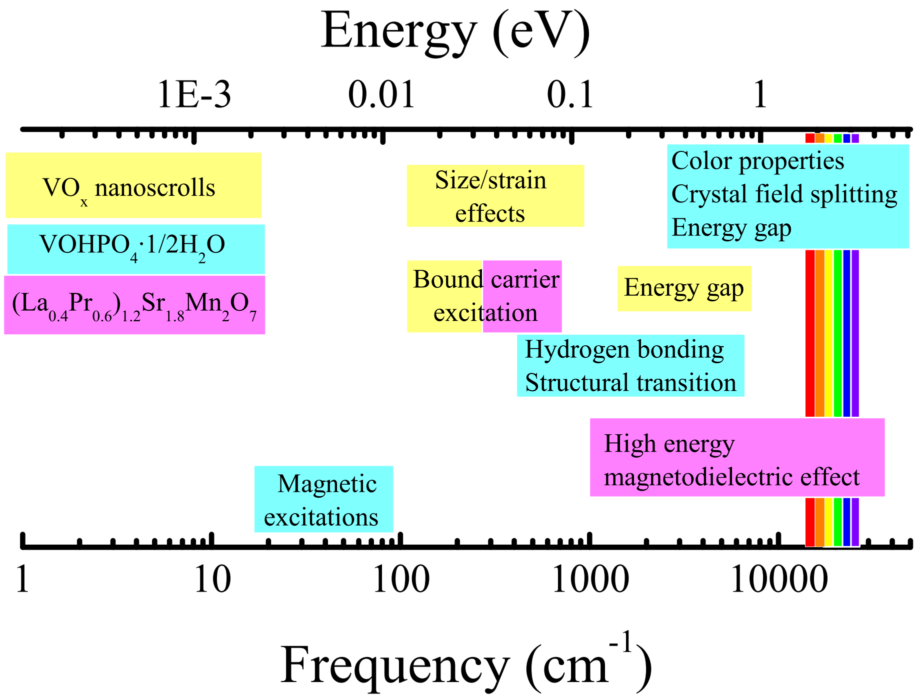

Figure 1.3: The electromagnetic spectrum showing the compounds of interest in this dissertation and the physical properties investigated. [38–44]

the experimental results concentrates on optical gap tuning, lattice and charge dynamics, hydrogen bonding, spin-lattice-charge coupling, and high energy magnetodielectric effects. These scientific problems and our contributions are summarized in Table 1.1.

Among the transition metal oxides, vanadates show particularly rich chemistry due to the tunable vanadium oxidation state and flexible coordination environment. [45] The nanoscrolls, (amine)$_y$VO$_x$ of interest here are mixed-valent with x $\sim$ 2.4. [26, 27] The size of the amine or diamine template determines scroll winding, providing an opportunity to tune the size of these materials. The exact crystal structure has not been completely resolved and is thought to be related to BaV_7O_{16}. [46] Scrolled vanadates exhibit very interesting physical properties including a large spin gap and potential battery as well as optical limiting applications. Recently, electron- and hole-doped vanadium oxide nanoscrolls were also reported to be 300 K ferromagnets, raising fundamental questions about their magnetic exchange mechanism. [47] Here, we are especially interested in the chemical structure and physical property correlations as well as charge and lattice dynamics in these novel nanoscale materials. In the pristine nanoscrolls, the electronic structure strongly resembles that of other bulk, low-dimensional, and molecular vanadates. [38] The 1.2 eV band is assigned as a superposition of V^{4+} $d \rightarrow d$ and $V^{4+} \rightarrow V^{5+}$ charge transfer excitations, and the features above 3 eV are attributed to O $2p \rightarrow$ V $3d$ charge transfer excitations. The 5 eV excitation shows a modest sheet distance dependence, redshifting with increasing sheet distance. We find that the optical gap is $\sim$0.56 eV at room temperature and $\sim$0.65 eV at 4.2 K. It does not depend systematically on tube size. At the same time, selected V-O-V stretching modes sharpen and redshift with increasing sheet distance. We attribute these trends to the microscopic manifestations of strain, which changes with curvature. [38] We unexpectedly observe a bound carrier excitation in

Table 1.1: Scientific problems and my contributions in this dissertation

Scientific Problems	Model Compound Used to Investigate the Scientific Problems	Our Scientific Findings
• Bulk vs. nanoscale dynamics • Structure-property correlations • Metal substitution effects	• Vanadate nanoscrolls • Refs. [38–40]	• Optical signature of molecular level strain effects • 1.2 eV band arising from superposition of V^{4+} $d \rightarrow d$ and $V^{4+} \rightarrow V^{5+}$ charge transfer excitations • Weakly metallic in ion substituted compounds • Localized bound carrier excitation in ion substituted compounds rather than Drude free carrier response due to inhomogeneous charge disproportionation and electron-electron correlation effects
• Spin-phonon coupling • Structural transition • Hydrogen bonding	• $VOHPO_4 \cdot \frac{1}{2}H_2O$ • Refs. [41, 42]	• Magnetic excitations activated via Dzyaloshinskii-Moriya interactions • Weak local symmetry breaking near 180 K • Enhance low-temperature hydrogen bonding near 180 K, driving phase transition • ~1.5 eV color band derived from crystal field splitting of the V^{4+} $3d$ levels, with low temperature trends consistent with improved hydrogen bonding
• Spin-lattice-charge coupling • Controlling disorder near phase boundary • High energy magnetodielectric effects	• $(La_{0.4}Pr_{0.6})_{1.2}Sr_{1.8}Mn_2O_7$ • Refs. [43, 44]	• Overall redshift of electronic structure, growth of bound carrier localization, and softening of Mn-O stretching and bending modes through spin-glass insulator to ferromagnetic metal transition • Exploiting magnetic field driven metal to insulator transition is a better way to achieve high energy magnetodielectric effect • Room temperature high energy magnetodielectric effects • High energy magnetodielectric effect over 100% near 0.8 eV at low temperature

the metal substituted nanoscrolls rather than a metallic response that was predicted by theory. [47] This bound carrier excitation is localized in the far-infrared due to a combination of inhomogeneous charge disproportionation and electron-electron correlation effects. We propose an alternate band filling picture that accounts for the charge localization. Analysis of the vibrational properties shows that the aforementioned V-O-V equatorial stretching modes redshift with ion substitution, indicating that ion exchange modifies both the local curvature and charge environment. Charge effects also redshift several high energy electronic excitations. [40]

The low-dimensional vanadates $VOHPO_4{\cdot}\frac{1}{2}H_2O$ attracted our attention as model system for fundamental investigations of low-dimensional quantum spin interactions and practical applications in the area of catalysis. [48–53] $VOHPO_4{\cdot}\frac{1}{2}H_2O$ is a two-dimensional material. Each layer consists of face-sharing vanadium oxide octahedra, corner-linked by hydrogen phosphate tetrahedra in the *ab*-plane. Here, we are mostly interested in the spin-phonon coupling, structural transition, and hydrogen bonding effects. We invoke a dynamic Dzyaloshinskii-Moriya mechanism to explain the activation and polarization dependence of the singlet-to-triplet gap in the far-infrared response, and we identify the low-energy phonons that likely facilitate this coupling. Vibrational mode splitting of the title compound also points toward a weak local symmetry breaking near 180 K, and the low-temperature redshift of V-O and H-O related modes demonstrates enhanced low-temperature hydrogen bonding. [41] We also investigate the optical properties of $VOHPO_4{\cdot}\frac{1}{2}H_2O$ at variable temperature. $VOHPO_4{\cdot}\frac{1}{2}H_2O$ displays a strong color band centered at $\sim$1.5 eV that derives from excitations between crystal field split $3d$ levels of the V^{4+} centers. These features redshift with decreasing temperature, indicative of enhanced low temperature hydrogen bonding between layers.

Substituted perovskite manganites have attracted considerable attention due to their exotic magnetic, electronic, and optical properties. These properties derive from the many competing ground states of the complex phase diagram, strong coupling across different energy scales, and the presence of an inhomogeneous texture. [4, 6, 7] The manganite of interest here is $(La_{0.4}Pr_{0.6})_{1.2}Sr_{1.8}Mn_2O_7$, which crystallizes in a body-centered tetragonal structure (space group $I4/mmm$). [54, 55] It is well-suited for fundamental magnetodielectric properties investigations, [37, 56, 57] extending the Tomioka-Tokura electronic phase diagram picture, [8] and testing oscillator strength sum rules. [58, 59] We measured the magneto-optical response of $(La_{0.4}Pr_{0.6})_{1.2}Sr_{1.8}Mn_2O_7$ in order to investigate the microscopic aspects of the magnetic field driven spin-glass insulator to ferromagnetic metal transition. Application of a magnetic field recovers the ferromagnetic state with an overall redshift of the electronic structure, growth of the bound carrier localization associated with ferromagnetic domains, development of a pseudogap, and softening of the Mn-O stretching and bending modes that indicate a structural change. We discuss field- and temperature-induced trends within the framework of the Tomioka-Tokura global electronic phase diagram picture and suggest that controlled disorder near a phase boundary can be used to tune the magnetodielectric response. [43] By exploiting the electronic mechanisms, we observed high energy magnetodielectric effect response in $(La_{0.4}Pr_{0.6})_{1.2}Sr_{1.8}Mn_2O_7$, behavior that results from a magnetic field driven spin-glass insulator to ferromagnetic metal transition. The size of the dielectric contrast depends on energy and it is as large as $\sim$100% near 0.8 eV. Remnants of the transition also drive the high energy magnetodielectric effect at room temperature. [44]

The remainder of the dissertation is organized as follows. The second chapter discusses the infrared and optical techniques, and the interaction of light with solids. Chapter 3 gives a literature survey of selected interesting properties of transition metal oxides. Chapter 4 presents our optical investigations of vanadate nanoscrolls, focusing on strain and doping effects. Chapter 5 is devoted to the experimental and theoretical results of $VOHPO_4 \cdot \frac{1}{2}H_2O$, focusing on hydrogen bonding, spin-phonon coupling, and magnetic excitations. Chapter 6 details the magneto-optical investigation of the field-induced spin-glass insulator to ferromagnetic metal transition in the bilayer manganite $(La_{0.4}Pr_{0.6})_{1.2}Sr_{1.8}Mn_2O_7$, with the goal of understanding phase competition, spin-charge-lattice coupling, controlling disorder near the phase boundary, and the high energy magnetodielectric effect. Chapter 7 summarizes my work.

Chapter 2

Experimental and Theoretical Techniques

2.1 Introduction

When a solid is subject to electromagnetic radiation of intensity I_0, the intensity of this beam is attenuated after passing through the sample. Several processes, such as absorption, reflectance, and scattering, contribute to the attenuation. Infrared and optical spectroscopies analyze reflectance or transmittance of the sample as a function photon energy. If infrared and optical reflectance is done over a wide frequency range, a Kramers-Kronig analysis can correlate the measured data to the dielectric function, $\epsilon(\omega)$. [29] At the same time, the dielectric response is directly related to the electronic structure and lattice dynamics of a solid. We can extract the optical constants including optical conductivity ($\sigma_1(\omega)$), plasma frequency (ω_p), effective mass ($m^*(\omega)$), oscillator strength (S), and relaxation time ($\tau(\omega)$). These parameters often provide insight on the intrinsic properties of solids. Experimentally, the reflectance ($R(\omega)$) and/or transmittance ($T(\omega)$) are often carried out with combination of several light sources, spectrometers, and detectors. This chapter will describe the experimental and theoretical techniques used in our spectroscopic work.

2.2 Optical Properties of Solids

2.2.1 Maxwell's Equation and Optical Constants

The theoretical description of the interaction of radiation with matter and the analysis of the experimental results are based on Maxwell's equations and on their solution for time-varying electric and magnetic fields. In the long wavelength limit, the propagation of electromagnetic wave can be described by the macroscopic Maxwell's equations: [29]

$$\nabla \cdot \mathbf{D} = 4\pi\rho^{ext} \tag{2.1}$$

$$\nabla \times \mathbf{E} = -\frac{1}{c}\frac{\partial \mathbf{B}}{\partial t} \tag{2.2}$$

$$\nabla \cdot \mathbf{B} = 0 \tag{2.3}$$

$$\nabla \times \mathbf{H} = \frac{1}{c}\frac{\partial \mathbf{D}}{\partial t} + \frac{4\pi}{c}\mathbf{J}^{cond} + \frac{4\pi}{c}\mathbf{J}^{ext}, \tag{2.4}$$

where $\mathbf{E}$ and $\mathbf{H}$ are the electric and magnetic fields, $\mathbf{D}$ and $\mathbf{B}$ are the displacement field and magnetic induction, $\mathbf{J}^{cond}$ are free-current density, and $\mathbf{J}^{ext}$ and ρ^{ext} are current and charge density induced by external force. In an anisotropic medium, the polarization and induced currents generally lie in a direction different from that of the electric field. We can represent the dielectric function as a tensor to solve this problem. For simplicity, in the isotropic media and within the linear approximation, we can assume

$$\mathbf{D} = \epsilon \mathbf{E} \tag{2.5}$$

$$\mathbf{B} = \mu \mathbf{H} \tag{2.6}$$

$$\mathbf{J}^{cond} = \sigma \mathbf{E}, \tag{2.7}$$

where ϵ is the dielectric function, and σ is the optical conductivity, and μ is the magnetic permeability. Here both ϵ and σ are scalar quantities rather than tensors for the isotropic and homogeneous media.

The complex refraction index [29]

$$N(\omega) = n(\omega) + i\kappa(\omega),$$

and the complex dielectric function

$$\epsilon(\omega) = \epsilon_r(\omega) + i\epsilon_i(\omega),$$

where n and κ are the refractive index and the extinction coefficient, and $N(\omega)$ and $\epsilon(\omega)$ are related by the following equation

$$N(\omega) = \sqrt{\epsilon(\omega)}. \tag{2.8}$$

Finally, solving Maxwell's equation 2.1-2.4 for a plane wave

$$\mathbf{E} = \mathbf{E_0} exp[i(\mathbf{q} \cdot \mathbf{x} - \omega t)] \tag{2.9}$$

gives the following relation,

$$\epsilon(\omega) = 1 + \frac{i\sigma(\omega)}{\omega\epsilon_0}, \tag{2.10}$$

Table 2.1: Relationships between the various response function $\epsilon(\omega)$, $\sigma(\omega)$, and $N(\omega)$

Dielectric constant $\epsilon(\omega)$	Conductivity $\sigma(\omega)$	Refractive index $N(\omega)$
$\epsilon = \epsilon_1 + i\epsilon_2$ $\sigma_1 = \frac{\omega\epsilon_2}{4\pi}$ $\sigma_2 = (1 - \epsilon_1)\frac{\omega}{4\pi}$ $n = (\frac{1}{2}((\epsilon_1^2 + \epsilon_2^2)^{1/2} + \epsilon_1))^{1/2}$ $k = (\frac{1}{2}((\epsilon_1^2 + \epsilon_2^2)^{1/2} - \epsilon_1))^{1/2}$	$\epsilon_1 = 1 - \frac{4\pi\sigma_2}{\omega}$ $\epsilon_2 = \frac{4\pi\sigma_1}{\omega}$ $\sigma = \sigma_1 + i\sigma_2$ $n = (\frac{1}{2}(((1 - \frac{4\pi\sigma_2}{\omega})^2 + (\frac{4\pi\sigma_1}{\omega})^2)^{1/2} + (1 - \frac{4\pi\sigma_2}{\omega})))^{1/2}$ $n = (\frac{1}{2}(((1 - \frac{4\pi\sigma_2}{\omega})^2 + (\frac{4\pi\sigma_1}{\omega})^2)^{1/2} - (1 - \frac{4\pi\sigma_2}{\omega})))^{1/2}$	$\epsilon_1 = n^2 - k^2$ $\epsilon_2 = 2nk$ $\sigma_1 = \frac{nk\omega}{2\pi}$ $\sigma_2 = (1 - n^2 + k^2)\frac{\omega}{4\pi}$ $N = n + ik$

or

$$\epsilon(\omega) = \epsilon_1(\omega) + i\epsilon_2(\omega) = \epsilon_1(\omega) + \frac{4\pi i\sigma_1(\omega)}{\omega} \tag{2.11}$$

where $\sigma_1(\omega)$ is the frequency dependent (optical) conductivity. In the case of weak absorption, $\epsilon_1 = n^2 - k^2 \approx n^2$, and $v \approx c/n$, the absorption coefficient α can be written as

$$\alpha = \frac{4\pi\sigma}{\epsilon_1 v} = \frac{4\pi\sigma}{nc} \tag{2.12}$$

Table 2.1 lists the relationships between the various response functions.

2.2.2 Kramers-Kronig Analysis and Sum Rules

The dielectric function can be derived by Kramers-Kronig transformation of the reflectance spectrum.

The reflectivity is defined as:

$$r = \frac{E_r}{E_i} = \frac{N_a - N_b}{N_a + N_b}, \tag{2.13}$$

where N_a and N_b are refraction indices of medium a and b. When the light is incident from vacuum onto a sample surface at normal incident, which means that N_a=1, and N_b=N=n+$i\kappa$, the power reflectance is given by

$$R(\omega) = rr^* = \frac{(1-n)^2+\kappa^2}{(1+n)^2+\kappa^2}. \tag{2.14}$$

The power reflectance $R(\omega)$ and phase-dispersion shift $\phi(\omega)$ are related by Kramers-Kronig transformation: [29]

$$\phi(\omega) = \frac{\omega}{\pi}\int_0^\infty \frac{lnR(\omega) - lnR(\omega^{'})}{\omega'^2-\omega^2}d\omega^{'}. \tag{2.15}$$

Since reflectivity

$$r = \sqrt{R}e^{i\phi}, \tag{2.16}$$

and combining Eqs. 2.14, 2.15, and 2.16, n and k can be determined by $R(\omega)$ and $\phi(\omega)$. Then from Eqs. 2.8 and 2.11, the real part of dielectric function and the real part of optical conductivity can be determined:

$$\epsilon_1 = n^2 - k^2 \tag{2.17}$$

$$\sigma_1 = \frac{\omega\epsilon_2}{4\pi} = \frac{\omega nk}{2\pi}. \tag{2.18}$$

In Eq. 2.15, the integration is from zero to ∞. Since our optical measurements usually cover the frequency range from far-infrared to ultraviolet, a proper extrapolation should be used. In this dissertation, in the low-frequency range, Hagen-Rubens relation, $R(\omega) = 1 - (2\omega/\pi\sigma_0)^{1/2}$, is used for metallic material; the low-frequency reflectance was extrapolated as a constant for semiconductor; in the high frequency, the optical response is mimicked by $R \sim \omega^{-\alpha}$, where α varies from 0-4 and can be determined by comparing the absorption and calculated optical conductivity.

Together with physical arguments about the behavior of the response in certain limits, the Kramers-Kronig relation can also be used to derive sum rules. That is

$$\int_0^\infty \omega' Im(-1/\epsilon(\omega'))d\omega' = 1/2\pi\omega_p^2. \tag{2.19}$$

2.2.3 Lorentz and Drude Models

The dielectric function can be modeled by three parts:

$$\epsilon = \epsilon_\infty + \epsilon_{free} + \epsilon_{bound}, \tag{2.20}$$

where ϵ_{free} is the contribution from free electrons, and ϵ_{bound} is contributed from bound carriers.

The model to describe the contribution of free carriers to the dielectric function is called the Drude model, and the contribution of bound electrons is modeled with a Lorentz oscillator. Both models are essentially deducted from the dielectric function of a harmonic oscillator with frequency ω_0 responding to an electromagnetic field, with ω_0=0 for the Drude model. [29]

The form of the Lorentz dielectric function is:

$$\epsilon = \epsilon_\infty + \sum \frac{\omega_{pj}^2}{\omega_j^2 - \omega^2 - i\omega\gamma_i}_j, \tag{2.21}$$

where the plasma frequency

$$\omega_p = \sqrt{\frac{4\pi N e^2}{m}}, \tag{2.22}$$

and ω_j and γ_j are the resonant frequency and damping constant, respectively, of the j^{th} Lorentzian oscillators.

From Eqs. 2.21, taking ω_j=0, we have the form of the Drude dielectric function

$$\epsilon_D(\omega) = \epsilon_\infty - \frac{\omega_p^2}{\omega^2 + \frac{i\omega}{\tau}} \tag{2.23}$$

where τ=1/γ is the mean free time between collisions.

2.3 Spectrometers

2.3.1 Bruker IFS 113v Fourier Transform Infrared Spectrometer

The majority of the far-infrared (30-600 cm^{-1}) and middle infrared (500-5000 cm^{-1}) reflectance and transmittance spectra in this work were obtained by using Bruker IFS 113v Fourier Transform Infrared (FTIR) spectrometer. The schematic of the optical components of the Bruker IFS 113v FTIR spectrometer is illustrated in Fig. 2.1. The spectrometer is divided into four chambers – source, interferometer, sample, and detector. Light from the source chamber is focused on the beamsplitter at a small angle of incidence, and is split into two beams, i.e., one reflected and one transmitted. Both reflected and transmitted beams go to a moving two-side mirror, which gives a path length difference. Then the two beams are recombined at the beamsplitter and directed through the sample chamber to the detector. The entire system is operated under vacuum.

a) *Interferometer and beamsplitter*

The Bruker IFS 113v uses Genzel-type interferometer, which is similar to a Michelson interferometer. A Michelson interferometer is illustrated in Fig. 2.2. Here, the incident beam is split into two parts by a beamsplitter. Half of the radiation transmitted by beamsplitter is reflected from the movable mirror M$_2$. The other

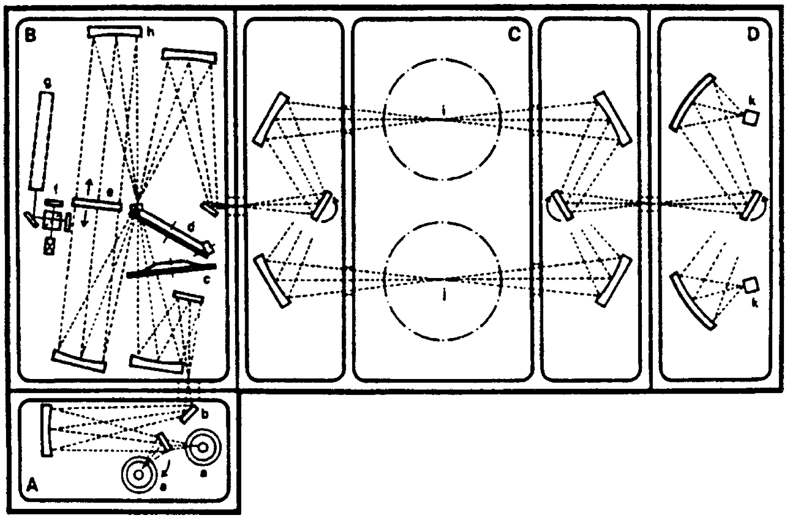

Figure 2.1: Optical layout of the Bruker 113V FTIR spectrometer.
A. Source Chamber; a- Tungsten lamp, Hg arc lamp, glowbar; b- automated aperture. B. Interferometer Chamber; c- optical filter; d- automatic beamsplitter changer; e- two-sided moving mirror; f- control interferometer; g- reference laser; h- remote control alignment mirror. C. Sample Chamber; i- sample focus; j- reference focus. D. Detector Chamber; k- far- and middle infrared deuterated triglycerine sulfate (DTGS) detector, far-infrared Si bolometer detector.

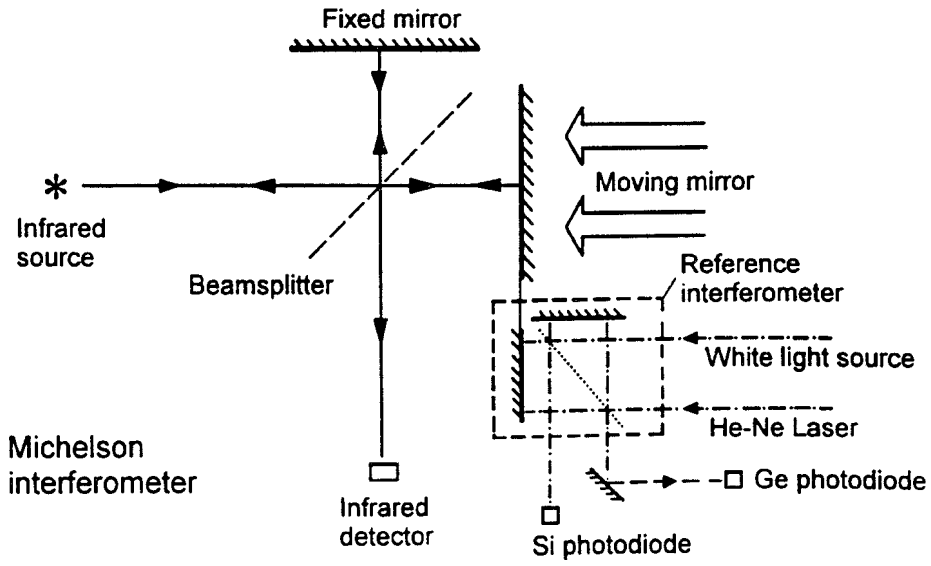

Figure 2.2: Schematic diagram of the Michelson interferometer

half is reflected onto the fixed mirror M_1. Both beams are recombined again at the beamsplitter, and recorded by detector D. The intensity of the recombined beams $I(x)$ (interferogram function) depends on the path difference between the fixed mirror M_1 and the moving mirror M_2. The plot of $I(x)$ as a function of path difference x is known as an interferogram. If M_2 travels at a constant velocity, the relation between interferogram function $I(x)$ and the source intensity $B(\omega)$ is given by

$$I(x) = 1/2 \int_0^\infty B(\omega) cos 2\pi\omega dx,$$

where ω is the frequency in wavenumbers. $I(x)$ is the cosine Fourier transform of $B(\omega)$, and contains complete information about the spectrum. Thus, the Fourier transform of the interferogram gives the single beam infrared spectrum. The typical transmittance or reflectance spectrum is the ratio spectrum of sample to reference. In the Bruker IFS 113v, a secondary laser/white light interferometer physically attached to the main Genzel-type interferometer (as shown in Fig. 2.1) provides an

Table 2.2: Bruker IFS 113v operating parameters

Range (cm^{-1})	Beam splitter	Opt. Filter	Source	Polarizer	Detector
10-50	Mylar 50 μ	Black PE	Hg arc	1	bolometer, DTGS
30-120	Mylar 23μ	Black PE	Hg arc	1	bolometer, DTGS
50-240	Mylar 12μ	Black PE	Hg arc	1	bolometer, DTGS
100-600	Mylar 3.5μ	Black PE	Hg arc	1	bolometer, DTGS
450-4000	KBr	open	Globar	2	DTGS

PE = polyethylene. Polarizer 1 = wire grid on oriented PE, Polarizer 2 = wire grid on AgBr

"optical marker" to initiate the start of spectrum data acquisition and also to precisely determine the optical path difference and speed of the main moving mirror. The design is essential for accurate Fourier transformation.

b) *Source, beamsplitter, detector, and accessories*

In order to obtain the best far- and middle-infrared spectrum, we have to choose the appropriate combination of sources, beamsplitters, detectors, and polarizers. Table 2.2 lists the typical operating parameters.

Typically, an external He-cooled Si bolometer detector made by INFRARED Laboratory Inc. is used for far-infrared measurements. The intensity of a black-body source becomes very weak in the far-infrared region, and the room-temperature DTGS detector does not have sensitivity to provide sufficiently high signal-to-noise ratio. The INFRARED Laboratory Inc. bolometer provides a much higher sensitivity (100 times better than DTGS) and lower noise level (less than 1% at liquid helium temperature).

The spectra taken with different beamsplitters are merged together to give the whole spectrum in the far- and middle- infrared. The spectrum can be merged with the data taken with the Perkin-Elmer λ-900 spectrometer, if necessary.

Table 2.3: Bruker IRscope II operating parameters

Beam splitter	Detector	Range (cm^{-1})
KBr	MCT	600-8000
Quazi	InPb	7500-12500 with near-infrared polarizer
Quazi	Si diode	12300 -16000 with visible polarizer

2.3.2 Bruker Equinox 55 IR Microscope

The Bruker IR Scope II is designed for accurate measurement of micro samples, or small areas on larger samples. In our lab, Bruker IRscope II combined with Bruker Equinox 55 FTIR spectrometer can be used to obtain the spectrum from the middle-infrared to visible range. It is ideal for small crystals, small edges of a crystal, and checking the absolute reflectance level obtained on the other instruments.

Bruker Equinox 55 FTIR spectrometer is equipped with a Globar source, two beamsplitters, and a DTGS detector. It has an external port to transfer the incident light to the IRscope II. IRscope II has three objectives (4×, 15×, and 30×), and several detectors (MCT, InPb, and Si diode) to cover the energy range from 600-16000 cm^{-1}.

Figure 2.3 shows the optical path of Bruker IRscope II. The IRscope II can measure reflectance or transmission of the sample by changing the orientation of mirror 22. The infrared or visible mode can be chosen depending on the orientation of mirror 3 (reflectance mode) or 17 (transmission mode). The detector can be changed by flipping mirror 13. Table 2.4 lists the operating parameters of Bruker Equinox 55 FTIR spectrometer combined with IRscope II. The spectrometer is operated under N_2 purge.

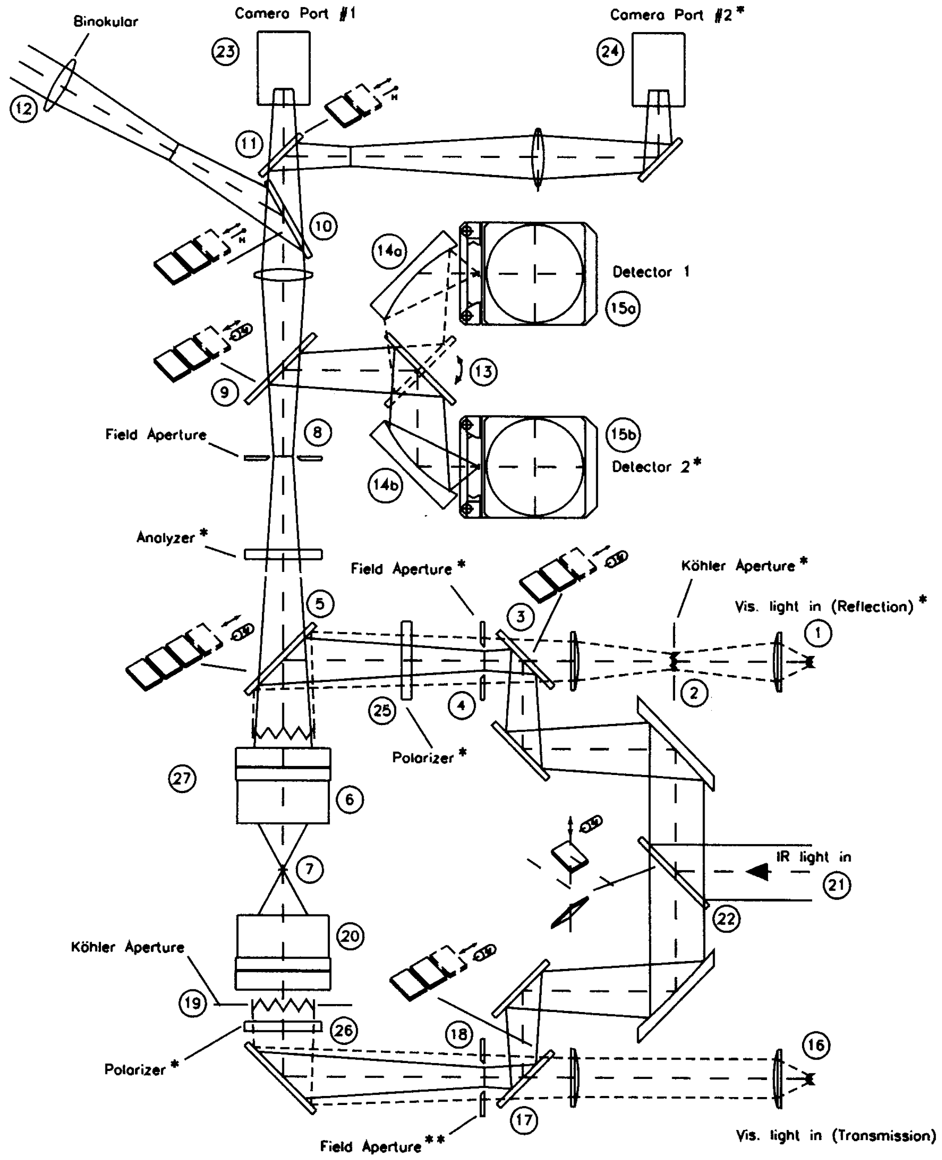

Figure 2.3: Optical path diagram of Bruker IRscope II.

1,16-visible light source; 2,19- visible light aperture; 3,22- motorized switch mirror; 4,18-optional iris or knife edge aperture; 5,9,10,17- beamsplitter changer; 6- Objective lens; 7-Sample; 8- Iris or knife edge aperture which defines the area of sample analyzed; 12- binocular eyepiece; 13- two position detector selection mirror; 14- mirror routing to detector; 15-detector; 20- condenser; 21- IR beam (from spectrometer); 23,24-camera port; 25,26,27-polarizer.

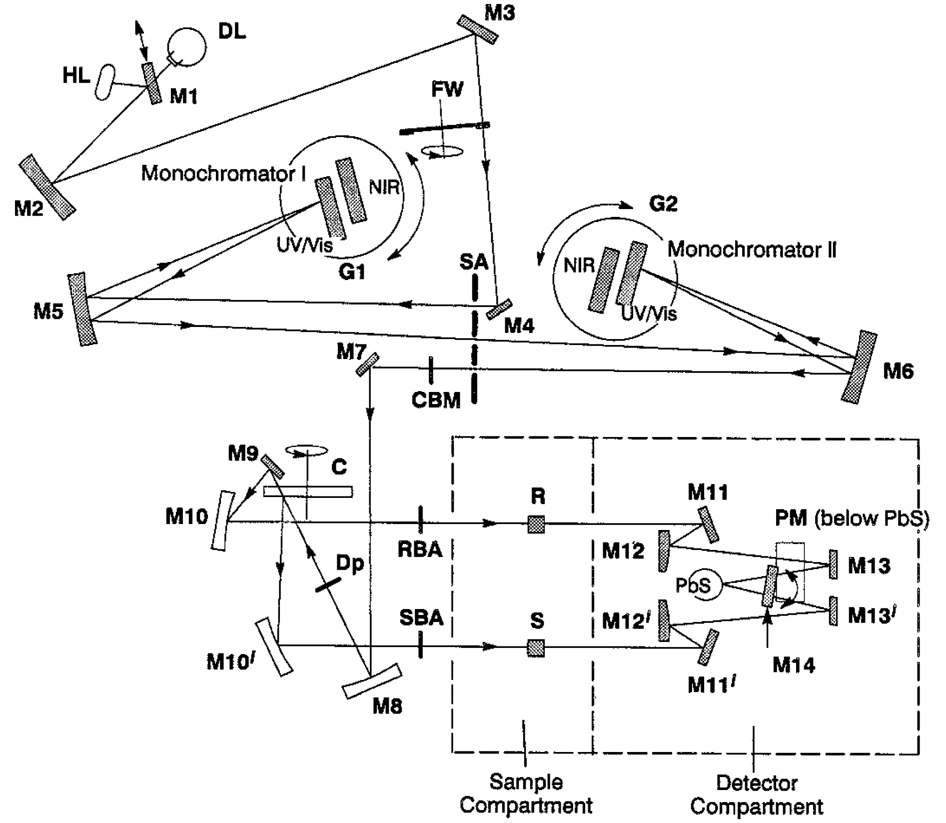

Figure 2.4: Optical layout of Perkin-Elmer λ-900

2.3.3 Perkin-Elmer λ-900 Spectrometer

The near-infrared (NIR)/Visible (Vis)/Ultraviolet (UV) spectra in this dissertation were measured on the Perkin-Elmer λ-900 Spectrometer. The Perkin-Elmer λ-900 Spectrometer features an all-reflecting, double-monochromator, double-beam optical system. The energy range covered by the λ-900 Spectrometer is 3300-190 nm ($\approx$ 3000-52000 cm^{-1}). The spectrometer is operated under nitrogen purging. The optical system is depicted schematically in Fig. 2.4.

There are two radiation sources, a deuterium lamp (DL) and a halogen lamp (HL). Halogen lamp is used for NIR and Vis range, and deuterium lamp is used for UV range. Source change is controlled by flipping mirror M1. The radiation of source is

Table 2.4: λ-900 operating parameters

Monochromator	Source	Detector	Range (cm^{-1})
Holographic Gratings	Halogen Lamp	PbS	3100-14250
Holographic Gratings	Halogen Lamp	Photomultiplier	11240-31330
Holographic Gratings	Deuterium Lamp	Photomultiplier	31330-52000

reflected by mirror M2, M3, and passes optical filter FW. Then, the beam is brought in monochromator I through M4, slit SA, and M5. Depending on the desired wavelength range, the collimated radiation beam strikes either the 2400 lines/mm grating or the 1200 lines/mm grating. The rotation position of the grating effectively selects a segment of the spectrum, reflecting this segment to mirror M5, to go through the exit slit, and enter Monochromator II. The advantage of the double-monochrometer is to maintain high spectral purity with an extremely low stray radiation content. The automatic grating change during monochromator slewing avoids the time-consuming re-alignment of the optics pathway due to themonochromator change.

The double beam is achieved via the chopper assembly C. As the chopper rotates, a mirror segment, a window segment and two dark segments are brought alternately into the radiation beam. When a window segment enters the beam, radiation passes through to mirror M9 and is then reflected via mirror M10 to create the reference beam (R). When a mirror segment enters the beam, the radiation is reflected via mirror M10′ to form the sample beam (S). When a dark segment is in the beam path, no radiation reaches the detector, permitting the detector to create the dark signal (D). Then, the measured spectrum is expressed as

$$spectrum = (S - D)/(R - D).$$

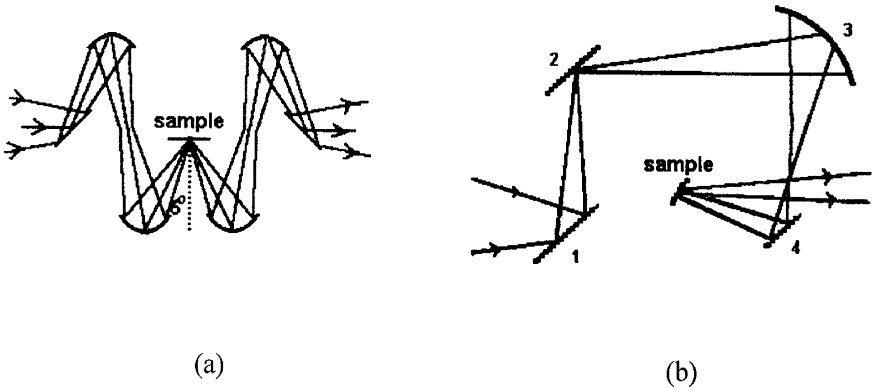

(a) (b)

Figure 2.5: Reflectance set-up for (a) Bruker IFS 113v FTIR and (b) Perkin-Elmer λ-900

Two detectors are used in the Perkin-Elmer λ-900 spectrometer. A photomulitplier (PM) is used in the UV/Vis range while a lead sulfide (PbS) detector is used in the NIR range. Detector change is automatic by rotating mirror M14 during scans.

2.3.4 Reflectance Stage and Polarizers

To measure the absolute reflectance spectrum, a reflectance stage (as shown in Fig. 2.5) is used to bring the near normal incident ($< 6^0$) light to a solid sample or reference mirror. An aluminum mirror is usually used as a reference material to obtain a baseline scan, then the reflectance spectrum of the sample is measured relative to the baseline. The absolute reflectance spectrum of the sample is obtained by renormalizing the measured spectrum with absolute Al mirror reflectance.

The optical theory outlined in Section 2.2 is based on Maxwell's equations 2.1–2.4 and Eqs. 2.5–2.7. The Eqs. 2.5– 2.7 is the material equations for an isotropic medium. In an anisotropic crystal, $\vec{D}$ and $\vec{E}$ are related by the following form:

$$D_x = \epsilon_{xx}E_x + \epsilon_{xy}E_y + \epsilon_{xz}E_z, \tag{2.24}$$

$$D_y = \epsilon_{xy}E_x + \epsilon_{yy}E_y + \epsilon_{yz}E_z, \tag{2.25}$$

$$D_z = \epsilon_{zx}E_x + \epsilon_{zy}E_y + \epsilon_{zz}E_z. \tag{2.26}$$

The nine qualities ϵ_{xx} ϵ_{xy}, ...are constants of the medium, and constitute the dielectric tensor. It is always possible to find a set of axes, *the principle dielectric axes*, such that the complex dielectric tensor can be put into diagonal form, i.e.,

$$\epsilon(q,\omega) = \begin{vmatrix} \epsilon_{xx} & 0 & 0 \\ 0 & \epsilon_{yy} & 0 \\ 0 & 0 & \epsilon_{zz} \end{vmatrix} . \tag{2.27}$$

Along the principle axes, $\vec{D}$ and $\vec{E}$ have the same directions. Since the dielectric tensor varies with frequency, the directions of the principal axes may also vary with frequency. This dispersion of the axes can arise only in crystals with monoclinic and triclinic symmetry. In the reflectance experiment on single crystals, the principal axes can be determined by considering the crystal shape and measuring the polarization dependence of the reflectance response.

To find the dielectric tensor along the principle axes of the single crystals, a polarized electric field of the light $\vec{E}$ is required. The polarized light is obtained by inserting a polarizer in the path of the beam. Several polarizers are used to cover the spectral range from far-infrared to UV. In the infrared, the polarizers used are made of a gold wire grid, vapor deposited on polyethlylene (far-infrared) or silver bromide substrates. A set of plastic Polariod film polarizers are used for the IR microscope. In the NIR/Vis/UV range, dichroic Glan-Thompson and Glan-Taylor polarizers are used for Perkin-Elmer λ-900.

2.4 Low-Temperature and High-Field Measurements

2.4.1 Low-Temperature Techniques

The low-temperature measurements were carried out with an open-flow cryostat. For the low-temperature experiments with the Bruker IFS 113v and Perkin-Elmer λ-900, an APD LT-3-110 Heli-Tran Liquid Transfer Refrigeration system with dual temperature sensors together with a Lakeshore Model 330 temperature controller were adapted. The principles of operation are illustrated in Fig.2.6. Cooling is accomplished by a controlled liquid He transfer through a high efficient transfer line to a heat exchanger adjacent to the sample interface. A needle valve at the end of the Heli-Tran transfer line permits precise control of the flow rate. The cooling rate can be regulated by changing the pressure of the supply dewar, adjusting the flowmeter and optimizing the position of the needle valve. It often takes about 25 minutes to precool the system, and the lowest stable temperature obtained is ~ 5 K.

To improve the thermal contact, crycon grease is placed between the cold stage of the cryostat and the sample holder, and the sample is mounted on the sample holder with GE Varnish and silver paste. There are two thermal sensors inside the cryostat, one is embedded in the tip of the cold stage, the other one is mounted on the sample holder. In this configuration, the temperatures provided by the two sensors allow us to estimate the real sample temperature.

2.4.2 Experimental Set-up at the NHMFL

The National High Magnetic Field Laboratory (NHMFL) provides a great opportunity to do magnet-related research. The world record magnets and magneto-

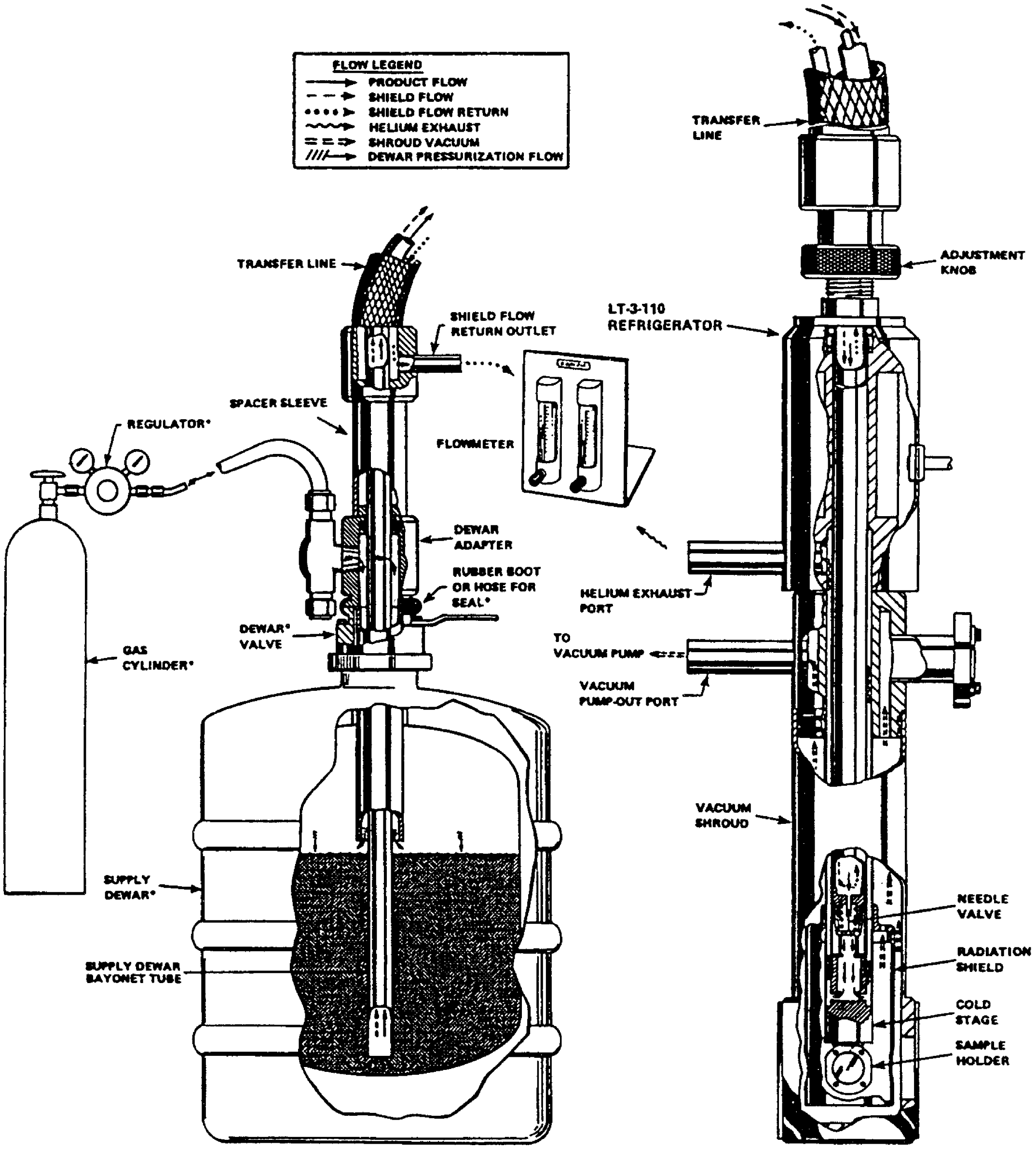

Figure 2.6: Set-up of LT-3-110 Heli-Tran liquid transfer line and cryostat.

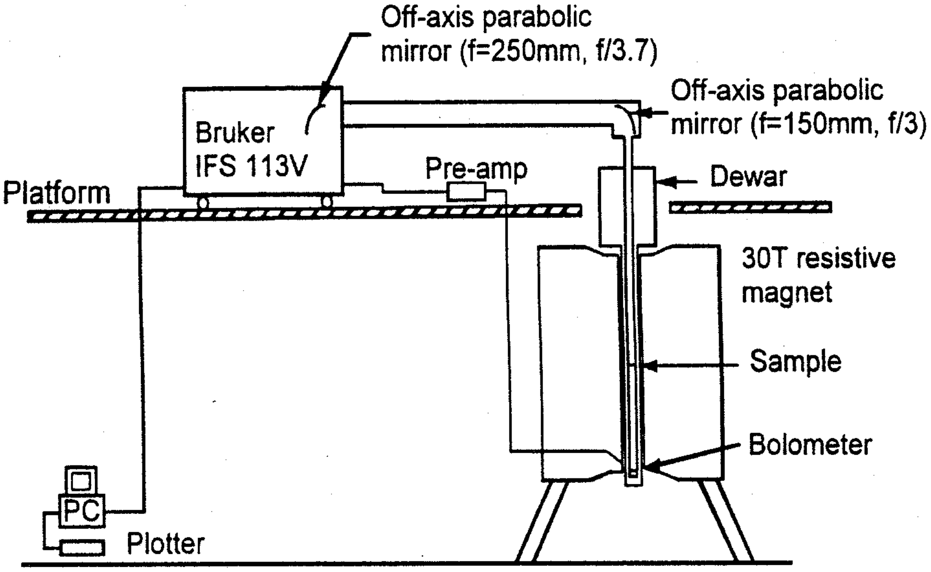

Figure 2.7: A schematic of IR set-up in the resistive magnet at NHMFL (after Ref. [60]).

optics facilities at NHMFL make it possible to investigate the unusual nature of low-dimensional solids in very high magnetic fields. For more information, visit the website of NHMFL at *http://www.nhmfl.gov*. The information in this section is largely from NHMFL website and Refs. [60–62].

Figure 2.7 shows a schematic of the infrared set-up for the transmission measurement in the 30 T resistive magnet. The infrared radiation provided by a Bruker 113v FTIR spectrometer is reflected out of the back sample chamber by an off-axis parabolic mirror. Another mirror in the light pipe further diverts the beam by 90° and focuses the beam onto the sample which is located in the middle of the probe. The transmitted light is finally collected by a Si-doped Bolometer and transformed into an electric signal. The signal is amplified and sent back to the Bruker to be processed by the computer. For the measurement in the NIR/Vis/UV range, a MacPherson 0.75m single grating monochrometer/spectrometer with a CCD camera or Ge detector is used to cover the energy range from 300-1600 nm, and the light is

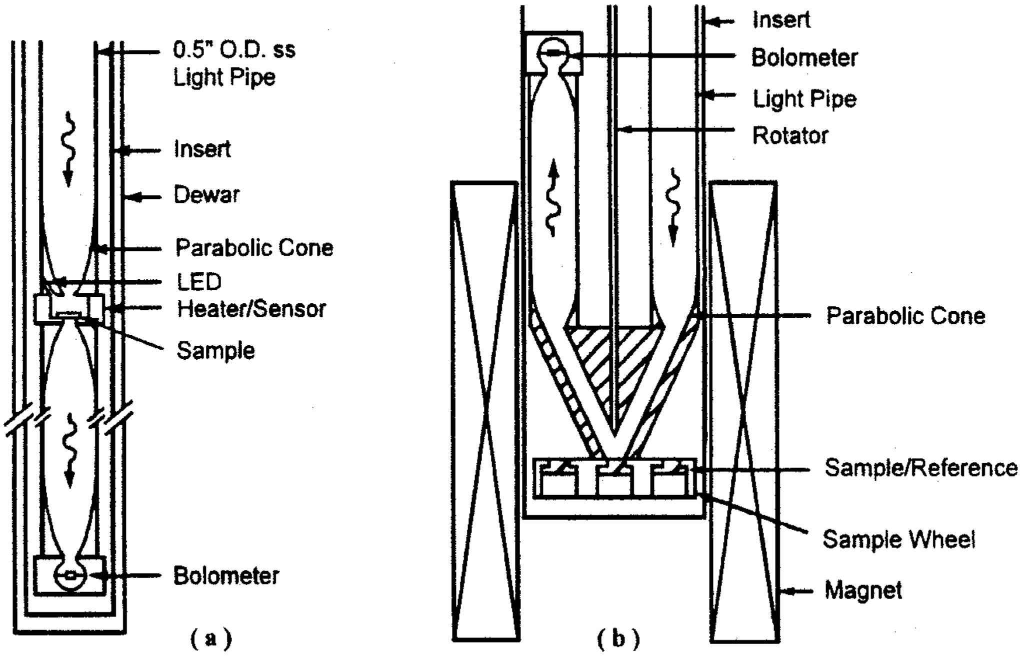

Figure 2.8: A schematic of (a) the transmittance probe used in the resistive magnet, and (b) the reflectance probe in the superconducting magnets (after Ref. [60]).

transferred in and out of the probe by appropriate optical fibers. Similar set-up can be used for the reflectance measurement with a different type of probe. Figure 2.8 displays the schematic representation of the transmittance probe used in the resistive magnet and the reflectance probe designed for the superconducting magnet.

2.5 Materials of Interest and Measurement Details

2.5.1 Vanadium Oxide Nanoscrolls

The vanadium oxide nanoscrolls were provided by M. Stanley Whittingham's group from Binghamton University, State University of New York. These nanoscrolls were prepared by an initial sol-gel reaction followed by hydrothermal treatment [63, 64]. V_2O_5 and an appropriate amine template ($C_nH_{2n+1}NH_2$ with $n = 4$ - 18) were mixed in a 1:1 molar ratio in ethanol and stirred for 3 hours in air. The mixture was then hydrolyzed under vigorous stirring followed by aging, which led to the formation of a yellow suspension. Subsequent hydrothermal treatment for 7 days resulted in a black powder. The product was washed with ethanol, diethyl ether, and water to remove excess amine and any decomposed products. The material was then dried under vacuum at 80 °C for twelve hours. The nanoscrolls were prepared with a variety of different amine templates, allowing control over the sheet distance. Ion exchange was preformed by stirring a mixture of vanadate nanoscrolls and MCl_2 (M=Mn, Zn, and Na, molar ratio 1:4) for 2 hours in ethanol/water mixture (4:1 by volume). The resulting mixture was centrifuged and washed with water, ethanol and diethyl ether. The product was then dried in the vacuum at 80 °C for twelve hours. The tubular morphology of the product was confirmed by transmission electron microscopy, and the sheet distance was determined by x-ray diffraction. For the pristine compounds,

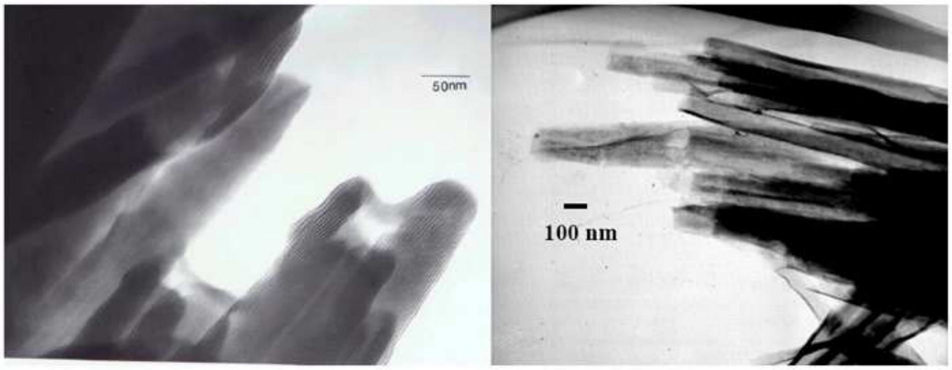

Figure 2.9: Typeical TEM images of vanadate nanoscrolls (left) showing open ends and Mn^{2+} substituted nanoscrolls (right). The layered structure inside the vanadate scrolls appears as alternating narrow dark and broad bright lines. (after Ref. [64])

the sheet distance varied between ∼15 and 35 Å. Figure 2.9 displays TEM images of pristine and ion substituted nanoscrolls.

Transmittance measurements

The vanadate nanoscrolls were mixed with pure KCl powder and pressed at 20,000 psi under vacuum to form isotropic pellets for transmission measurements. The compounds were evenly suspended in the KCl matrix. Different loading levels (∼0.05, 0.03, and 0.02% by weight) were employed as needed to obtain optimum sensitivity over the full energy range of our investigation. The middle and near infrared transmittance spectra were measured with a Bruker Equinox 55 FTIR coupled a Bruker IR Scope II. The near-infrared, visible, and near-ultraviolet spectra were measured with a modified Perkin-Elmer λ-900 spectrometer. Low temperature experiments were carried out with an open-flow cryostat. Spectral resolution is 2 cm^{-1} in the infrared range and 2 nm in the near-infrared, visible, and near-ultraviolet. The absorption spectrum was calculated from the transmittance as $\alpha(\omega) = -\frac{1}{hd} lnT(\omega)$, where h is the loading of vanadate nanoscrolls in the KCl matrix, and d is the pellet thickness.

Reflectance measurements

The vanadate nanoscrolls were also pressed into pellets for near normal reflectance measurements. Here, no matrix material was used. The spectroscopic experiments were carried out over a wide energy range (4 meV - 6.2 eV; 30 - 50000 cm^{-1}) using a series of spectrometers including a Bruker 113V Fourier transform infrared spectrometer, a Bruker Equinox 55 Fourier transform infrared spectrometer equipped with an infrared microscope, and a Perkin Elmer Lambda 900 grating spectrometer. The spectral resolution was 2 cm^{-1} in the far and middle-infrared and 2 nm in the near-infrared, visible, and near-ultraviolet. Aluminum mirrors were used as references for all measurements. Variable temperature spectroscopies were carried out between 4.2 and 300 K using an open-flow helium cryostat and temperature controller. The optical constants were calculated by a Kramers-Kronig analysis of the measured reflectance: $\tilde{\epsilon}(\omega) = \epsilon_1(\omega) + i\epsilon_2(\omega) = \epsilon_1(\omega) + \frac{4\pi i}{\omega}\sigma_1(\omega)$. [29]

2.5.2 $\mathrm{VOHPO_4}\cdot\frac{1}{2}\mathrm{H_2O}$

$\mathrm{VOHPO_4}\cdot\frac{1}{2}\mathrm{H_2O}$ samples are provided by Charlie C. Torardi from DuPont Company. Single crystals of $\mathrm{VOHPO_4}\cdot\frac{1}{2}\mathrm{H_2O}$ were grown by hydrothermal reaction of $\mathrm{VO_2}$ (99.9%, Aldrich), $\mathrm{V_2O_3}$ (Alfa), and $3M$ $\mathrm{H_3PO_4}$ solution in a sealed gold tube at 500 °C and 3 kbar pressure for 12 hours. The resulting samples were thin and plate-like, with typical dimensions of up to $\sim 3\times 3\times 0.1$ mm^3. Combined x-ray and infrared techniques were used to orient the crystals. They were easily cleaved along c.

Susceptibility Measurement

The magnetic susceptibility χ was measured in a SQUID-based magnetometer (Quantum Design model MPMS-7) in collaboration with James R. Thompson from Oak Ridge National Laboratory. An oriented single crystal was mounted for measurement with the magnetic field H applied along the a or b crystallographic direction. The crystal was mounted between a pair of long, thin-walled plastic tubes whose movement produced no magnetic signal in the pickup coils. Hence, the sample holder was "invisible" and no background correction was needed. The flat planar crystal was held in the center of a plastic mounting tube in an essentially background-free configuration, which was important as the magnetic signal was quite small at low temperatures. For both crystal orientations, measurements of the magnetization M as a function of H revealed an accurately linear response that extrapolated through the origin within statistical uncertainty; this shows that the sample was free of any ferromagnetic contamination. The differential susceptibility was obtained from the ratio M/H by measurement in a fixed magnetic field $H = 5$ kOe. The magnetic moment of the crystal was measured with both increasing and decreasing temperatures over the range 2 - 300 K. No evidence of thermal (or magnetic) hysteresis was observed.

Electron Spin Resonance Measurement

The electron spin resonance (ESR) experiments were performed in collaboration with Sergei Zvyagin from National High Magnetic Field Laboratory, using a Bruker Elexsys E680X spectrometer at the X-band frequency (9.4 GHz) and at temperatures between 5 and 200 K. The magnetic field was applied along the c axis.

Infrared and Optical Transmittance Measurement

Variable temperature transmittance measurements were carried out on single crystals of $VOHPO_4 \cdot \frac{1}{2}H_2O$ over a wide energy range (4 meV - 6.2 eV; 30 - 50000 cm^{-1}) using a series of spectrometers including a Bruker IFS 113V Fourier transform infrared spectrometer equipped with a bolometer detector, a Bruker Equinox 55 Fourier transform infrared spectrometer equipped with a microscope attachment, and a modified Perkin-Elmer Lambda-900 grating spectrometer. Our resolution was 0.5 cm^{-1} in the infrared and 2 nm in the optical regime. Selected infrared measurements were also carried out with 0.1 cm^{-1} resolution. For cleaved single crystals, appropriate polarizers were used to separate the response along the a and b directions. Even with the thinnest crystals, a number of vibrational bands in the polarized spectra were saturated. To get the whole spectrum, several crystals were ground with pure KCl powder and pressed at 20000 psi to form isotropic pellet for unpolarized infrared measurements. The advantage of this technique is that we can adjust the sample loading to highlight a feature of interest; however, in such measurements, polarization information is lost. The low-temperature spectroscopic measurements were carried out with a continuous-flow helium cryostat and temperature controller. For peak fitting purposes, absorbance was calculated from transmittance as $-\frac{1}{d}\ln T(\omega)$, where T is the transmittance and d is the thickness of the sample, which is ∼10-100 microns. Peak positions and integrated oscillator strengths were determined by standard peak fit procedures.

2.5.3 $(La_{0.4}Pr_{0.6})_{1.2}Sr_{1.8}Mn_2O_7$

$(La_{0.4}Pr_{0.6})_{1.2}Sr_{1.8}Mn_2O_7$ samples are provided by Ramanathaan Suryanarayanan's group from Université Paris-Sud. Single crystals of $(La_{0.4}Pr_{0.6})_{1.2}Sr_{1.8}Mn_2O_7$ were grown from sintered rods of same nominal composition by the floating-zone technique, using a mirror furnace. [55] Typical crystal dimensions were ≈4×5×2 mm^3. They were cleaved to yield a shiny surface corresponding to the *ab* plane.

Reflectance Measurement

Near normal *ab* plane reflectance of $(La_{0.4}Pr_{0.6})_{1.2}Sr_{1.8}Mn_2O_7$ was measured over a wide energy range (3.7 meV - 6.5 eV) using different spectrometers including a Bruker 113V Fourier transform infrared spectrometer, a Bruker Equinox 55 Fourier transform infrared spectrometer equipped with an infrared microscope, and a Perkin Elmer Lambda 900 grating spectrometer. The spectral resolution was 2 cm^{-1} in the far and middle-infrared and 2 nm in the near-infrared, visible, and near-ultraviolet. Aluminum mirrors were used as references for all measurements. Low temperature spectroscopies were carried out with a continuous-flow helium cryostat and temperature controller. Optical conductivity was calculated by a Kramers-Kronig analysis of the measured reflectance. [29]

Field Dependent Measurement

The magneto-optical properties of $(La_{0.4}Pr_{0.6})_{1.2}Sr_{1.8}Mn_2O_7$ were measured at the National High Magnetic Field Laboratory (NHMFL) in Tallahassee, FL, using a Bruker 113V Fourier transform infrared spectrometer equipped with a 18 T superconducting magnet and a grating spectrometer equipped with InGaAs and CCD detectors and a 33 T resistive magnet. Experiments were performed at 4.2 K for $H \parallel c$. Selected experiments were also carried out between 4.2 and 300 K in the spectral range of 0.75 - 3 eV. Data were collected on both increasing and decreasing magnetic field. Upsweep data were plotted here. After each field sweep, the samples were heated to 80 K to erase the “memory”. The field-induced changes in the measured reflectance were studied by taking the ratio of reflectance at each field and reflectance at zero field, i.e., [R(H)/R(H=0 T)]. To obtain the high field optical constants, we renormalized the zero-field absolute reflectance with the high-field reflectance ratios, and recalculated σ_1 and ϵ_1 using Kramers-Kronig techniques. [29] Due to limited coverage of the spectrometers at the NHMFL, the measured data were spliced together with curve fitting techniques between ~0.5 and 0.75 eV.

Color Rendering Techniques

Standard color rendering techniques are employed in collaboration with Jason Haraldsen to visualize temperature- and field-induced spectral changes. [65,66] Through a Kramers-Kronig analysis, one can determine the extinction coefficient as a function of frequency, $\kappa(\omega)$. The absorption coefficient, α, is calculated as α=$4\pi\kappa(\omega)$. Here, the absorption coefficient data are "matched" with the effective absorption using a proportionality constant (which is typically on the order of the pellet thickness times the loading). The absorption coefficient needs to be normalized by a constant, K, to determine the effective absorption of the material. K is dependent on factors such as the mass fraction and thickness of the transmittance sample. However, because these are reflectance measurements of a solid material, K is unknown. This constant can be approximated by an examination of the transmittance of the material or by normalizing the absorption to a distinct value of color (assuming the color of the material is known). Once K is determined for a material, it is the same for all spectra and is not dependent on magnetic field or temperature. A comparison of the absorption coefficient to the effective absorption spectrum can be used to render color by integrating the product of the spectrum with the well-known XYZ color matching functions to determine the XYZ color values. [65] These XYZ values are converted into RGB color values and then inverted to determine the color of a material. [65] The final RGB values allow color rendering.

Impedance Measurements

Impedance measurements were carried out at 30 kHz, using an Agilent 4284A LCR meter in a two-wire configuration with the AC current parallel to the applied magnetic field. The high temperature impedance was corrected for the contribution from the probe, which is negligible at 4.2 K.

Chapter 3

Current Problems in Transition Metal Oxides-Literature Survey

Transition metal oxides represent one of the most fascinating categories of inorganic solids with a wide variety of structures and properties. They can be metallic (such as RuO_2 and $LaNiO_3$), insulating (such as $BaTiO_3$), ferromagnetic (such as CrO_2), ferrimagnetic (such as Fe_3O_4), antiferromagnetic (such as NiO), ferroelectric (such as $BaTiO_3$), and high-temperature superconducting (such as $YBa_2Cu_3O_{7-x}$). [2,3,67–71] These electronic and magnetic properties are tunable with change in temperature, pressure, chemical composition, or magnetic field, making transition metal oxides suitable for fundamental investigations as well as many practical applications. In the following of this chapter, I will review some of the most interesting problems in transition metal oxides.

3.1 VO_x Nanoscrolls

Nanophase materials represent a field of fundamental interest because this unique class of compounds is connected with interesting solid state physical and chemical properties that can be exploited for a variety of practical applications. The tubular structure provides a high aspect ratio, access to different contact regions, and the ability to assemble into more complex architectures. These characteristics make nanotubes very promising candidates for the realization of highly functional, effective, and resource-saving devices such as single electron transistors, sensors, capacitors, and storage/release systems. The discovery of carbon nanotubes revolutionized fundamental science at the nanoscale. [72] More recently, the synthesis of inorganic fullerene-like materials such as MoS_2, WS_2, BN, TiO_2, $NiCl_2$, VO_x, and NbS_2 has attracted attention. [12–24]

The electronic structure and vibrational properties of inorganic fullerene-like materials are of great current interest. Theoretical predictions of strain energy, optical gap, and electronic structure have focused on Si- and P-based tubes, NbS_2, MoS_2, WS_2, GaN, GaSe, as well as BN nanostructures. [73–80] In GaSe, GaN and MoS_2, the energy gap is predicted to increase toward the bulk value as the tube diameter increases, whereas the strain energy decreases with increasing tube diameter. [73,74,79] Figure 3.1 displays representative theoretical predictions of stain energy and gap in GaSe and MoS_2 nanotubes. In BN nanotubes, vibrational property predictions suggest that the modes will redshift with increasing tube diameter. [81] The frequency of the radial breathing mode is of special interest and is predicted to increase with decreasing tube diameter. [81] Broad and complementary spectroscopic measurements of inorganic fullerene-like materials have been more sparse. The optical properties of selected model materials (MoS_2, WS_2, and a selected VO_x) have been studied over a limited energy range. [82, 83] In tubular MoS_2 and WS_2, the gap is lower than the corresponding bulk material, in line with the aforementioned theoretical predictions. [82] Infrared spectroscopy of bulk and nanoparticles WS_2 demonstrates that the intralayer effective charge increases slightly in the inorganic fullerene-like

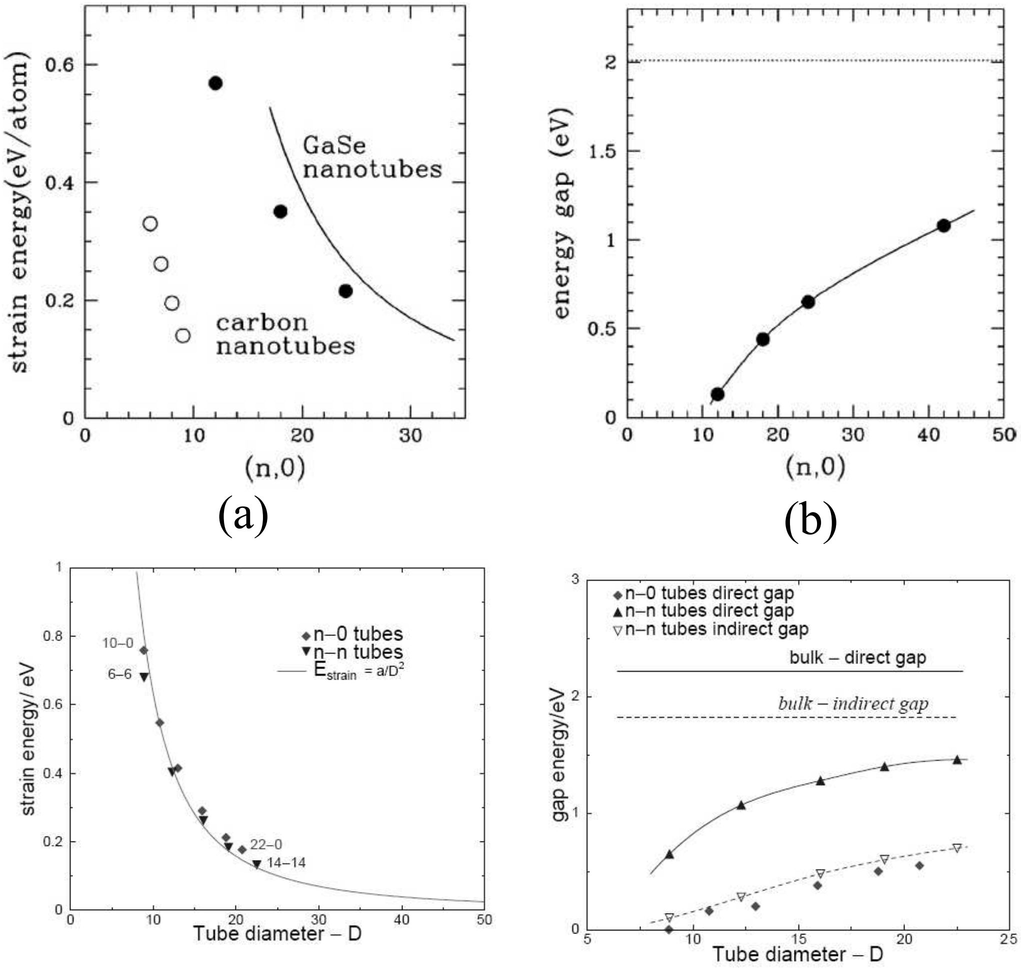

(a) (b)

(c) (d)

Figure 3.1: (a) Plot of strain energy vs. nanotube size which is given by the number of unit cells around the circumference for GaSe $(n, 0)$ tubes. (after Ref. [73]) (b) Energy gap (eV) for the GaSe $(n, 0)$ nanotubes calculated within the tight binding approach. (after Ref. [73]) (c) Calculated strain energies of MoS_2 nanotubes (energy per atom relative to the infinite single MoS_2 triple layer) as a function of tube diameter in Å. (after Ref. [74]) (d) Calculated gap energies of MoS_2 nanotubes as a function of tube diameter in Å. (after Ref. [74])

material compared to that in the bulk. [84] Photoluminescence emission of Y_2O_3:Eu nanotubes is also different from that in the bulk, displaying important surface structure and excitation wavelength effects. [85] Vibrational property measurements show broadened (MoS_2, WS_2, HfS_2), [87] red-shifted (CdSe), [86] or identical ($NbSe_2$) phonon modes compared with analogous bulk materials. [87]

Among the transition metal oxides, vanadates show particularly rich chemistry due to the tunable vanadium oxidation state and flexible coordination environment, which ranges from octahedral to square pyramidal to tetrahedral with increasing vanadium oxidation state. [45] Vanadium oxides form many layered and nanoscale compounds with open-framework, making them prospective materials for ion intercalation, exchange, and storage. [27, 88–90] The nanoscale vanadates, $(\text{amine})_y\text{VO}_x$ of interest here are mixed-valent with $x \sim 2.4$. These compounds are actually scrolls, consisting of vanadate layers between which organic molecules are intercalated. [26, 27, 63, 88, 91] The size of the amine or diamine template determines scroll winding, providing an opportunity to tune the size of these materials. The typical scrolls are ~15-100 nm in diameter, containing up to 30 vanadium oxide layers (inset of Fig. 3.2(a)). The exact crystal structure is complicated and is not completely understood. Figure 3.2(a) shows a representative x-ray powder diffraction pattern for the $(C_{12}H_{25}NH_3)_y$-VO_x scrolls. The (00l) reflections from the vanadium oxide layers are clear, but the (hk0) reflections from the atomic structure within each layer are weak. The latter indicates a possible tetragonal lattice of basal repeat size 6.144 Å, closely related to that of BaV_7O_{16}, which has a planar structure of basal size 6.160 Å. [46] The arrangement in BaV_7O_{16} is shown in Fig. 3.2(b). [46] It contains zig-zag chains of edge-sharing VO_5 square pyramids. These chains share some corners with each other to form a two dimensional sheet. The sheets also share corners with VO_4 tetrahedra, bringing the two VO_x layers together to form a characteristic

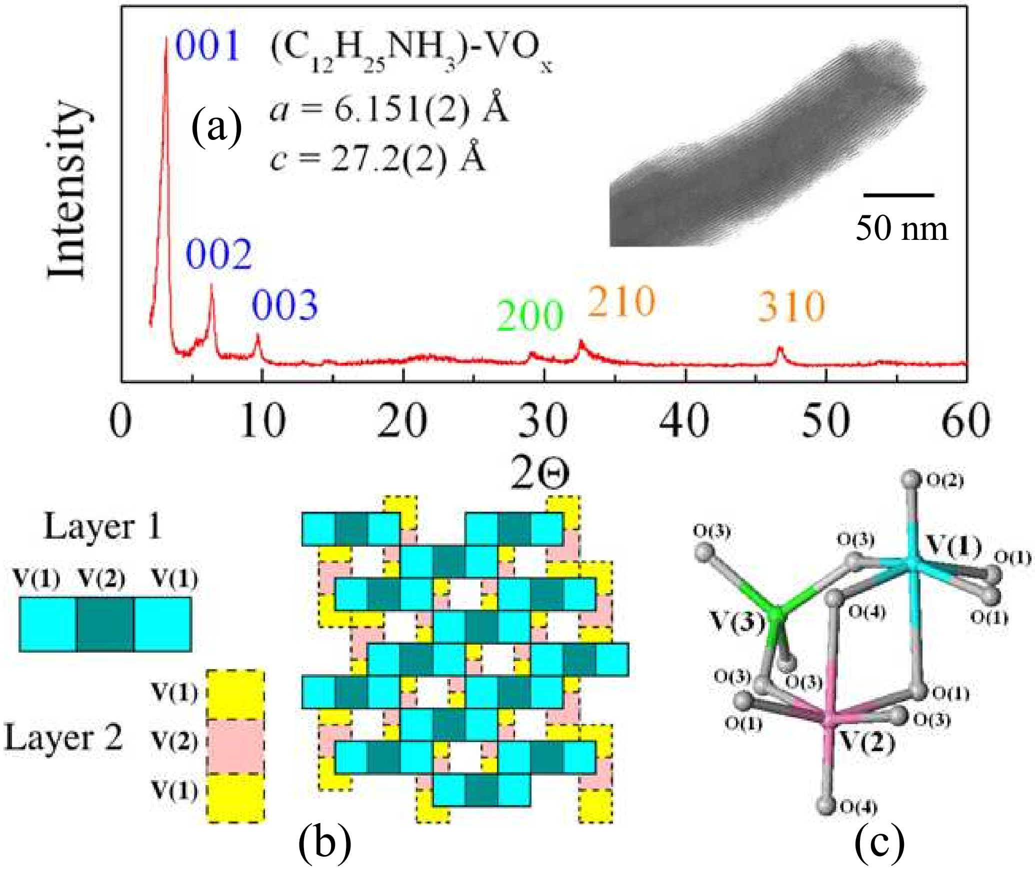

Figure 3.2: (a) Representative x-ray powder diffraction scan of $(C_{12}H_{25}NH_3)_y$-VO_x scrolls showing only 00l and weak hk0 reflections. The inset displays a representative TEM image with lattice fringing and a center cavity. (b) Probable double-layer structure of the VO_x scrolls, analogous to the BaV_7O_{16} model compound. [46] (c) Close-up view of the local structure around the V centers, showing the arrangement of octahedra and tetrahedra in the BaV_7O_{16} model compound. [46]

double sheet. Figure 3.2(c) displays the local structure around the V centers in the BaV_7O_{16} model compound. Each two-dimensional layer contains two octahedrally coordinated vanadium atoms, V(1) and V(2), with one tetrahedrally coordinated V(3) occurs in between the layers.

Scrolled vanadates exhibit very interesting physical properties including a large spin gap, diameter-dependent optical features, and potential battery and optical limiting applications. [38, 47, 83, 92, 93] Recently, electron- and hole-doped vanadium oxide nanoscrolls were reported to be 300 K ferromagnets, raising fundamental questions about their magnetic exchange mechanism. [47] The "doping" process was also predicted to convert the pristine Mott insulating scrolls into a Drude-type metal via changes in band filling and a simple shift of the Fermi energy. [47] Figure 3.3 displays a possible schematic representation of Mott-Hubbard band splitting in VO_x nanoscrolls and a simple unit-cell model of spin textures. Direct measurement of the low-energy electronic structure is clearly important to test this prediction. Further, the rigid band model raises fundamental questions about the chemical nature of the "doping" or ion exchange process in the scrolled vanadates. [47, 64, 91, 94] To date, only Mn^{2+} has been shown to completely replace the organic template, even though some other ions such as Na^+, Li^+, Zn^{2+}, Cu^{2+}, and Ca^{2+} can partially replace the amine template. [64, 91, 94] From the chemical perspective, metal intercalation does not appear as simple as "putting in electrons"; both reduction of V as well as ion exchange with the proton on the amine are possible.

3.2 Heisenberg Antiferromagnet $VOHPO_4 \cdot \frac{1}{2}H_2O$

The chemical and structural diversity of vanadium phosphates provides a rich set of model materials for fundamental investigations of low dimensional quantum spin interactions, magnetostructural correlations, and practical applications in the area

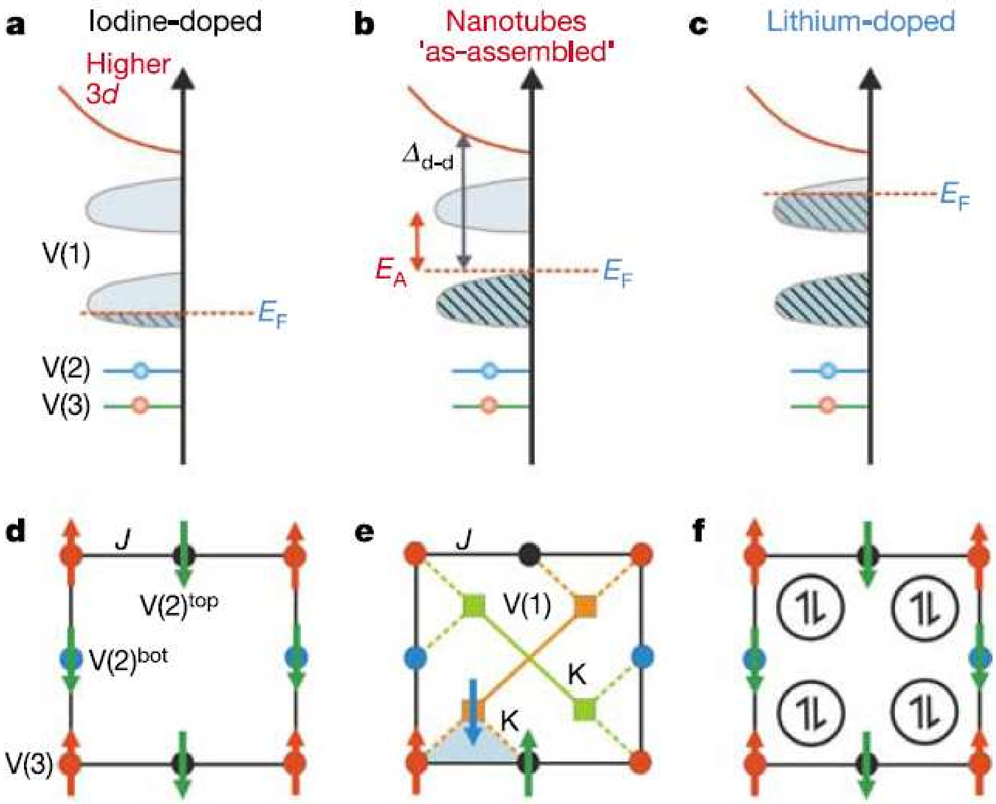

Figure 3.3: A schematic representation of Mott-Hubbard band splitting in VO$_x$ nanoscrolls and a simple unit-cell model of spin textures with and without charge doping. In a Mott insulator, the motion of each particle is hindered by the strong Coulomb repulsion U from other particles, and in this respect they are very different from band insulators, in which the Pauli exclusion principle forbids the motion of electrons. (After Ref. [47])

of catalysis, large gap scintillators, and electrodes for Li ion batteries. [48–53, 95–98] The versatility of these materials derives from the flexible vanadium oxidation state combined with novel architectures involving octahedral vanadium oxide and tetrahedral phosphate building blocks. [48–51] The bridging phosphate tetrahedra have demonstrated to provide a strong exchange route and mediate the long path magnetic interactions in many vanadium phosphates. From magnetostructural point of view, Beltrán-Porter et al. also have considered exchange pathways in several vanadyl phosphates and argued that phosphate tetrahedra pathways may be more than V-O-V. [48, 51, 52] Figure 3.4 displays schematic representation of the relative disposition of the dominant orbitals within VO_6 octahedra and PO_4 tetrahedra networks, demonstrating PO_4 tetrahedra play an important role in mediating the magnetic exchange through π bonding between different vanadium sites.

Vanadyl hydrogen phosphate hemihydrate $VOHPO_4{\cdot}\frac{1}{2}H_2O$ and its derivative vanadyl pyrophosphate $(VO)_2P_2O_7$, are two important prototypes, well-studied as gaped $S = 1/2$ Heisenberg antiferromagnets and as a precursor/catalyst for the oxidation of n-butane to maleic anhydride. [50,51,53,99–109] Figure 3.5(a) shows the 300 K ab-plane structure of $VOHPO_4{\cdot}\frac{1}{2}H_2O$. [49, 109] Each layer consists of face-sharing vanadium oxide octahedra, corner-linked by hydrogen phosphate tetrahedra in the ab-plane. Within each VO_6 octahedron, one vanadium-oxygen interaction is stronger and can be considered a vanadyl group. The vanadyl hydrogen phosphate layers are stacked along the c axis and held via interlayer hydrogen bonding interactions. At room temperature, the oxygen atoms that form the vanadium oxide octahedra, phosphate tetrahedra, and associated hydrogen atoms are statistically disordered between two equivalent positions. At low temperature, these oxygen and hydrogen atoms are ordered within both layers and between adjacent layers, thus doubling the unit cell along the c axis and reducing symmetry (from P_{mmn} to $P2_1/c$). [49,109] The structure

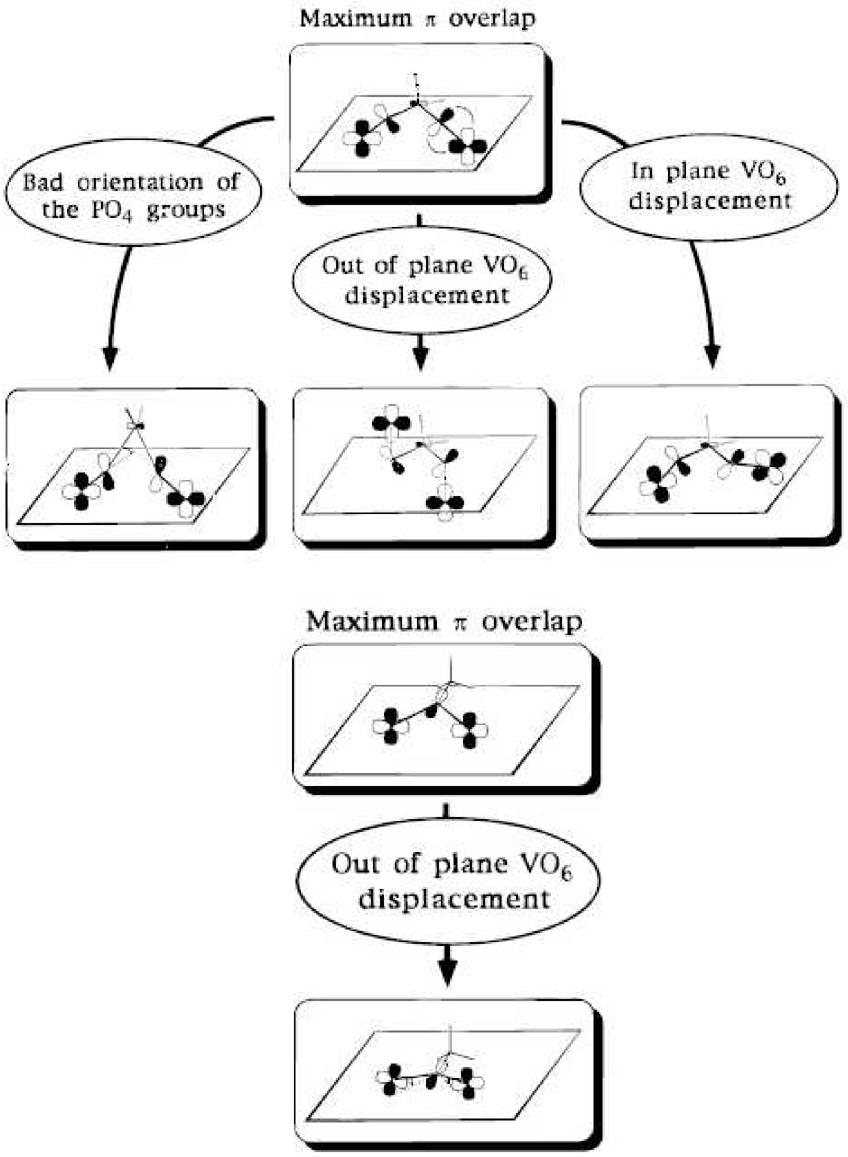

Figure 3.4: Schematic representation of the relative disposition of the dominant orbitals within VO_6 octahedra and PO_4 tetrahedra networks, showing the maximum π overlap. PO_4 tetrahedra play an important role in mediating the magnetic exchange between vanadium ions. (after Ref. [99])

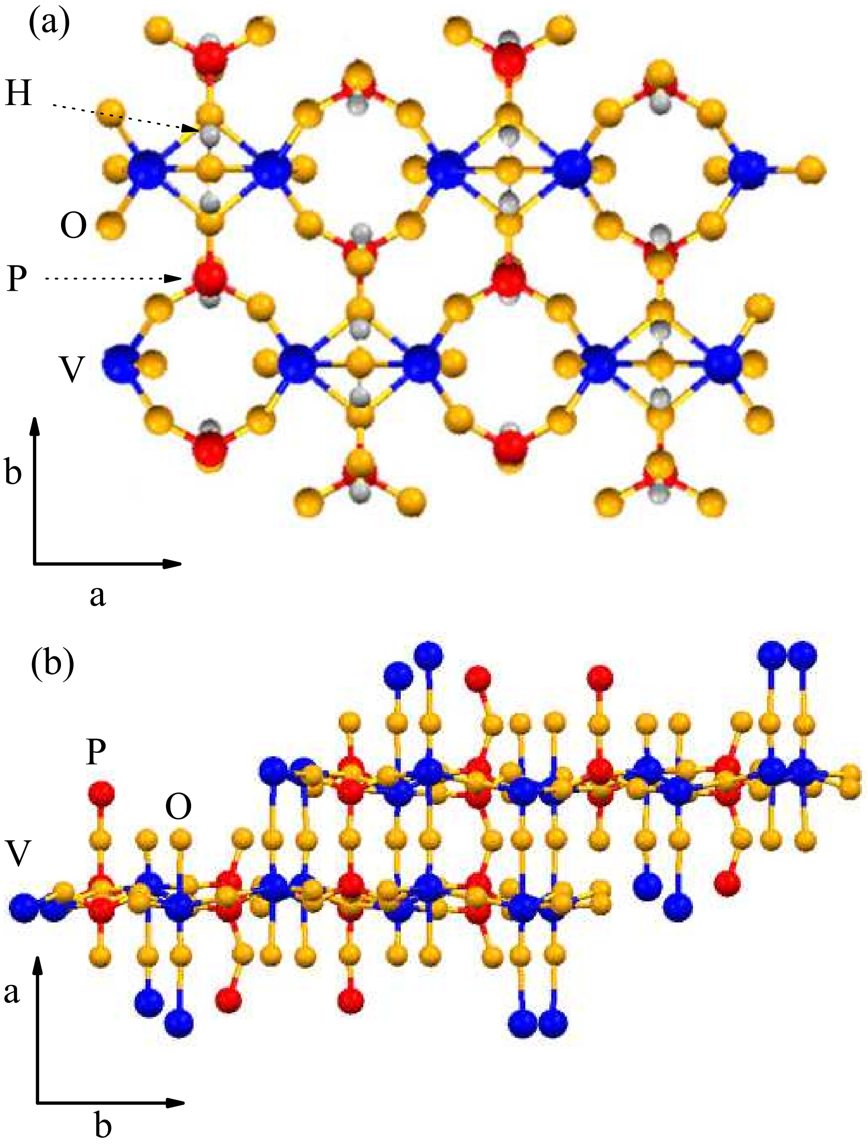

Figure 3.5: (a) 300 K structure of $VOHPO_4 \cdot \frac{1}{2}H_2O$ within the *ab*-plane. This rendering shows pairs of face-sharing vanadate octahedra interconnected by hydrogen-phosphate tetrahedra. The dominant spin dimers occur along the *a* direction. (b) 300 K structure of $(VO)_2P_2O_7$ projected within *ab*-plane. The alternating spin chain is along the *b* axis.

of $(VO)_2P_2O_7$ is related to that of its precursor (Fig. 3.5(b)). [101,109] Edge-sharing pairs of VO_6 octahedra are stacked along the a axis to form a two-leg structural ladder. The ladders are linked by covalently bonded PO_4 tetrahedra to form a three dimensional network with corner-sharing VO_6 octahedra.

Magnetostructural correlations and spin models of $VOHPO_4{\cdot}\frac{1}{2}H_2O$ and $(VO)_2P_2O_7$ have attracted sustained attention. [41,49–52,99–103,106,107,110–112] From inelastic neutron scattering investigations of the magnetic excitations [100–102] as well as several studies of spin-phonon coupling, [41,110–112] the spin Hamiltonians and low-energy dynamics of these materials are well understood. $VOHPO_4{\cdot}\frac{1}{2}H_2O$ and $(VO)_2P_2O_7$ are now known to be weakly coupled dimers and alternating chain compounds, respectively. In $VOHPO_4{\cdot}\frac{1}{2}H_2O$, alternating vanadium dimers form chains along the a axis, with V-O-V and V-O-P-O-V superexchange interactions. [100] The center-to-center distances between the vanadium sites are 3.09 and 4.33 Å, respectively. [49, 50, 100, 109] Interdimer interactions are less than 5% of intradimer exchange. [41] V-O-P-O-V superexchange interactions also connect the VO_6 units in the b direction, although the V-O-P-O-V bond angles and distances are very different from those along a. In $(VO)_2P_2O_7$, alternating magnetic chains form along the b axis, again with both V-O-V and V-O-P-O-V superexchange interactions. [102] Figure 3.6 displays the schematic representation of the structure and magnetic interactions in $VOHPO_4{\cdot}\frac{1}{2}H_2O$ and $(VO)_2P_2O_7$.

Complex hydrogen bonding networks also present in $VOHPO_4{\cdot}\frac{1}{2}H_2O$. The vanadyl hydrogen phosphate layers are stacked along the c axis and held together by two types of interlayer hydrogen bonding interactions: (1) hydrogens on shared water molecules interact with the apical oxygen atoms that are bonded to phosphate tetrahedra in an adjacent layer, and (2) covalently bound hydrogen centers interact with vanadyl oxygen atoms in a neighboring layer. [49] Hydrogen bonding can control both long-range

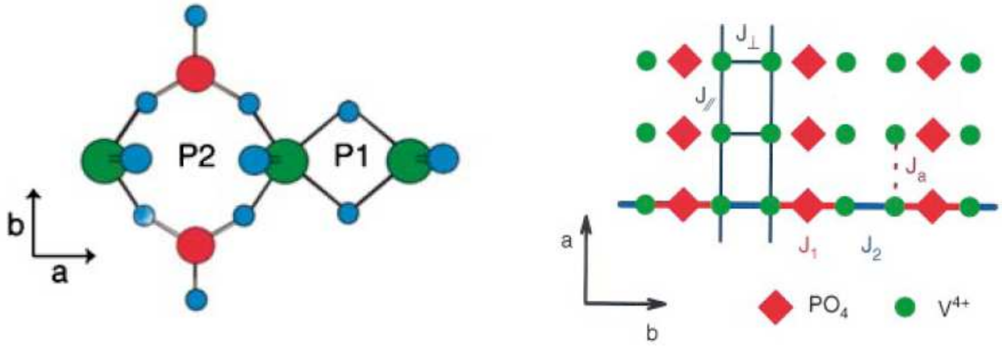

(a) (b)

Figure 3.6: (a) Schematic representation of the structure and magnetic interactions in $VOHPO_4{\cdot}\frac{1}{2}H_2O$. The dominant interaction is through P2 (V-O-P-O-V) pathway. (after Ref. [100]) (b) Schematic representation of the structure and magnetic interactions in $(VO)_2P_2O_7$. It is best described as an alternating spin chain rather than a spin ladder. (after Ref. [102])

and local structure and modulate significant magnetic exchange pathways.

3.3 $(La_{0.4}Pr_{0.6})_{1.2}Sr_{1.8}Mn_2O_7$

Substituted perovskite manganites have attracted considerable attention due to their exotic magnetic, electronic, and optical properties. These properties derive from the many competing ground states of the complex phase diagram, strong coupling across different energy scales, and the presence of an inhomogeneous texture. [4, 6, 7] One consequence of this complexity is that enormous physical property changes can be induced by small chemical and physical perturbations. Colossal magnetoresistance has been observed in doped manganites and has attracted attention at understanding the electronic and magnetic properties of these materials. [4, 7] At low temperatures, properly doped manganites exhibit ferromagnetic metallic or "badly" metallic behavior, while at high temperatures they exhibit a paramagnetic insulating behavior. The colossal magnetoresistance effect occurred at the transition temperature T_c is understood to first order within the framework of double exchange theory. [113]

The undoped compounds of the manganites, e.g. LaMnO_3 have a $3d^4$ electronic configuration. The cubic crystal field splits the degeneracy of the d orbitals into t_{2g} (d_{xy}, d_{xz}, d_{yz}) and e_g ($d_{x^2-y^2}$, $d_{3z^2-r^2}$) orbitals. The e_g orbitals hybridize strongly with the O $2p$ states, forming dispersive bands containing the electrons responsible for the conduction. The t_{2g} orbitals hybridize less strongly to those states and can be treated as localized core states, with a net spin S=3/2. Substitution of the trivalent La ions with a divalent ion such as Sr, Ca, or Ba dopes holes into the manganites and subsequently change the electronic configuration. (from $3d^4$ to $3d^3$) Figure 3.7(a) and (b) display schematic representation of Mn^{3+} and Mn^{4+} electronic configuration for LaMnO_3 and SrMnO_3, respectively.

Within the double-exchange theory, [4, 7] the hopping amplitude of the e_g hole from one site to another is a function of the relative spin alignment at the two sites, that is, $\tilde{t} = t_0 \cos(\theta/2)$. (Fig. 3.7(c)) Fully ferromagnetic alignment of the nearest neighboring spins will give the greatest hopping amplitude $\tilde{t}$ ($\theta = 0$, $\cos(\theta/2)$=1) and the greatest bandwidths, and fully antiferromagnetic alignment will lead to $\tilde{t}$ =0 ($\theta = 180$, $\cos(\theta/2)$=0), implying a non-dispersive band with zero bandwidth. The uncorrelated spins will have a reduction in hopping amplitude of roughly $1/\sqrt{2}$. ($\theta = 90$, $\cos(\theta/2)$=$1/\sqrt{2}$) (Fig. 3.7(d-e)) [4, 7] Therefore, ferromagnetic alignment will gain kinetic energy and compete with the superexchange energy which favors antiferromagnetic alignment as well as with the thermal fluctuations which favor disorder. Slightly above T_c, a large magnetic field tends to align the core (t_{2g}) spins and therefore increases the hopping amplitude between e_g electrons and driving the material more metallic. [4, 7]

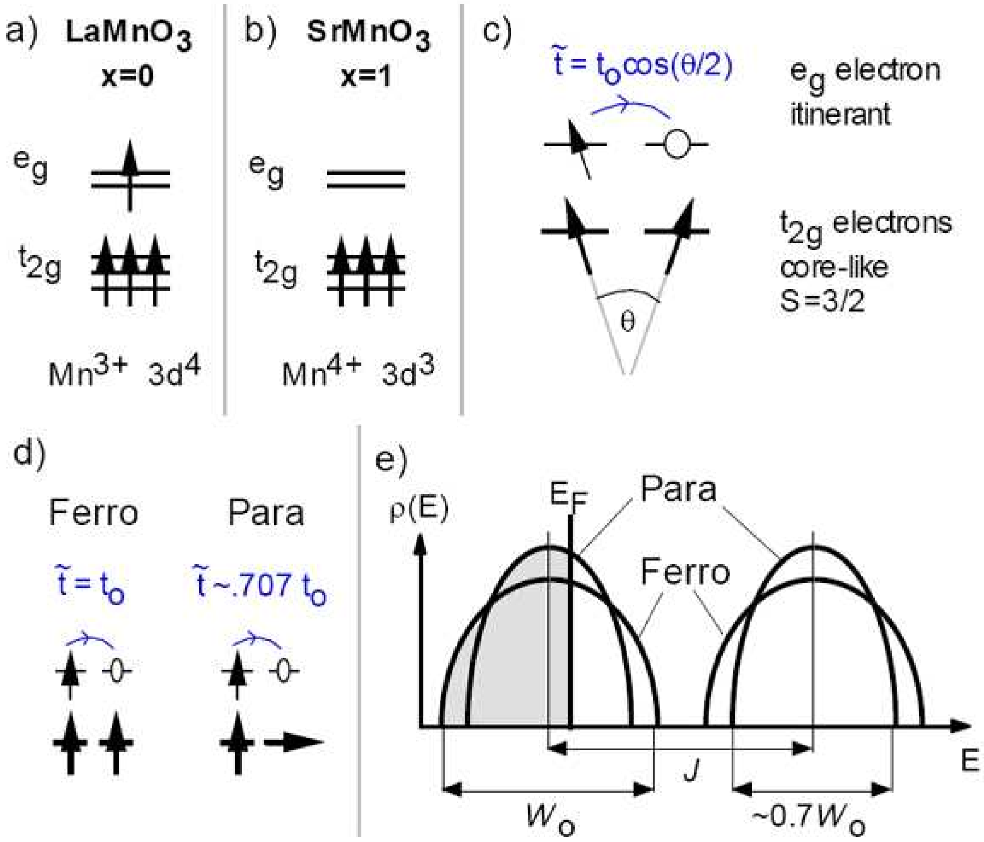

Figure 3.7: (a-b) Electronic configuration of Mn^{3+} and Mn^{4+}. (c-d) An illustration of the concept of double exchange - the hopping matrix element as a function of spin alignment. (e) The double-exchange prediction for the bandwidths for the ferromagnetic and paramagnetic cases. (after Ref. [4, 7])

Double-exchange alone is not enough to account for the behavior of the manganites. For example, the conductivity in the paramagnetic state is predicted to 0.7 times that of the ferromagnetic state by double-exchange theory, [4] while experimentally the conductivity may decrease several orders of magnitude through the transition. Other physics such as polaron formation, charge and orbital ordering, and competing degenerate ground states is necessary to explain these phenomena.

The double-layer manganites of interest here derive from the $La_{1.2}Sr_{1.8}Mn_2O_7$ parent compound, crystallizing in a body-centered tetragonal structure (space group $I4/mmm$) as shown in Fig. 3.8. [54, 55] These bilayer manganites display a broad metallic regime, colossal magnetoresistance, Jahn-Teller distortions, metal-insulator transitions, as well as charge and orbital ordering. [114–116] These materials are therefore well-suited for fundamental magnetodielectric properties investigations and are also useful to extend the Tomioka-Tokura electronic phase diagram picture [8] and test oscillator strength sum rules. [58, 59] Pr substitution of the La sites in $La_{1.2}Sr_{1.8}Mn_2O_7$ yields materials with chemical formula $(La_{1-z}Pr_z)_{1.2}Sr_{1.8}Mn_2O_7$, providing an opportunity to investigate the physical properties of bilayer manganites as a function of disorder without changing the total hole concentration. [55] Upon increasing Pr substitution (z=0, 0.2, and 0.4), the paramagnetic insulator to ferromagnetic metal transition temperature, T_c, decreases (120, 90, and 60 K, respectively). [117] At z=0.6, the transition is actually quenched. [117] This material, $(La_{0.4}Pr_{0.6})_{1.2}Sr_{1.8}Mn_2O_7$, is the subject of our present work. Pr substitution modifies the lattice constants (c/a increases), causes a change in the Jahn-Teller distortion, induces bound carrier localization in the far infrared, and modifies the e_g orbital occupancy. [117–119] Clearly, the degree of disorder strongly influences the physical properties. In fact, given that $(La_{0.4}Pr_{0.6})_{1.2}Sr_{1.8}Mn_2O_7$ is highly disordered, the aforementioned low-temperature paramagnetic insulating state can likely

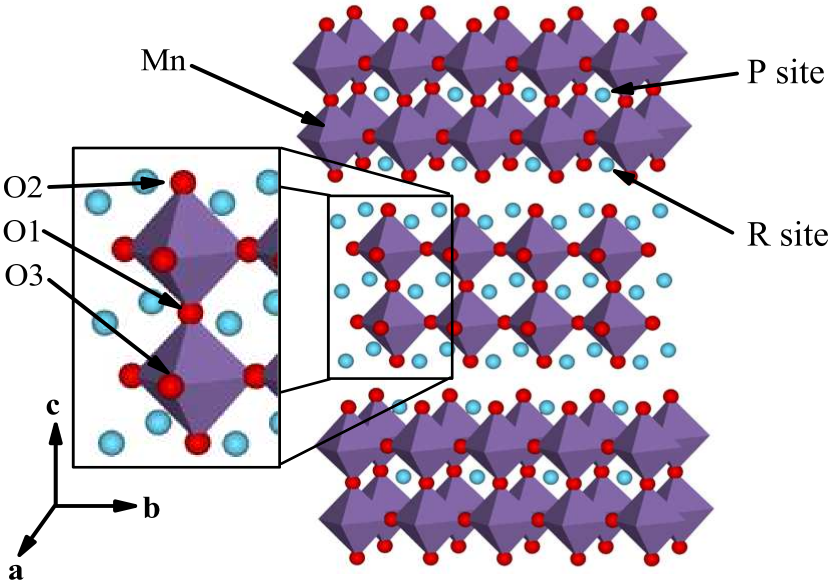

Figure 3.8: Crystal structure of $(La_{0.4}Pr_{0.6})_{1.2}Sr_{1.8}Mn_2O_7$, with O (red/black), Mn-containing octahedra (purple/gray), and the rare/alkaline earth ions (light blue/light gray). O occupies three different sites, and rare earth/alkaline earth metal have different coordination numbers depending on whether they occupy perovskite (P) or rock salt (R) sites. [54,55] Note that the unit cell along the b axis has been replicated to highlight the layered structure.

be considered to be a spin-glass insulator as well, although variable frequency ac susceptibility measurements are needed to confirm this picture. [8,55] The evolution of chemical-tuning induced states are summarized in Fig. 3.9(a) and compared with the Tomioka-Tokura electronic phase diagram picture in single layer manganites. (Figure 3.9(b))

The long-range ordered ferromagnetic state that is suppressed by chemical pressure in $(La_{0.4}Pr_{0.6})_{1.2}Sr_{1.8}Mn_2O_7$ is recovered under magnetic field. This recovery is evident in the $H-T$ phase diagram deduced from magnetization, magnetostriction, and resistivity measurements. (Figure 3.10(a)) [120,123–125] Magneto-optical

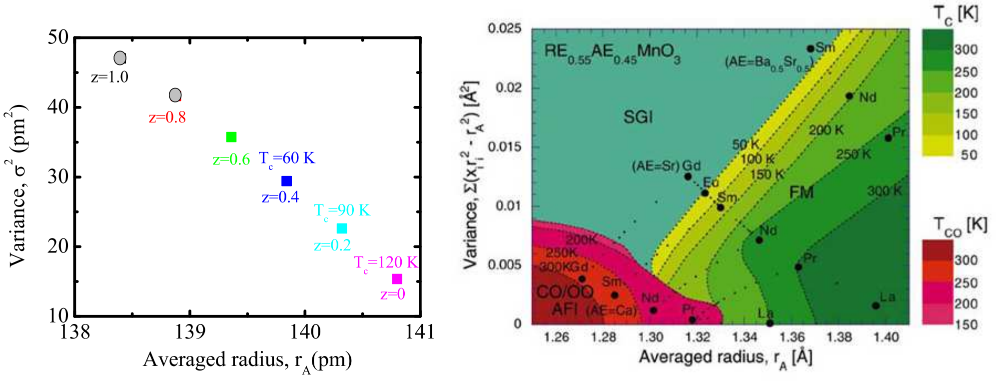

(a) (b)

Figure 3.9: (a) The electronic phase diagram calculated for $(La_{1-z}Pr_z)_{1.2}Sr_{1.8}Mn_2O_7$ crystals in the plane of effective one-electron bandwidth (r_A) and the magnitude of quenched disorder (σ^2). (b) The global phase diagram of $RE_{1-x}AE_xMnO_3$ (x=0.45) crystals in the plane of r_A and σ^2. (after Ref. [8])

imaging suggests that the high field ferromagnetic metallic state is homogenous, as shown in Fig. 3.10(b). [121] Neutron scattering demonstrates that the field-induced ferromagnetic metallic state is very similar to the ferromagnetic metallic state in the double-layer parent compound, $La_{1.2}Sr_{1.8}Mn_2O_7$. [126] Neutron diffraction studies show that local structure (Mn-O bond distances and Mn-O-Mn bond angles) and e_g orbital occupancies change dramatically in magnetic field, directly influencing electron hopping between Mn sites. [118, 122] Figure 3.10(c) demonstrate the lattice distortion and schematic electronic structure of Mn^{3+} ions in $(La_{0.4}Pr_{0.6})_{1.2}Sr_{1.8}Mn_2O_7$ in the field-induced ferromagnetic metallic state at 2 K.

Double layer manganites also attract attention due to potential fundamental investigations as well as practical applications of high energy magnetodielectric effects. The discovery of magnetoelectric coupling and in particular of the magnetodielectric effect, e.g., field-induced change in dielectric constant ϵ_1, has attracted attention

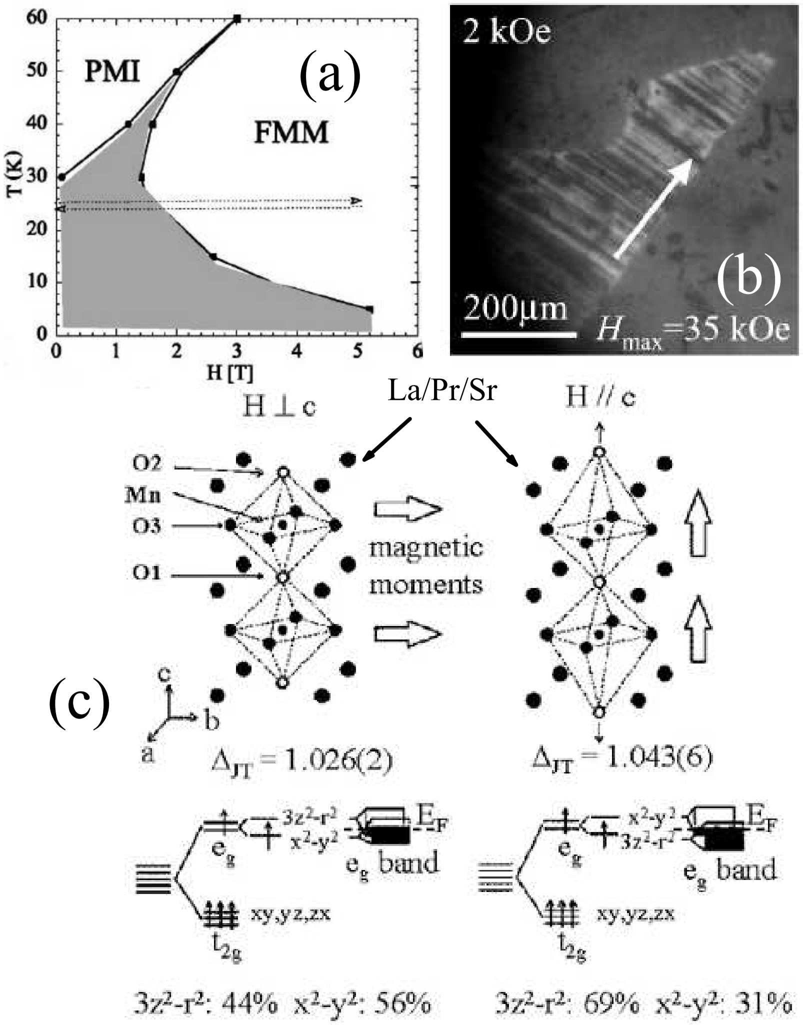

Figure 3.10: (a) Magnetic phase diagram of $(La_{0.4}Pr_{0.6})_{1.2}Sr_{1.8}Mn_2O_7$ in the (H, T) plane established from the magnetic measurements (after Ref. [120]) (b) Magneto-optical images of magnetic stripe structures in the ab plane of $(La_{0.4}Pr_{0.6})_{1.2}Sr_{1.8}Mn_2O_7$ crystals under $H \parallel$=2 kOe after applying H_{max}=35 kOe at 10 K. (after Ref. [121]) (c) Lattice distortion and schematic electronic structure of Mn^{3+} ions in $(La_{0.4}Pr_{0.6})_{1.2}Sr_{1.8}Mn_2O_7$ in the field-induced ferromagnetic metallic state at 2 K. The bottom shows the orbital occupancies of e_g electrons, resulting from polarized neutron diffraction. (after Ref. [122])

due to both potential utilization in multifunctional devices and the desire to understand the fundamental physics underlying multiferroic materials. [127–134] For instance, rare earth manganites such as $TbMnO_3$, $HoMnO_3$, $YMnO_3$, and $DyMn_2O_5$ display sizable static magnetodielectric effects at low temperature, demonstrating that dielectric contrast can be achieved by physical tuning through various magnetic transitions in $H - T$ space. [130, 133, 134] Cubic spinels such as $CdCr_2S_4$ and $HgCr_2S_4$ present even larger static magnetodielectric contrast, attributed to relaxational dynamics driven by magnetization in the field. [127–129] More recently, 300 K magnetodielectric behavior was reported in mixed valent $LuFe_2O_4$ and attributed to charge ordering effects. [132] Mn-doped $BiFeO_3$ also exhibits a potentially tunable room temperature magnetodielectric effect due to enhanced thermal fluctuations near the Néel temperature. [135] Discovery of large magnetodielectric effects in other materials combined with mechanistic understanding of magnetoelectric cross-coupling is of fundamental interest and may hold promise for next-generation memory devices.

Static dielectric properties are typically measured in a parallel plate/capacitance geometry at low frequencies (Hz - MHz). [127, 129, 132] Challenges with this technique include contact problems, potential dead layers, and edge effects. [136, 137] A contactless technique, such as optical spectroscopy, eliminates these issues. At the same time, the electromagnetic spectrum is very broad. This opens the possibility of exploiting changes in ϵ_1 over a wide energy range, essentially as a multi− (rather than single−) channel information storage system. The high energy magnetodielectric effect was recently discovered by our group in several materials including inhomogeneously mixed-valent $K_2V_3O_8$ ($\sim$5% at 30 T near 1.2 eV), Kagomé staircase compound $Ni_3V_2O_8$ ($\sim$16% at 30 T near 1.3 eV), and hexagonal multiferroic $HoMnO_3$ ($\sim$8% at 20 T near 1.8 eV), [9, 37, 138] as shown in Fig. 3.11. In these materials, the high energy magnetodielectric effect derives from spin-lattice-charge

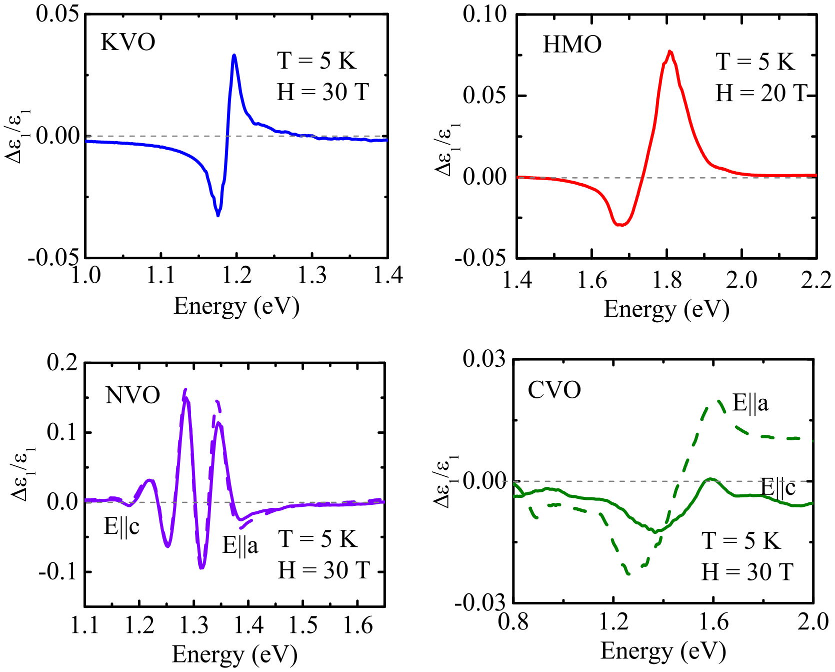

Figure 3.11: High energy magnetodielectric contrast in $K_2V_3O_8$, $HoMnO_3$, $Ni_3V_2O_8$, and $Co_3V_2O_8$. [9, 37, 138]

mixing effects. Part of our continuing strategy to increase dielectric contrast centers on the exploitation of electronic mechanisms such as metal-insulator transitions, charge ordering, and orbital ordering that are known to drive changes in the optical constants. [139, 140] Metal-insulator transitions are common with decreasing temperature, but they are rarely induced by magnetic field. $(La_{0.4}Pr_{0.6})_{1.2}Sr_{1.8}Mn_2O_7$ displays colossal magnetoresistance effects, providing an excellent opportunity for studying the high energy magnetodielectric behavior.

Chapter 4

Lattice and Charge Dynamics of VO_x Nanoscrolls

4.1 Electronic Structure of the Pristine VO_x Nanoscrolls

Figure 4.1(a) displays the 300 K optical absorption spectrum of $(C_8H_{17}NH_3)_y$-VO_x scrolls, calculated from a Kramers-Kronig analysis of the reflectance spectrum. [29] The absorption coefficient was also calculated from the transmittance measurement and we obtain similar results. The spectrum shows several reproducible, fairly prominent, broad bands, which are centered at ∼1.2, 3.9, 5.0, and 7.0 eV. The feature at ∼1.2 eV is assigned as the superposition of both V $d \rightarrow d$ and $V^{4+} \rightarrow V^{5+}$ charge transfer excitations. The features centered at 3.9, 5.0, and ∼7.0 eV are assigned as O $2p \rightarrow$ V $3d$ charge transfer transitions. The inset shows a close-up view of the 5.0 eV excitation which changes modestly with sheet distance. To find the precise peak position of these bands, we set the derivative of the curve equal to zero. This redshift with increasing sheet distance is very unusual, different from traditional

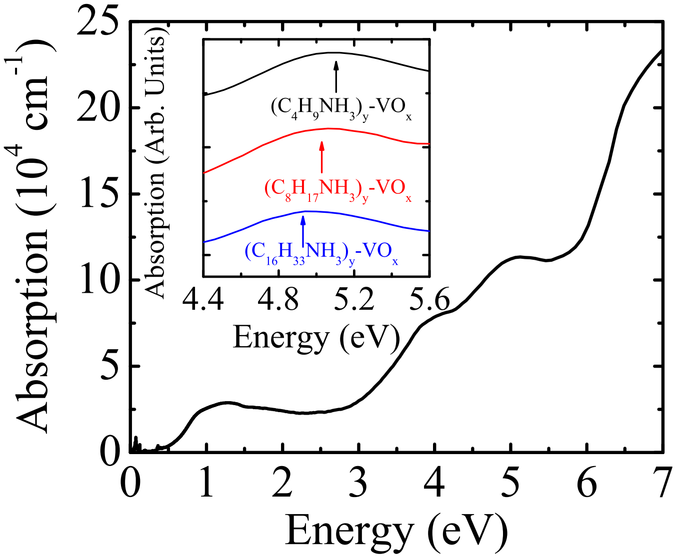

Figure 4.1: 300 K absorption spectrum of $(C_8H_{17}NH_3)_y$-VO_x scrolls. The inset shows a close-up view of one of the high-energy excitations, which changes modestly with sheet distance. In the inset, the curves are offset for clarity. (after Ref. [38])

strain-induced redshifting in other inorganic fullerene-like materials [73–79]. Unfortunately, the challenging crystal structure combined with the lack of theoretical work on the VO_x scrolls precludes a detailed explanation of this trend. We speculate that the 5 eV excitation is strongly polarized in the radial direction. This supposition can be checked, once oriented samples are available, and the result may connect it with the observed sheet distance effect. The optical gap, 2Δ, is determined by making a linear extrapolation of the leading edge of the absorption band down to zero energy. For $(C_8H_{17}NH_3)_y$-VO_x scrolls, we find $2\Delta_{300K}$ $\sim$0.54 eV. At low temperature, the gap sharpens and moves to higher energy. The shape of the optical gap is similar to that of other synthetic metal materials.

As mentioned previously, VO_x nanoscrolls consist of vanadate layers between which organic molecules are intercalated. [26, 27, 63, 88, 91] The size of the amine

Table 4.1: The optical gap of different VO_x nanoscrolls

Material	Sheet Distance(Å)	$2\Delta_{300K}$(eV)	$2\Delta_{4.2K}$ (eV)
$(C_4H_9NH_3)_y$-VO_x	15.82	0.58	0.64
$(C_6H_{13}NH_3)_y$-VO_x	17.37	0.59	0.70
$(C_8H_{17}NH_3)_y$-VO_x	22.98	0.54	0.58
$(C_{12}H_{25}NH_3)_y$-VO_x	27.25	0.57	0.63
$(C_{14}H_{29}NH_3)_y$-VO_x	29.54	0.58	0.68
$(C_{16}H_{33}NH_3)_y$-VO_x	31.38	0.56	0.70
$(C_{18}H_{37}NH_3)_y$-VO_x	35.28	0.54	0.64
Average Value		0.56	0.65

[1] The error bar on 2Δ is 5% at 300 K and 3% at 4.2 K

or diamine template determines scroll winding, providing an opportunity to tune interlayer distance and therefore the size of these materials. The sheet distance dependence of the optical gap is important for understanding the electronic structure of the VO_x nanoscrolls. The effect of tube diameter on the gap has been calculated for several model materials. In GaSe, GaN and MoS_2, 2Δ is predicted to decrease from the bulk value with decreasing tube diameter. [73, 74, 79] This trend can be understood as the strain dependence of the electronic states in these compounds. [87] However, in our materials, changes in the sheet distance, analogous to the aforementioned tube diameter modifications, have no systematic effect on the optical gap (Table 4.1). On average, the gap, 2Δ, is $\sim$0.56 eV at 300 K and $\sim$0.65 eV at 4.2 K. We suspect that the insensitivity of the optical gap to sheet distance is related to the large diameter($\sim$100 nm) of the VO_x nanoscrolls. Note that the tube diameters of GaSe and GaN, for instance, are much smaller than that of the VO_x nanoscrolls, and tube curvature is much more substantial. [73, 79] Upon substitution of different amine templates, there is only modest change in curvature due to the inherently large diameter of the VO_x scrolls.

Comparing the absorption spectrum of $(C_8H_{17}NH_3)_y$-VO_x nanoscrolls to that of other vanadates, we find that the VO_x scrolls show a striking resemblance to several model materials, including VO_2, α'-NaV_2O_5, and $Na_2V_3O_7$, (Fig. 4.2) [141–145] despite substantial differences in structure and charge. The absorption spectrum also resembles that of the molecule-based magnet $K_6[V_{15}As_6O_{42}(H_2O)]\cdot 8H_2O$. [146] In bulk VO_2, tubular $Na_2V_3O_7$, and molecular $K_6[V_{15}As_6O_{42}(H_2O)]\cdot 8H_2O$, all transition metal atoms have a +4 charge. In these materials, the feature centered at ∼1.2 eV has been assigned as a localized $d \rightarrow d$ transition between ground and excited states, split by a crystal field. [144–146] Assignment of the 1 eV excitation and the higher-energy sidebands in ladder-like α'-NaV_2O_5, however, has been controversial due to the mixed-valence character of this material. [141, 142, 147] The 1 eV excitation is currently attributed to $V^{4+} \rightarrow V^{5+}$ charge transfer excitations on the V-O-V rung. [142, 147]

The VO_x nanoscrolls are also mixed-valent, suggesting that the feature at ∼1.2 eV may share certain characteristics with α'-NaV_2O_5. In our case, however, the band seems to arise from two sources, and we attribute it to the superposition of both V $d \rightarrow d$ and $V^{4+} \rightarrow V^{5+}$ charge transfer excitations. Evidence for this dual assignment comes from both spectral and structural data. From the spectral point of view, both the band shape as well as the trend with decreasing temperature point toward contributions from two very different excitations in the $(C_8H_{17}NH_3)_y$-VO_x scrolls. At 300 K, the band consists of two peaks: a weak feature at ∼0.8 eV and a stronger feature centered at 1.2 eV. The 0.8 eV feature blueshifts with decreasing temperature and combines with the 1.2 eV band at base temperature. It is useful to recall that charge transfer transitions often exhibit substantial temperature dependence, whereas on-site $d \rightarrow d$ excitations show more subtle effects. This difference suggests that the feature centered at 0.8 eV can be attributed to a $V^{4+} \rightarrow V^{5+}$ charge transfer

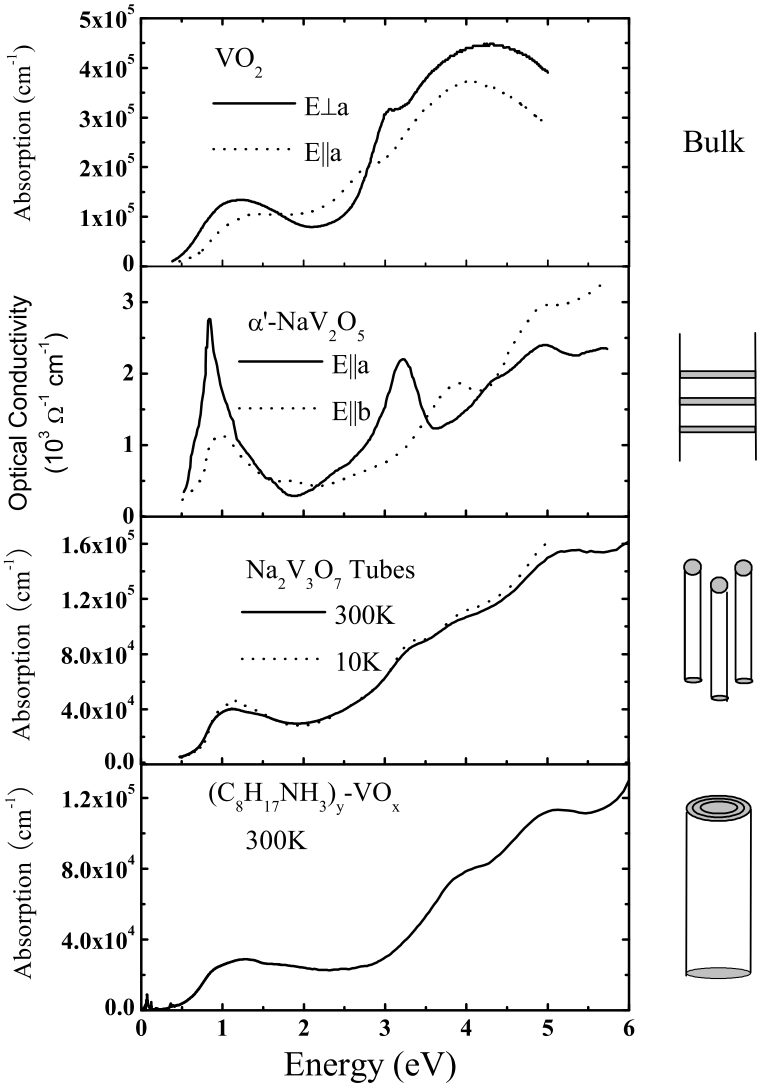

Figure 4.2: 300 K optical absorption spectrum of $(C_8H_{17}NH_3)_y$-VO_x scrolls as compared with the room temperature absorption spectra of VO_2, [143] the polarized optical conductivity of α'-NaV_2O_5 [141, 144] and the variable temperature absorption spectra of $Na_2V_3O_7$. [145] (after Ref. [38])

excitation and the larger 1.2 eV feature assigned as a V $d \rightarrow d$ excitation. Note that the $d \rightarrow d$ excitation is formally La Porte forbidden. It appears in the spectrum of the VO_x scrolls due to symmetry breaking around the chromophore, which relaxes the selection rules on excitations within the d manifold. This kind of selection rule relaxation appears in a number of model vanadates. [143–146] Such a process is also allowed due to the strong hybridization between V $3d$ and O $2p$ orbitals. Structural data also supports the dual assignment of the ∼1.2 eV band. As discussed previously, the mixed-valent chromophore units display both edge- and corner-sharing arrangements. [46, 88] Only the edge-sharing units are likely to engage in charge transfer with appreciable oscillator strength; corner-sharing will likely not provide sufficient overlap for related excitations to appear in the spectrum. Combined with the La Porte forbidden on-site V $d \rightarrow d$ excitations, we can therefore account for the two oscillators that constitute the ∼1.2 eV band.

The higher energy spectral features of the VO_x nanoscrolls also display strong similarities with the aforementioned model vanadates, but the response is not identical. (Fig. 4.2) The structures at 3.9, 5.0 and ∼7.0 eV, previously identified as O $2p \rightarrow$ V $3d$ charge transfer excitations in the VO_x nanoscrolls, are present in the spectra of the bulk, ladder, and molecular materials. [141–146] However, the ∼3.2 eV excitation that appears in the response of all other vanadates, is not apparent in the spectrum of $(C_8H_{17}NH_3)_y$-VO_x (Fig. 4.2) or the other VO_x nanoscrolls. Future electronic structure calculations may be able to explain the absence of this feature in the VO_x.

Armed with an understanding of the electronic properties of the VO_x nanoscrolls, we are now in a better position to shead light on the mechanism of optical limiting behavior in these materials. [83] Briefly, the findings of Xu *et. al.* are that optical limiting is observed when the system is pumped at 532 nm (2.3 eV) but not when the system is pumped at 1064 nm (1.16 eV). [83] This is obviously different from the broadband nature of the limiting effect in carbon. [148, 149] Based upon these observations and the assignment of a 460 nm (2.7 eV) optical gap, the authors attribute the optical limiting effect to a two-photon process. [83] In this work we show, however, that the average optical gap of the VO_x nanoscrolls is $\sim$0.56 eV at 300 K, much less than that assumed by Xu *et. al.* The proposed two-photon mechanism [83] is therefore not consistent with this new picture of the electronic structure, suggesting that it may be useful to consider alternate mechanisms for the optical limiting behavior in these materials. It is also useful to note that, even if we assume that the band structure and gap assignment of the previous authors is correct, alternate explanations may be applied to their results. For instance, 532 nm excitation may promote a carrier into a virtual or "trapped" state, close to the conduction band, so that subsequent thermal excitation can take place. Low-temperature measurements could rule out this possibility. Pumping at a different energy, where thermal processes are unlikely (for instance 1.9 eV), may also help to test the plausibility of this mechanism. Finally, we note that 1064 nm (1.16 eV) light will be absorbed into the band centered at $\sim$1.2 eV (Fig. 4.1(a)). For some reason, this seems to be an inappropriate choice from the point of view of optical limiting, perhaps forcing the system into a "wrong" excited state. On the other hand, 532 nm (2.3 eV) pumping successful generates an optical limiting response in the VO_x scrolls, a result that may be related to the relatively low-absorption window of the VO_x in this energy range. Electronic structure calculations, once available, may offer additional mechanistic insight.

4.2 Vibrational Structure of the Pristine VO_x Nanoscrolls

4.2.1 Sheet Distance Effects on the Vibrational Response of the VO_x Nanoscrolls

Figure 4.3(a) displays the 300 K vibrational response of $(C_6H_{13}NH_3)_y$-VO_x nanoscrolls. The far- and middle-infrared absorption spectra display a number of modes that can be conveniently divided into four groups. These features are located at ∼113 cm^{-1}, between 150 - 400 cm^{-1}, between 400 - 1000 cm^{-1}, and above 1000 cm^{-1}. The modes above 1000 cm^{-1} are attributed to those of the amine template. Using previous mode assignments of other model vanadates including V_2O_5, α'-NaV_2O_5, $Na_2V_3O_7$, and $K_6[V_{15}As_6O_{42}(H_2O)]\cdot 8H_2O$ as well as the current understanding of VO_x structure, [46, 88] the clusters located between 150 - 400 cm^{-1} and 400 - 1000 cm^{-1} are attributed to V-O bending and stretching, respectively. [145, 146, 150] There are two distinct axial stretching modes, a consequence of the substantial difference in the two axial V-O bond lengths, one of which is extremely long and weak. As expected, the axial modes are relatively insensitive to tube diameter effects. Selected equatorial stretching modes do, however, depend on the sheet distance, as detailed below. This effect is somewhat analogous to the size effects that modulate the structural phase transition in VO_2 nanoparticles. [151] The isolated feature at 113 cm^{-1} (inset of Fig. 4.3(a)) is assigned as the screw-like motion of scrolls and is also discussed in detail below. Our mode assignments are summarized in Table 4.2.

We find that selected vanadium-oxygen stretching modes are very sensitive to tube curvature. Figure 4.3(b) shows a close-up of view of two V-O-V stretching modes as a function of sheet distance. The spectra have been normalized so that it is meaningful to compare the integrated area. The peak centered at ∼585 cm^{-1}

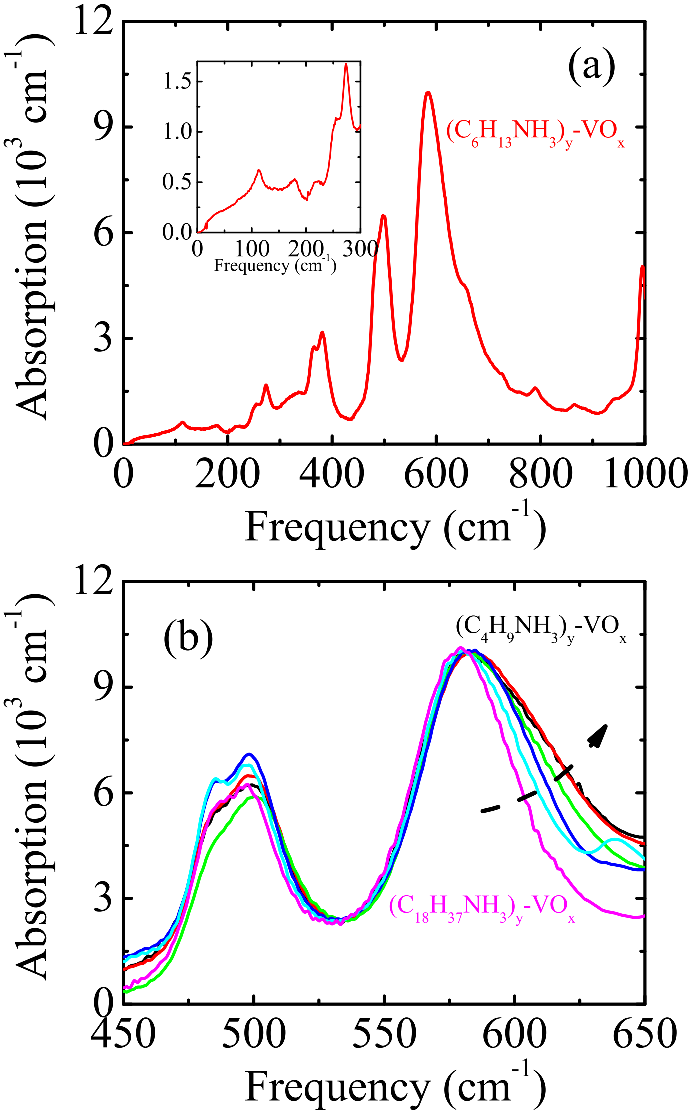

Figure 4.3: (a) 300 K infrared absorption spectrum of $(C_6H_{13}NH_3)_y$-VO_x nanoscrolls. The inset shows a magnified view of the far-infrared response. (b) Close-up view of two V-O-V stretching modes as a function of sheet distance in the nanoscrolls. (after Ref. [38])

Table 4.2: Vibrational modes of $(C_6H_{13}NH_3)_y$-VO_x nanoscrolls

Peak Frequency (cm^{-1})	Assignment
113	Screw-like motion of scroll
179	V-O bending
215	V-O bending
255, 273[1]	V-O bending
341, 366, 381[1]	V-O bending
486, 498[1]	V-O-V (weak axial) stretching [2]
585[1],653,727	V-O-V (equatorial) stretching
790	V-O-V (equatorial) stretching
866	V-O-V (equatorial) stretching
945, 995[1]	V-O (strong axial) stretching [3]

[1] Indicates that the main feature in a multi-peak cluster.
[2] Oxygen is shared by two vanadium.
[3] Oxygen is not shared by two vanadium.
[4] The features above 1000 cm^{-1} are related to the motion of the amine template.

appears to broaden with decreasing sheet distance. This widening is somewhat of an optical illusion, as discussed below. More modest sheet distance effects are observed in the $\sim$490 cm^{-1} feature. To quantify the changes in the vibrational properties with sheet distance, we fit the various spectra with five model oscillators over the frequency range of interest, 450 - 700 cm^{-1}. Figure 4.4(a) gives an example of a typical fit. Here, the fifth oscillator works as a background.

The peak positions and integrated areas of the four most important oscillators are shown in Figs. 4.4(b) and (c) as a function of sheet distance. The trends associated with the $\sim$585 cm^{-1} feature are notable. The center peak positions of oscillators 3 and 4 converge by $\sim$12 cm^{-1} over the range of our investigation $(C_4H_9NH_3)_y$-VO_x to $(C_{18}H_{37}NH_3)_y$-VO_x nanoscrolls), whereas the center positions of oscillators 1 and 2 display a more modest frequency change, converging by only $\sim$2 cm^{-1}. The integrated areas of oscillators 3 and 4 increase and decrease with increasing sheet

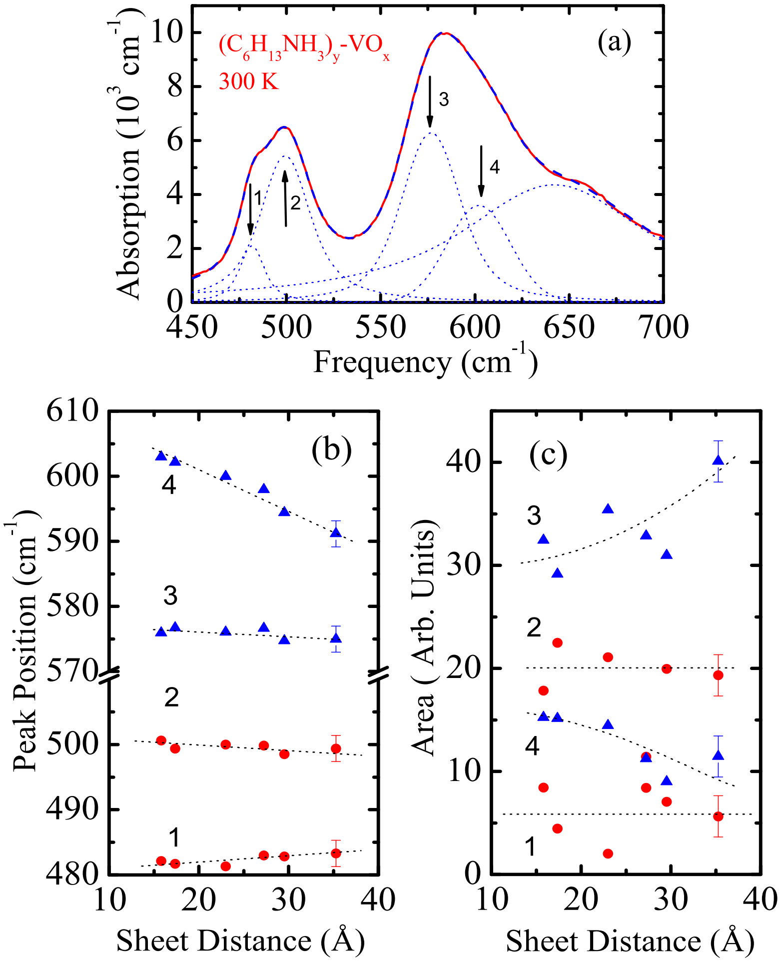

Figure 4.4: (a) Example fit of the 300 K spectrum of $(C_6H_{13}NH_3)_y$-VO_x nanoscrolls in the range of the V-O-V stretching modes. Dashed lines show the model Voigt oscillators used in the fit. (b) Peak positions of the fitted oscillators as a function of sheet distance. (c) Integral areas of the fitted oscillators vs. sheet distance. Dashed lines guide the eye. (after Ref. [38])

distance, respectively, indicating a transfer of spectral weight from the high-energy side band (oscillator 4) to the main peak (oscillator 3). This trend is consistent with more pronounced (limited) site distinction on smaller (larger) tubes. In contrast, the integrated areas of oscillators 1 and 2 (associated with the $\sim$490 cm^{-1} feature) are insensitive to sheet distance effects.

We attribute these trends to tube curvature effects. From the structural point of view, tube curvature increases as sheet distance decreases (from $(C_{18}H_{37}NH_3)_y$-VO_x to $(C_4H_9NH_3)_y$-VO_x). When a two-dimensional sheet is wrapped into the tubular morphology, equatorial bond lengths and their motion will be especially sensitive to the degree of radial distortion. Greater distortion will manifest itself in the spectrum in several ways, typically with mode shifting, linewidth changes, and site-symmetry breaking. All are observed in the VO_x nanoscrolls. (Fig. 4.3(b)) The sensitivity of the 580 cm^{-1} feature to sheet distance modification is therefore directly attributable to the directional character of the V-O-V equatorial stretching motion and the distortion of the nanoscroll. The overall redshifting with increasing sheet distance, characteristic of a more relaxed lattice, is especially pronounced. In contrast, axial bond lengths (and their associated vibrational motion) are modified only subtly due to distortion. Sheet distance effects on the $\sim$490 cm^{-1} mode (related to the very long V-O-V axial stretching motion in the sheet) are in line with this supposition.

Previous far-infrared studies of other model vanadates indicate that the lowest-frequency modes are not due to localized vibrations of vanadium and oxygen atoms, but instead are related to more complicated, long-range external motions such as lattice motion, liberation or rattling. [150, 152] For instance, the 74 cm^{-1} feature in V_2O_5 is assigned as a librational mode of the $(V_2O_5)_n$ chains, [152] the 90 cm^{-1} mode in α'-NaV_2O_5 is attributed to translation of V_2O_5 units along the c axis, [150] the 88 cm^{-1} mode in $Na_2V_3O_7$ is connected with rattling mode of Na^+ inside the tubes, [145] and the 85 cm^{-1} feature in $K_6[V_{15}As_6O_{42}(H_2O)]\cdot 8H_2O$ is assigned as a rattling mode of H_2O inside the vanadium oxide cage. [146] None of these options offer a plausible assignment for the 113 cm^{-1} feature in the VO_x nanoscrolls. However, the morphology of the VO_x nanoscrolls suggests an interesting alternative. Theoretical and experimental work indicate that, in the tubular morphology, a low-frequency radial breathing mode is expected. For instance, in single-wall carbon nanotubes and BN tubes, the frequency of the radial breathing mode is inversely proportional to the radius of the nanotube, independent of the nanotube structure. [81, 153] For the BN tubes, this redshifting is predicted to be substantial, moving from 600 cm^{-1} to 100 cm^{-1} as tube radius increases from 2.5 to 10 Å. [81] A peak at 113 cm^{-1} is therefore the correct order of magnitude for assignment as a radial breathing mode in the VO_x nanoscrolls. Note that usually radial breathing mode in nanotubes is totally symmetry and is only Raman active. The screw-like motion of the VO_x scrolls, which corresponds to the breathing mode in regular nanotubes, will be infrared active. We therefore assign the 113 cm^{-1} feature to screw-like motion in VO_x nanoscrolls. Considering the theoretical predictions, it is somewhat disappointing to find that the 113 cm^{-1} feature does not display any sheet distance dependence. We attribute this lack of sensitivity to the small difference of sheet distances compared with large tube diameters.

4.2.2 Temperature and Magnetic Field Effects on the VO_x Nanoscrolls

Physical tuning with temperature, applied magnetic field, or pressure provides a way to manipulate competing interactions in a material. For instance, temperature is well known to drive structural phase transitions, magnetic fields can modify dimensionality or break symmetry, and pressure can increase three-dimensional interactions and overlap. In a number of model vanadates, the effect of temperature on the ground state has received a great deal of attention. In particular, a semiconducting to metal transition has been observed at ∼350 K in bulk VO_2, VO_2 nanoparticles and nanorods, as well as the model oxides VO and V_2O_3. [151, 154–156] Substantial changes in the far-infrared response accompany the 350 K transition. In order to search for evidence of a similar semiconductor to metal transition in a material with a tubular morphology, we investigated the variable temperature vibrational properties of $(C_6H_{13}NH_3)_y$-VO_x nanoscrolls. Typical data is shown in Fig. 4.5(a).

At the base temperature, vibrational modes are sharp, and quite a bit of fine structure is observed. The equatorial V-O-V modes are more sensitive to temperature than the axial modes. The 113 cm^{-1} mode corresponding to the low-energy screw-like motion of the scrolls sharpens and blue shifts slightly at 4 K. We emphasize that $(C_6H_{13}NH_3)_y$-VO_x nanoscrolls are semiconducting at all temperatures. There is no evidence of a transition to a highly conducting metallic state. Extrapolation of $\sigma_1(\omega)$ to zero frequency provides an estimate of the dc conductivity. From the upper inset of Fig. 4.5(a), we extract $\sigma_{dc} \approx 0.1$ cm^{-1} at 4 K, whereas it is somewhat higher (≈ 2 cm^{-1}) at 450 K. The lower inset of Fig. 4.5(a) displays the low-frequency values of the optical conductivity vs. temperature. Although the low-frequency ac conductivity rises with increasing temperature, $(C_6H_{13}NH_3)_y$-VO_x nanoscrolls remains essentially semiconducting over the full temperature range of our investigation. No dramatic semiconducting to metallic state transition is observed, different from the other aforementioned vanadium oxides.

It is interesting to speculate on possible explanations for the very weak semiconductor to metal transition in the VO_x nanoscrolls. At the present time, the leading candidates are: (1) the presence of the amine templates, which somehow interferes with the establishment of a conducting ground state, (2) the strong Coulomb interac-

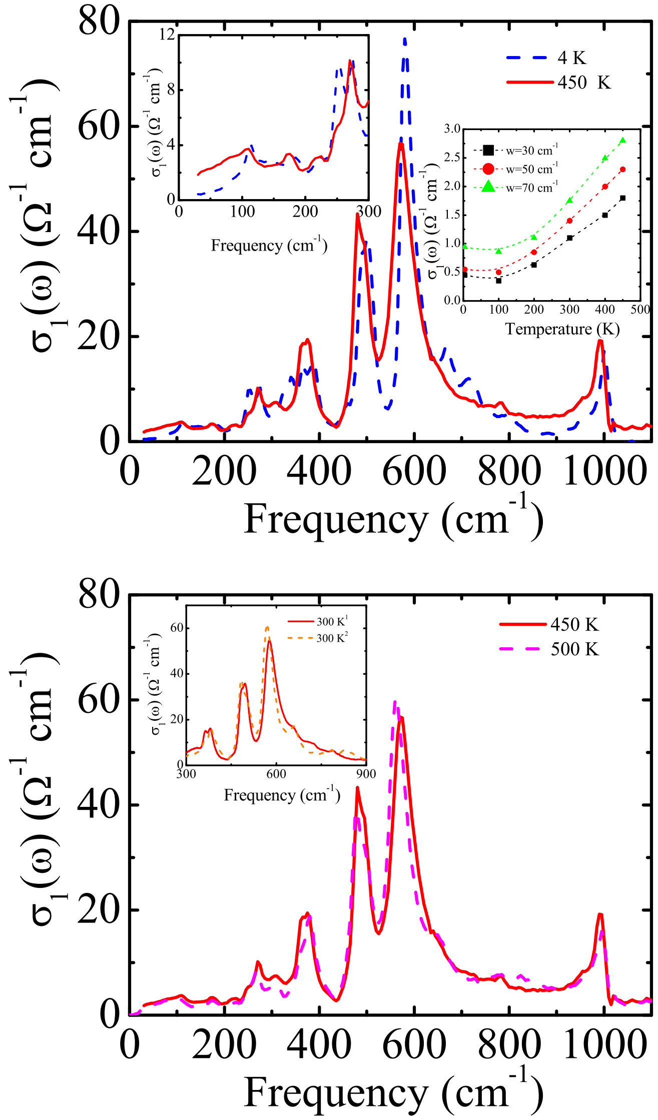

Figure 4.5: (a) Optical conductivity spectrum of $(C_6H_{13}NH_3)_y$-VO_x nanoscrolls at 4 and 450 K. The upper inset shows a magnified view of the far infrared response. The lower inset shows the low-frequency optical conductivity as a function of temperature. (b) High-temperature optical conductivity spectrum of $(C_6H_{13}NH_3)_y$-VO_x nanoscrolls. Degradation occurs above 450 K. The inset shows a comparison of the 300 K spectrum, before and after heating to 500 K. Clear evidence of damage is observed. (after Ref. [39])

tions in the VO_x nanoscrolls give rise to a Hubbard gap and thus, a semiconducting state over a wide temperature range, and (3) the semiconductor to metal transition is preempted by the high-temperature decomposition. High pressure infrared measurements would allow a test of the second hypothesis, as pressure can be used to tune the electron correlations and eliminate the Hubbard gap. It is useful to note that the materials in our present investigation are in powder form and therefore present an isotropic response. If the conductivity characteristics of the VO_x nanoscrolls are anisotropic, a different result, more characteristic of a one-dimensional metal, might be obtained on oriented or “single tube” samples.

Magneto-infrared measurements were carried out at the National High Magnetic Field Laboratory in Tallahassee, FL to investigate the effects of physical tuning with an applied magnetic field. These experiments were motivated by the fact that many vanadates are well-known to display novel high field effects, [147] especially in materials with mixed oxidation states. However, in fields up to 17 T, the VO_x nanoscrolls display no field-induced modifications in the infrared response (30 - 2000 cm^{-1}). Any magneto-elastic coupling in the VO_x nanoscrolls must therefore take place at a higher energy scale, if it exists at all.

According to recent thermogravametric analysis results, [64] there is a loss of tube integrity when the VO_x nanoscrolls are heated above $\sim$470 K. Inspection of the data in Fig. 4.5(b) demonstrates that the vibrational response is a sensitive and microscopic indicator of the degradation. There are a number of clear spectral changes that appear in the damaged material. These include a reduction in intensity and a blue-shift of the high-energy axial stretching mode at 995 cm^{-1}, a notable blue-shift in the 595 cm^{-1} feature, and systematic changes between 250 and 400 cm^{-1}, features attributed to V-O bending motion (Table 4.2).

The mechanism of high-temperature degradation of the VO_x nanoscrolls does not seem to be merely burning and decomposition of the amine. According to the variable temperature vibrational response, the inorganic framework itself breaks down above 470 K. There may be partial removal of oxygen in this process. The inset of Fig. 4.5(b) shows a comparison of the 300 K spectrum of $(C_6H_{13}NH_3)_y$-VO_x nanoscrolls before and after heating above the decomposition point. Clear evidence of damage is observed.

4.3 Bound Carrier Excitation in Ion Substituted Nanoscrolls: Mn-VO_x

Figure 4.6(a) shows the optical conductivity of the pristine VO_x scrolls and the Mn^{2+} substituted compounds at room temperature. The pristine scrolls display semiconducting behavior, with clearly resolved vibrational modes below 1000 cm^{-1} and a low background conductivity. As mentioned previously, these modes originate from V-O-V axial and equatorial stretching, V-O bending, and screw-like motions of the scrolls. Subtle spectral changes occur when the amine template is exchanged for Mn^{2+}, Zn^{2+}, or Na^+. In the Mn^{2+} substituted compound (Fig. 4.6(a)), the optical conductivity develops a broad electronic background in the far infrared region, with strong phonons riding top of this excitation. The Fano-like lineshapes of several phonons, especially those near 250 and 380 cm^{-1}, indicate that this background is electronic in nature. [157] This localized electronic excitation has a width of $\sim$400 - 500 cm^{-1}. Such a bound carrier response is characteristic of a weak or “bad” metal rather than a traditional Drude metal and has been observed in other complex oxides. [43, 158–160] Extrapolating $\sigma_1(\omega)$ to zero frequency, we find $\sigma_{dc} \approx 1\ \Omega^{-1}$ cm^{-1}. We obtain similar results at low temperature, (Fig. 4.6(b)) suggesting that the vanadium centers in both pristine and ion-exchanged scrolls are charge dispro-

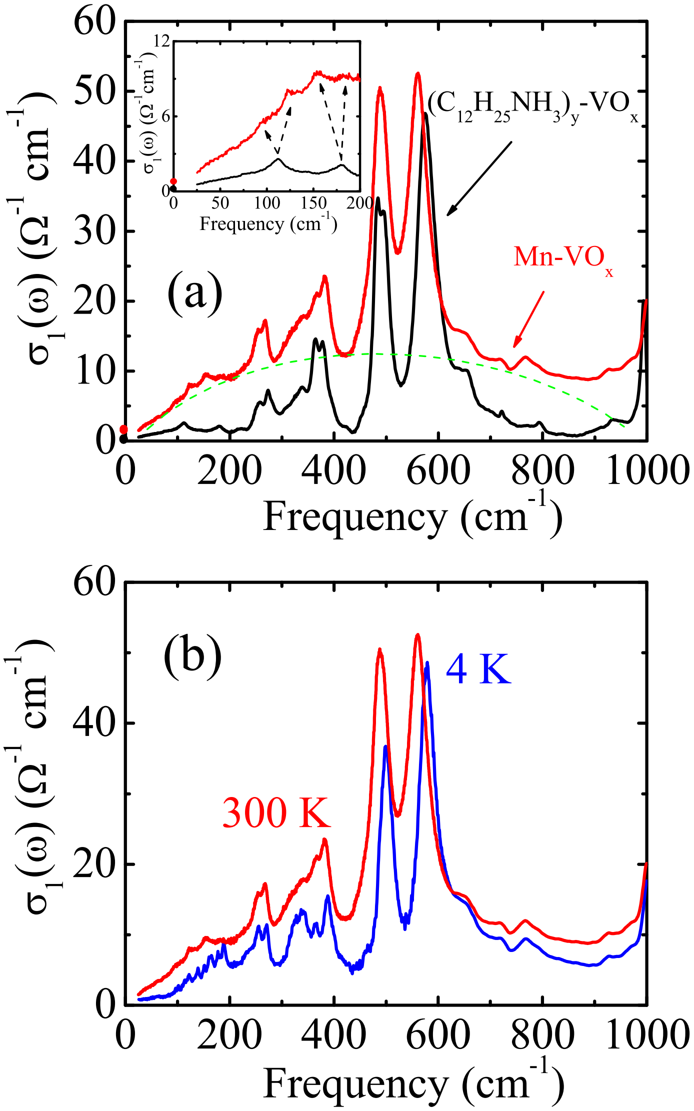

Figure 4.6: (a) 300 K optical conductivity of pristine VO_x scrolls and the Mn exchanged compound in the far-infrared regime. The dotted line guides the eye, highlighting the additional bound carrier contribution in the substituted scrolls. The inset shows a magnified view of the low-frequency response of pristine and Mn exchanged scrolls. The extrapolated dc conductivity is indicated by filled circles at $\omega = 0$ in both panels. (b) Optical conductivity spectra of Mn^{2+} substituted VO_x nanoscrolls at 4 and 300 K. (after Ref. [40])

portionated, with V^{4+} and V^{5+} ions rather than the mixed valent state ($V^{4.5+}$) that might be anticipated for a highly conducting material.

Based on the observation of a far infrared bound carrier localization, the ion exchange processes does add carriers to the scrolled vanadates. The carriers are not, however, mobile in the ion substituted scrolls. Pristine $(C_{12}H_{25}NH_3)_y$-VO_x scrolls are frustrated spin liquids as well as Mott insulators. [47] Within the rigid band model, the "doping" or ion exchange process has been predicted to transform the insulator to a good conductor by modifying the number of carriers and simply shifting the Fermi energy. [47] The data in Fig. 4.6 are, however, in direct contradiction to this expectation. The metal substituted scrolls display charge localization rather than a free carrier response, indicating that these materials are bad metals in the bulk form. Single scroll STM measurements are in progress to complement this spectroscopic work.

Improved understanding of the ion exchange chemistry as well as first principles electronic structure calculations of the substituted vanadium oxide nanoscrolls is clearly needed. The lack of detailed structural information unfortunately impedes both efforts. Figure 4.7 displays a schematic representation of several possible band structures that may evolve during the metal exchange process. The pristine scrolls, diagrammed in Fig. 4.7(a), are Mott insulators, with an $\sim$0.5 eV band gap. [38] This gap derives from a superposition of both V on-site d to d excitations and V^{4+} to V^{5+} charge transfer excitations. [38] There are several possible ways to inject charge into the system. One scenario, proposed by Krusin-Elbaum *et al.*, involves the reconstruction of electronic structure within the rigid band model. [47] As diagramed in Fig. 4.7(d), the essential physics of the electron or hole "doping" process can be modeled by changing the number of carriers and shifting the Fermi energy to the appropriate position. [47] This picture can not, however, account for the weakly

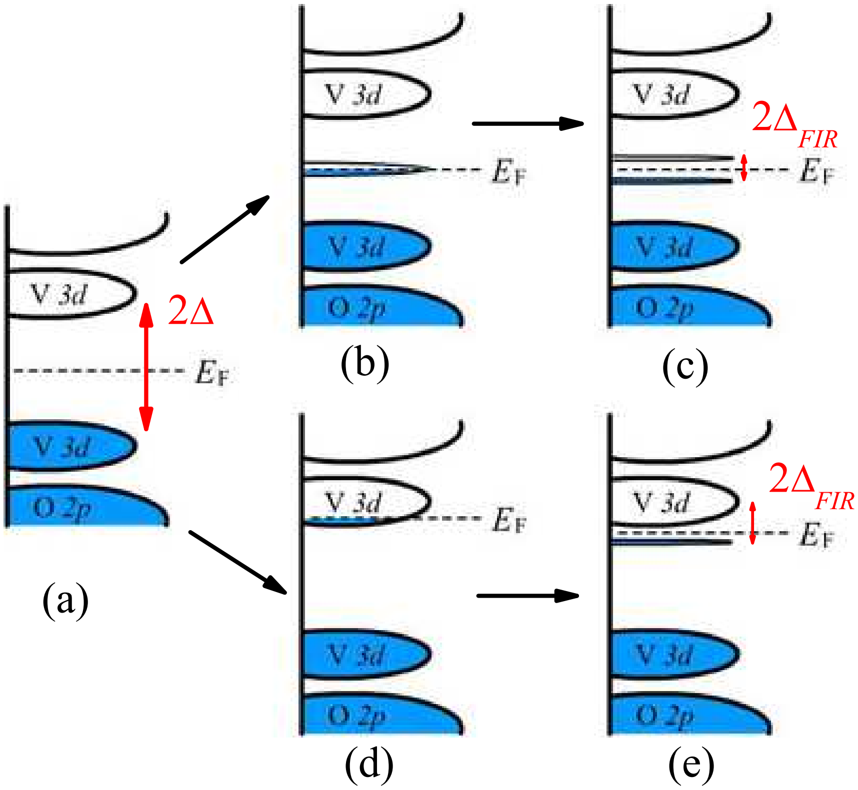

Figure 4.7: Schematic representation of possible electronic structure changes emanating from the ion exchange process in the scrolled vanadates. (a) Band structure of pristine vanadium oxide nanoscrolls. Here, 2Δ denotes the $\sim$0.5 eV band gap. [38] (b) Schematic view in which ion exchange adds carriers to a new defect-level band that forms near E_F. (c) Cartoon view in which the new charge defect band splits due to electron-electron interactions and/or chemical disorder effects. Here, $2\Delta_{FIR}$ represents the low energy bound carrier excitation. This structure will likely have narrow bandwidth. (d) Alternate approach to the exchange process in which ion exchange adds carriers within the rigid band model. [47] (e) Schematic view in which the V $3d$ band splits due to electron-electron interactions and/or chemical disorder effects. Here, $2\Delta_{FIR}$ represents a possible low energy excitation, although it will have a wider band width than in (c) due to joint density of states effects. (after Ref. [40])

metallic spectral response of the Mn^{2+} substituted nanoscrolls. Even if the partially-filled band of Fig. 4.7(d) is allowed to split due to electron-electron interactions and/or chemical disorder effects (Fig. 4.7(e)), the resulting low energy excitation would be fairly broad due to joint density of states effects in which the narrow occupied level below E_F is mixed with the wider empty valence band arising from the V $3d$ states. An alternate approach is to allow the ion exchange process to introduce a new band, essentially a "defect level" that derives from the charging process (Fig. 4.7(b)). Splitting of this already narrow band might also occur due to charge disproportionation, electron-electron interactions, or disorder effects (Fig. 4.7(c)). As always, the Fermi level is repositioned between conduction and valence bands. A dipole-allowed transition between these levels would be consistent with a localized charge carrier excitation rather than a traditional metallic response in the low energy region of the optical conductivity. Such a feature would be relatively narrow, consistent with the 400 - 500 cm^{-1} linewidth observed in the spectrum of Mn^{2+} substituted scrolls. At this time, the scheme diagramed in Fig. 4.7(a-c) is in the best accord with our experimental results.

Comparison of mode frequencies with those of model compounds where the valence is known often allows a microscopic analysis of local charge and bonding behavior. Thus, careful examination of vibrational shifting and splitting mode patterns can also provide information on the ion exchange process, although in this case, we must account for both charge and structural modifications. This analysis is possible because vibrational features are observed in both the pristine and ion exchanged materials. In the pristine vanadium oxide nanoscrolls, the mode at $\sim$575 cm^{-1} is assigned as the V-O-V equatorial stretch. [38] This mode is very sensitive to curvature, widening as the size of the amine template is reduced, characteristic of a more strained lattice. [38] The V-O-V equatorial stretching mode (Fig. 4.6) redshifts with ion substitution, moving from $\sim$575 cm^{-1} in the pristine scrolls, to $\sim$570 cm^{-1} in Na^{+} and $\sim$560 cm^{-1} in Mn^{2+} exchanged compounds. Shifts in peak position are observed in other doped and intercalated vanadates. [161,162] For instance, modification of the V^{4+}:V^{5+} ratio in Ti-substituted α'-NaV$_2$O$_5$ redshifts the V-O stretching mode from 525 cm^{-1} in pristine α'-NaV$_2$O$_5$ to 521 cm^{-1} in the Ti^{4+} doped compound. [162] From the structural point of view, the redshift in the scrolled vanadates is unexpected. X-ray results indicate that the interlayer distance decreases as the smaller metal ions replace the larger amines. [91] The V-O-V equatorial stretch might therefore be expected to widen in the substituted scrolls due to their increased curvature, but the center peak position ought to be relatively insensitive to size. [38] Ion exchange also adds charge to the scrolls. We attribute changes in the V-O-V equatorial stretching mode position (Fig. 4.6) to charging effects which overcome the aforementioned local strain that tends to widen and slightly harden the V-O-V resonance. This overall softening trend ($\sim$575 cm^{-1} in the pristine scrolls to $\sim$560 cm^{-1} in the Mn^{2+} substituted compound) confirms that the ion exchange process adds carriers to the scrolls. The sharp, unscreened vibrational features in the ion substituted scrolls show, however, that the carriers are not mobile, consistent with the observation of a bound carrier excitation in the far infrared. The metal exchange process also leads to some chemical disorder, as evidenced in the splitting of a low frequency bending motion ($\sim$180 cm^{-1}) and the screw-like mode at $\sim$113 cm^{-1} that is analogous to the radial breathing mode in carbon nanotubes (inset, Fig. 4.6). Disordered Cu^{2+} exchanged nanoscrolls have been reported recently. [94]

Figure 4.8 displays the 300 K optical conductivity of the pristine VO$_x$ scrolls and the Mn^{2+} exchanged compound over a broader energy range. With the exception of the aforementioned bound carrier excitation localized in the far infrared (Fig. 4.6), the spectrum of the ion exchanged scrolls is similar to that of the pristine compound,

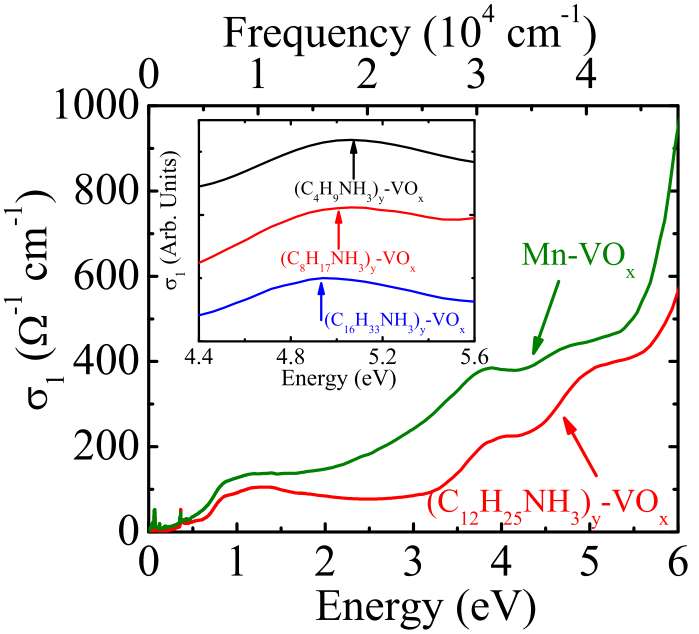

Figure 4.8: Expanded view of the 300 K optical conductivity of pristine VO$_x$ scrolls and the Mn exchanged compound. The inset shows a close-up view of the ∼5 eV excitation, which changes modestly with sheet distance in the unsubstituted scrolls. [38] In the inset, the curves are offset for clarity. (after Ref. [40])

in line with the fact that these excitations derive from the vanadium oxide framework. [38] Both materials display similar ∼0.5 eV optical gaps and excitations centered near 1 eV that derive from a superposition of V d to d on-site excitations and V^{4+} to V^{5+} charge transfer excitations. [38] The O p to V d charge transfer excitations at ∼3.9 and ∼5.0 eV redshift with ion substitution. That this is a charge (rather than size) effect is evident from a comparison of the data in the inset of Fig. 4.8. Here, the excitation centered at ∼5.0 eV shifts to higher energy as the size of the amine template decreases (corresponding to a reduction in the interlayer distance). The 3.9 eV feature does not change with curvature. [38] The Mn^{2+} substituted scrolls display the opposite trend, indicating that charge effects also modify the charge transfer excitations. First principles electronic calculations will offer microscopic insight on this problem.

Chapter 5

Infrared and Optical Studies of $VOHPO_4 \cdot \frac{1}{2}H_2O$

5.1 Characterization of $VOHPO_4 \cdot \frac{1}{2}H_2O$ Crystals

Our $VOHPO_4 \cdot \frac{1}{2}H_2O$ single crystals were characterized by magnetic susceptibility and ESR. Figure 5.1 (a) displays the molar susceptibility χ as a function of temperature. Here the units of χ are $cm^3\ mol^{-1}$; each formula unit of $VOHPO_4 \cdot \frac{1}{2}H_2O$ contains one vanadium ion. Some qualitative features are noteworthy. Most striking is that the results for χ are extremely similar for the two orthogonal crystal orientations, differing by $\sim$1%. Second, the susceptibility drops to quite low values near 10 K, before exhibiting an upturn at lower temperature. The signal at the lowest temperatures varies as $\sim$1/T, and is attributed to a "Curie tail" of isolated paramagnetic impurity ions. This was also observed in the previous study of polycrystalline $VOHPO_4 \cdot \frac{1}{2}H_2O$, [50] but it was much larger, indicating that the signal is not intrinsic to the material. Using results of a Curie analysis of the data at low temperatures (T $<$ 10 K), we can subtract this impurity component and isolate the susceptibility of the pure material. Isolated dimer, [50, 163] alternating chain [164], and coupled al-

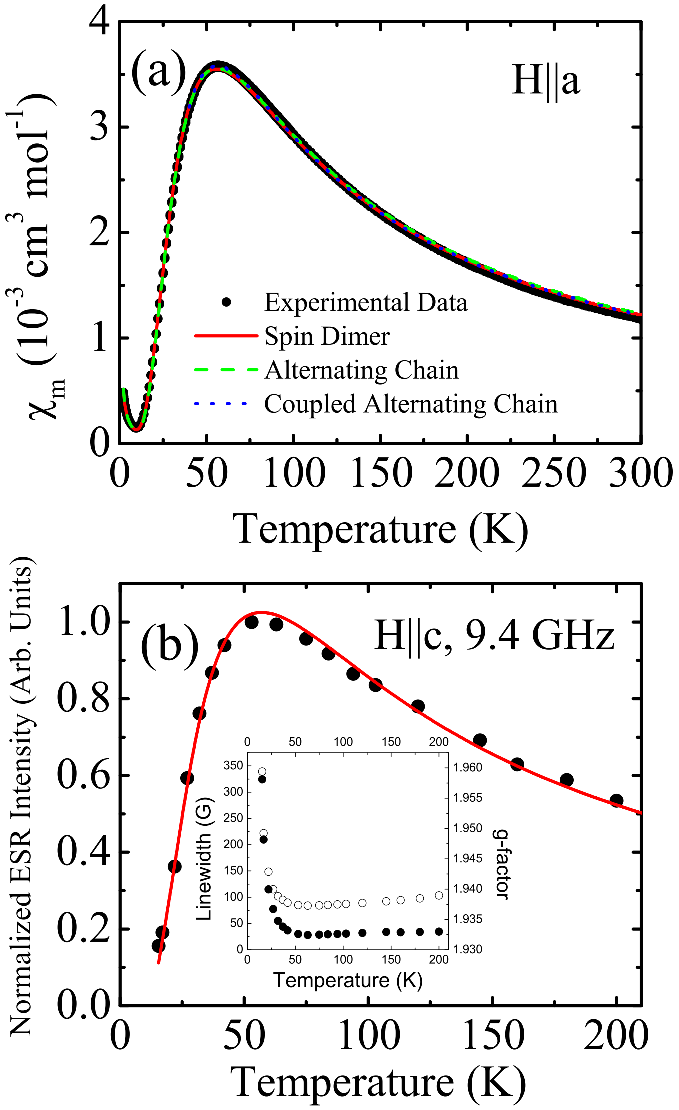

Figure 5.1: (a) Magnetic susceptibility χ for VOHPO$_4\cdot\frac{1}{2}$H$_2$O single crystals. Closed circles denote experimental data ($H \parallel a$), the solid (red) line shows the isolated dimer model fit, the dashed (green) line is the alternation chain model fit, and the dotted (blue) line shows the mean field-coupled alternating chain model fit. For these fits, we employed $g = 2.07$ ($H \parallel ab$ plane). (b) Normalized ESR intensity vs. temperature at 9.4 GHz. The fit (red solid line) is described in the text. The insets display the linewidth (open symbols) and g-factor (closed symbols) as a function of temperature. Our value of g (H $\parallel$ c) compares well with the previously reported 300 K value of 1.966, although there is no information on the direction of applied field in Ref. [51]. (after Ref. [41])

ternating chain [51,165,166] models can be fit to the susceptibility data (Fig. 5.1(a)), and with appropriate parameters, each accurately reproduces the experimental results. We extract J = 7.83 meV (63.15 cm^{-1}) for the dimer model, J = 7.80 meV (62.9 cm^{-1}) and α = J′/J = 0.04 for the alternating chain model, and J = 7.83 meV (63.15 cm^{-1}), $\alpha = 0.03$, and γ = J″/J = 0.005 for the mean field-coupled alternating chain model, respectively. In the latter, γ represents a mean field interchain interaction. Note that the small fitted J′/J and J″/J values show that the isolated dimer models gives a very good description of the susceptibility. As summarized in Table 5.1, the data can accommodate a small antiferromagnetic coupling between the dominant V-V magnetic dimers. Bulk susceptibility data can support modest antiferromagnetic coupling between the dominant magnetic dimer units. Similar antiferromagnetic coupling may be present along the *b* direction. However, as a macroscopic technique, susceptibility cannot easily distinguish between microscopically different models under weak coupling conditions. Energy dispersion data from inelastic neutron scattering experiments provide a comparable upper bound of <5% for the coupling between magnetic dimers. [167]

Figure 5.1(b) shows the ESR response of $\text{VOHPO}_4{\cdot}\frac{1}{2}\text{H}_2\text{O}$ between 5 and 200 K. A significant low-temperature linebroadening and shift of the resonance field, followed by a splitting of the absorption line into two weak resonances below 15 K, can be associated with a temperature-induced development of the spin-triplet exciton superstructure (see, for instance Ref. [170] and references therein). This will be investigated in future work. The integrated ESR intensity of $\text{VOHPO}_4{\cdot}\frac{1}{2}\text{H}_2\text{O}$ as a function of temperature exhibits behavior that is typical of a spin gap system and is consistent with expectations for a dimerized quantum $S = 1/2$ antiferromagnet with a singlet ground state. A detailed analysis of the ESR intensity dependence should include such parameters as the density of states and probability of ESR

Table 5.1: Exchange interactions of $VOHPO_4 \cdot \frac{1}{2}H_2O$ extracted from various experimental techniques

Technique	Sample Form	Model	J (meV)	α^b	γ^b	Δ_{gap} (meV)	References
χ	P	ID	7.6			7.6	[50, 51]
χ	SC $H \parallel a$	ID	7.83			7.83	This Work
	(or $H \parallel b$)	AC	7.80	0.04		7.61	This Work
		CAC	7.83	0.03	0.005		This Work
^{31}P NMR		ID	7.58			7.58	[51, 168, 169]
		AC	7.67	-0.427		5.52	[169]
		CDC	7.84	-0.429	-0.121		[169]
ESR	SC $H \parallel c$	ID	7.15			7.15	This Work
Neutron	DP	ID	7.81			7.81	[100]

[1] Technique: χ=Susceptibility.

[2] Sample Form: P=Powder; SC=Single Crystal; DP=Deuterated powder.

[3] Model: ID=Isolated Dimer; AC=Alteranting Chain; CAC=Coupled Alternating Chain; CDC=Coupled Dimer Chain.

[4] We estimate that the error bar on J is ±3% and ±10% for our susceptibility and ESR measurements, respectively.

[5] Here, α and γ are defined as J'/J and J''/J, respectively.

transition, which in $VOHPO_4 \cdot \frac{1}{2}H_2O$ can be affected by peculiarities of the local magnetic structure (including the interdimer coupling and/or the Dzyaloshinskii-Moriya interaction). Since no comprehensive theory is available, a simple isolated dimer model was used to fit the ESR data. A Boltzmann distribution is assumed for the temperature dependence of the ESR signal and in determining the spin singlet-triplet energy gap. The normalized integrated ESR absorption was fit as $I_{ESR}(T)/I_{max} \propto \{\exp[(-\Delta_{gap}+g\mu_B B)/k_B T]-\exp[(-\Delta_{gap}-g\mu_B B)/k_B T]\}/Z$, where g is the electron g-factor for our field configuration ($H \parallel c$), μ_B is the Bohr magneton, k_B is the Boltzmann constant, Z is the dimer partition function, and Δ_{gap} is the spin gap. The best fit to the data yields $\Delta_{gap} = 7.15$ meV (57.7 cm^{-1}), as shown in Table 5.1.

5.2 Low Energy Excitations in the Optical Spectrum of $VOHPO_4 \cdot \frac{1}{2}H_2O$

According to formal "change in dipole moment" selection rules, [171] magnetic excitations are absent from optical spectra due to the different parity of the singlet ground and triplet excited states. Symmetry breaking and various types of coupling can, however, allow these transitions through singlet-triplet mixing. One consequence of this mixing is the activation of low-energy magnetic excitations. Optical spectroscopy has been successfully employed in studies of the magnetic energy gaps in α'-NaV_2O_5, $SrCu_2(BO_3)_2$, and $CoCl_2 \cdot 2H_2O$, [172–176] multiple magnetic excitations in $CoCl_2 \cdot 2H_2O$ and $CsCoCl_3$, [175–177] and spin-vibron coupling and excitations of the magnetic manifold in Mn_{12}-acetate. [178–180] Thus, in fortuitous cases, magnetic excitations and interactions can be investigated with optical techniques. Many theoretical approaches have been employed to explain the electric-dipole activation of

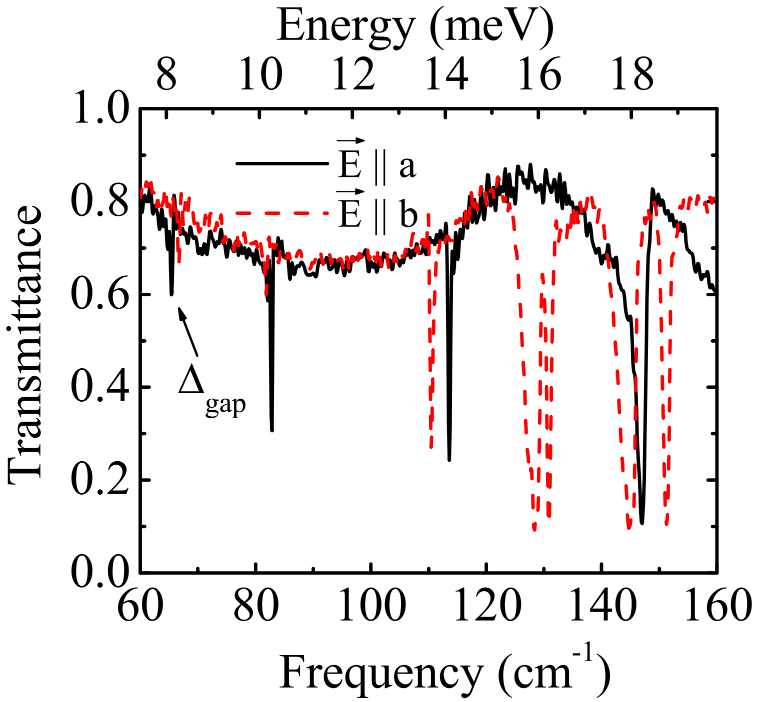

Figure 5.2: Far infrared transmittance spectra of $VOHPO_4{\cdot}\frac{1}{2}H_2O$ for light polarized along the a direction (black solid line) and b direction (red dashed line). The data were taken at 4.2 K. (after Ref. [41])

the singlet-triplet gap. [175,181–188] These approaches generally rely on higher-order terms in the Hamiltonian to lift selection rules.

Figure 5.2 displays the polarized transmittance spectrum of $VOHPO_4 \cdot \frac{1}{2} H_2O$ in the far infrared regime at 4.2 K. In order to assign each of the observed excitations, we consider the temperature dependence of each feature (Fig. 5.3) as well as previous neutron scattering results. [100] Magnetic excitations tend to be very sharp at base temperature and weaken rapidly with increasing temperature. In contrast, phonons are present at all temperatures (although they can broaden significantly), and oscillator strength sum rules must be obeyed. [29] Neutron scattering clearly identifies the spin gap at ∼7.81 meV (63.0 cm^{-1}). [100] An infrared absorption line appears in our data at a similar energy, with a notable polarization dependence: 8.11 meV (65.5 cm^{-1}) for $\vec{E}$ along a and 8.27 meV (66.7 cm^{-1}) for $\vec{E}$ along b. Based on the similar energies, the narrow linewidths (∼0.1 cm^{-1}), and the observed temperature dependence, we tentatively interpret the 8.11 and 8.27 meV lines as magnetic excitations, as related to the spin gap (Δ_{gap}). An alternate assignment is that this pair of peaks may be due phonons. If magnetic in origin, these excitations may be activated in the optical response and shifted from the unperturbed spin gap position by a dynamic Dzyaloshinskii-Moriya interaction, as described below. Based on the temperature dependence of the far infrared spectra shown in Fig. 5.3, we attribute the 15 - 20 meV peaks to lattice phonons. These lines are strongly polarized (Fig. 5.2). The origin of the 10.27/10.15 meV (82.83/81.87 cm^{-1}) peaks and the 13.7/14.1 meV (110.5/113.7 cm^{-1}) pair (Fig. 5.2) are still under investigation. We suspect that they may be related to zero field splittings [189] or multiple magnetic excitations, [176] although the latter is usually very weak. The low temperature linewidths are very narrow, on the order of 0.3 - 0.5 cm^{-1}, although they broaden significantly with increasing temperature.

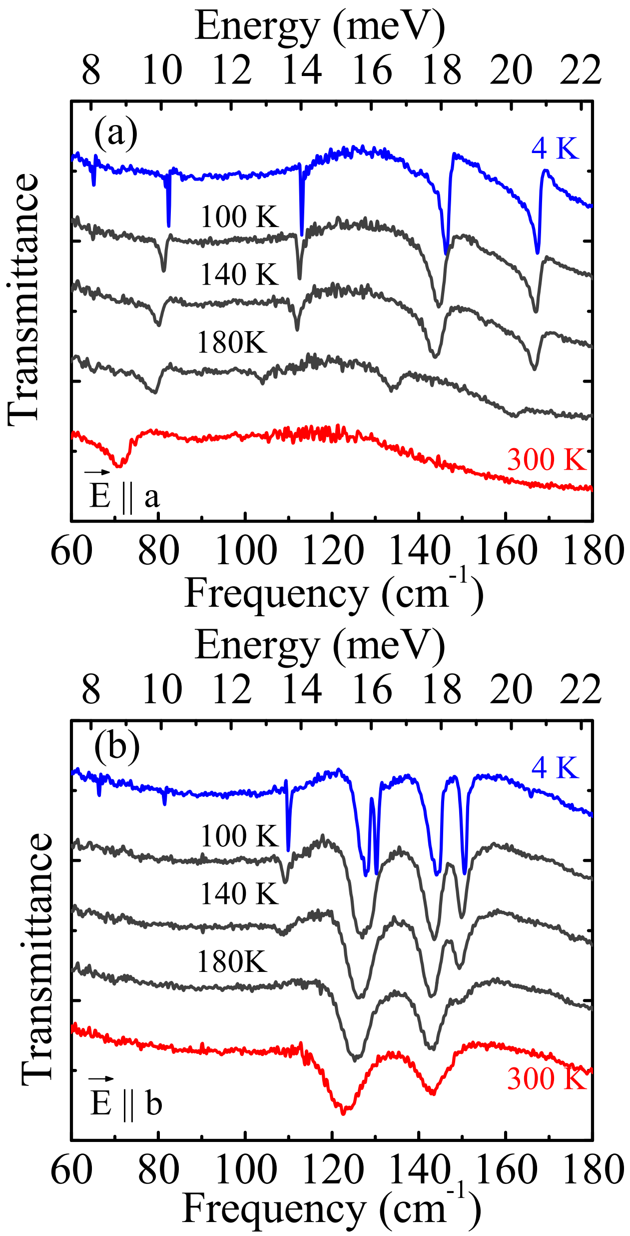

Figure 5.3: Variable temperature transmittance spectra of $VOHPO_4 \cdot \frac{1}{2}H_2O$ for light polarized (a) along the *a* direction and (b) along the *b* direction. Measurement temperatures are indicated. The spectra are offset by 0.45 for clarity. (after Ref. [41])

Table 5.1 summarizes the singlet-triplet gap energies of $VOHPO_4 \cdot \frac{1}{2}H_2O$, extracted from various measurements including magnetic susceptibility, ^{31}P NMR, ESR spectroscopy, and inelastic neutron scattering. In the isolated dimer model, Δ_{gap} is equal to the magnetic interaction energy J. In the alternating chain model, the relationship between Δ_{gap} and J is more complicated because the dominant dimers are coupled, resulting in mode dispersion, α so that $\Delta_{gap} = f(\alpha)$J. [190–192] In the coupled alternating chain model, $\Delta_{gap} = f(\alpha, \gamma)$J, although for weak coupling, the relationship will be similar to that for the isolated alternating chain. Here, α and γ are related to mode dispersion and defined as J′/J and J″/J, respectively. Interestingly, the position of Δ_{gap} determined by optical techniques (8.11 meV and 8.27 meV for a and b polarizations, respectively) is slightly higher than that obtained by other measurements. This result is likely a manifestation of spin-orbit coupling. Raman signatures of strong spin-phonon coupling have also been observed in $(VO)_2P_2O_7$. [193]

Assuming that these low-energy excitations (8.11 meV (65.5 cm^{-1}) for $\vec{E}$ along a and 8.27 meV (66.7 cm^{-1}) for $\vec{E}$ along b) are indeed magnetic in nature, the dynamic Dzyaloshinskii-Moriya interaction is one type of coupling that provides a plausible framework for understanding the observed spectroscopic results. The Dzyaloshinskii-Moriya interaction has also attracted attention in $BiFeO_3$ and in $Cu_2(OH)_3(C_mH_{2m+1}COO)$ (m = 7, 9, 11), in which it mediates magnetoelastic and glassy interactions, respectively. [194, 195] This interaction is created when an optically-active phonon breaks inversion symmetry through the dominant exchange pathway, therefore allowing an electric dipole singlet-to-triplet transition to occur between spin levels. [172–174, 181, 182, 186–188] The principal excitation of interest is $|S,0\rangle \rightarrow |T,0\rangle$, where S (T) denote singlet (triplet) spin states, and 0 denotes the phonon state. Similar transitions are observed at 8.11 meV (65.4 cm^{-1}) for

$\vec{E} \parallel a$ and 8.43 meV (68 cm^{-1}) for $\vec{E} \parallel c$ in α'-$\mathrm{NaV_2O_5}$ [172] and at 2.98 meV (24 cm^{-1}) in $\mathrm{SrCu_2(BO_3)_2}$. [174] The static interaction between the two spin states gives rise to magnetic dipole transitions. It does not require a lattice deformation. On the other hand, antisymmetric interaction requires at least an instantaneous lattice distortion and gives rise to electric dipole transitions between magnetic states. Both Cépas and Rõõm *et al.* estimate that the electric dipole excitations are much stronger than the magnetic dipole transitions. [172, 188] We therefore focus on dynamic Dzyaloshinskii-Moriya coupling. Using the analytical results obtained from first order perturbation theory (valid for low temperatures, modest Dzyaloshinskii-Moriya coupling, and phonon energies larger than the spin gap), [174, 188] we can write the transition probability for the electric dipole transition between magnetic states (I_{el}) as

$$I_{el} = |\langle T, 0|V|S, 0\rangle|^2 = \frac{I_{ph}(\mathbf{D}_{dDM})^2(\hbar\omega_p)^2}{[(\Delta_{gap})^2 - (\hbar\omega_p)^2]^2}, \tag{5.1}$$

where I_{ph} is the intensity or oscillator strength of the infrared-active phonon, D_{dDM} is the dynamic Dzyaloshinskii-Moriya coupling vector, $\hbar\omega_p$ is the phonon energy, and Δ_{gap} is the energy of excitation. Here, $\mathbf{D}_{dDM} = (\frac{\partial \mathbf{D}}{\partial Q}\big|_{Q=0})Q$, and $\mathbf{D}(0)$ is the static Dzyaloshinskii-Moriya vector. These terms give rise to the antisymmetric (electric dipole) and symmetric (magnetic dipole) excitations, respectively. Transition probability can thus be evaluated based on the spectroscopic data, allowing us to understand the possible activation of the singlet-triplet gap in the optical response of $\mathrm{VOHPO_4{\cdot}\frac{1}{2}H_2O}$. Previous estimates suggest that I_{el}:I_{ph} is on the order of 1:10000. [174, 188]

The rich phonon spectrum (Fig. 5.2) provides many low-energy a- and b-polarized lattice modes as candidates for possible coupling. As emphasized by Rõõm *et al.*, [172] the transition polarization is determined by the polarization of the optical phonon creating the dynamic Dzyaloshinskii-Moriya interaction by lattice deformation. To activate the 8.11 and 8.27 meV features in $VOHPO_4{\cdot}\frac{1}{2}H_2O$, at least two independent (a- and b-polarized) phonons are needed, and considering the complexity of the lattice dynamics, it is very likely that multiple modes are involved in each polarization. Separate a- and c-axis phonons were also essential for understanding the α'-NaV_2O_5 data. [172] By examining the ratio of intensities (which is proportional to the transition probabilities [172]), we can identify the phonons that may be contributing to the activation process. Further, we can see from Eqn. 5.1 that the energy of the coupling phonon should not be too far from the energy of the excitation. Based upon these criterion, the lattice modes between ~15 and 20 meV (120 - 160 cm^{-1}) in Fig. 5.2 are good candidates to activate the a- and b-polarized spin gap excitations. Dynamics simulations show that these modes modulate magnetic centers along the a- and b-directions, with low-energy out-of-plane, torsional, and twisting motion. For comparison, the important coupling phonons in α'-NaV_2O_5 are either at 199 or 518 cm^{-1} (a- direction) and at 68 cm^{-1} (c-direction), and those in $SrCu_2(BO_3)_2$ seem to involve Cu-O-Cu bond bending (perpendicular to the dimers). [172–174, 188] In contrast, a low-frequency lattice phonon (30 cm^{-1}) is implicated in $CoCl_2{\cdot}2H_2O$. [176]

The magnitude of the static Dzyaloshinskii-Moriya interaction can be estimated [182] as $D(0) \approx (|g - g_e|/g_e)J$. Using $g = 1.96$ and $g_e = 2.0$, we obtain $D(0) \approx 1.3$ cm^{-1} for $VOHPO_4{\cdot}\frac{1}{2}H_2O$. This relationship is often applied to describe the dynamic Dzyaloshinskii-Moriya interaction as well. An independent estimate of D_{dDM} can be extracted from Eqn. 5.1 using measured oscillator strengths for the spin gap excitations and coupling phonons. For $\vec{E} \parallel a$, $I_{el} \approx 65$ cm^{-2}, and $I_{ph} \approx 7060$ and 10550 cm^{-2} for the 146 and 167 cm^{-1} modes, respectively. For $\vec{E} \parallel b$, $I_{el} \approx 50$ cm^{-2}, and $I_{ph} \approx 9600$, 7625, and 3600 cm^{-2} for the 129, 146, and 167 cm^{-1} modes. Error bars on these values are fairly substantial, probably ±10%. These error bars are mainly arisen from determining the thickness of the sample. From the above analysis, we estimate $D_{dDM} = 7.9$ and 5.2 cm^{-1} (0.98 and 0.64 meV) along the *a* and *b* directions, respectively. A similar coupling strength was observed in α'-NaV$_2$O$_5$. [172] In the absence of magnetic field results, we are unable to determine the direction of the Dzyaloshinskii-Moriya vector, although it is certainly perpendicular to the activating phonon. Clearly, future high field investigations of gap mode splitting will be useful to confirm this overall picture.

5.3 Low Temperature Phase Transition and Enhanced Hydrogen Bonding

The two most interesting aspects of the variable temperature vibrational response of VOHPO$_4\cdot\frac{1}{2}$H$_2$O are the low-temperature mode splitting and redshifting. Figure 5.4 (a), (c), (e), and (g) displays close-up views of selected modes that illustrate the weak low temperature structural transition. Note that these vibrational features are at higher energy than those discussed previously (Fig. 5.2). It is well known that subtle atomic displacements, often difficult to detect in direct structural measurements, manifest themselves quite clearly in the infrared through the appearance of new phonon lines or splitting of existing features as a function of temperature. [196] The B$_{1u}$, B$_{2u}$, and B$_{3u}$ modes that derive from a group theoretical analysis of the 300 K P_{mmn} structure of VOHPO$_4\cdot\frac{1}{2}$H$_2$O are of A$_u$ and B$_u$ type in the lower symmetry $P2_1/c$ subgroup. [197]

The modes near 650, 940, 1100, and 1135 cm^{-1} are assigned as the out-of-plane P-O-H deformation, the symmetric P-O-H stretch, and the asymmetric PO$_3$ stretch (for the 1100 - 1205 cm^{-1} cluster), respectively. The features near 690 cm^{-1} are attributed to combined O-P-O and O-V-O deformation. The 4070 cm^{-1} mode is likely

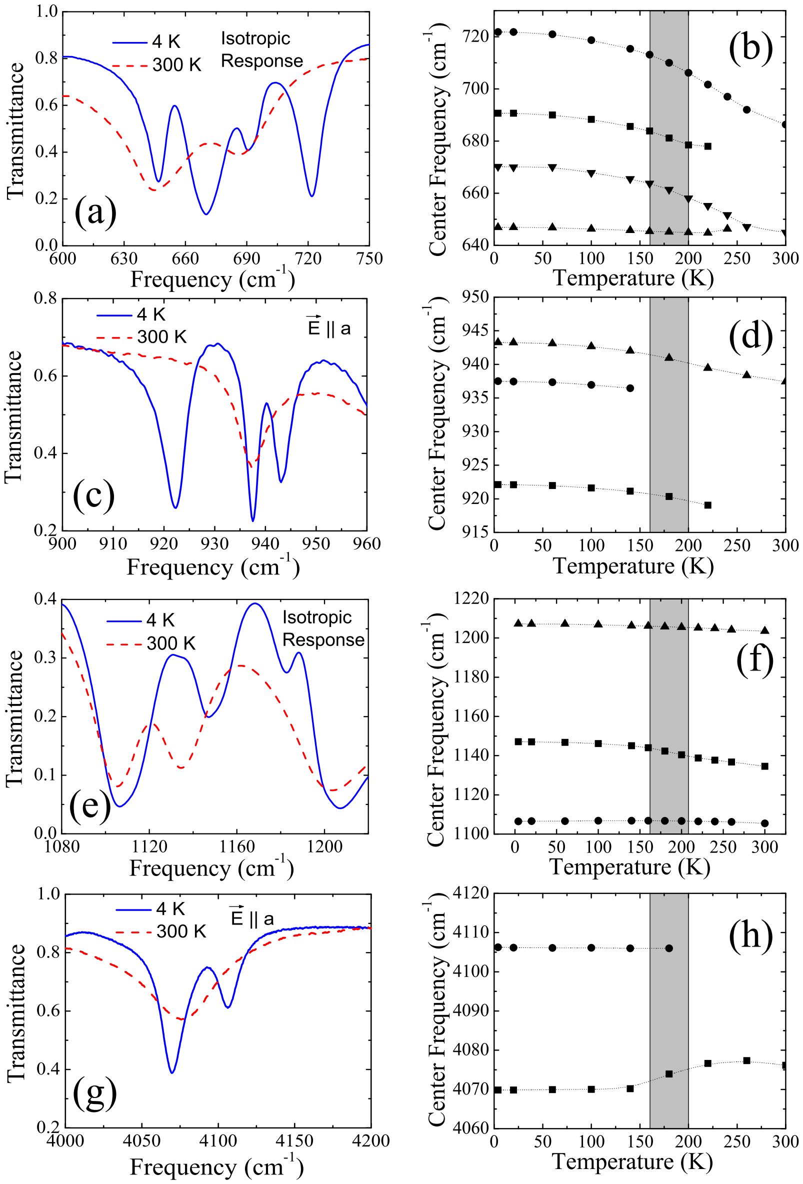

Figure 5.4: Close-up views of the temperature-dependent transmittance spectra (left) and corresponding mode frequencies (right) of VOHPO$_4\cdot\frac{1}{2}$H$_2$O in selected regions, highlighting the weak second order structural transitions near 180 K. Error bars are on the order of symbol size. (after Ref. [41])

a combination of the 1050 cm^{-1} (asymmetric PO_3 stretch) and 3050 cm^{-1} (P-OH stretching) features. [48, 198–200] The many spectral features above 3500 cm^{-1} are attributable to the hydrated waters and suggest that the PO_4 bridging anions are involved in the hydrogen bonding network. [48] In the PO_4 building block unit, the two short linkages (1.492 Å) involve P-O-V interactions, the intermediate bond length (1.545 Å) involves the P-O-$(V)_2$ interaction, and the long linkage (1.586 Å) is associated with different P-O-H interactions. Several of these modes split through the transition region. Using the 300 K mode near 940 cm^{-1} as an example, we observe the feature splits into triplets with decreasing temperature. A satellite peak arises from the shoulder near 922 cm^{-1} grows rapidly below 180 K. At the same time, a small peak at 937 cm^{-1} appears from 180 K. Changes in the 940 cm^{-1} P-O-H stretch (Fig. 5.4(c) and (d)), suggest that the local symmetry of this group is broken into at least three distinct arrangements at low temperature. The 650 cm^{-1} out-of-plane P-O-H deformation mode (Fig. 5.4(a) and (b)) splits as well. At the same time, trends in the asymmetric PO_3 stretching mode (Fig. 5.4(e) and (f)) are standard (no low temperature splitting or red-shifting), suggesting that that interactions are modified mainly between the apical oxygen in the PO_4 tetrahedra and the hydrogen atoms on the shared waters. The gradual distortion of the P-O-H group with decreasing temperature is important because subtle distortions and displacements of the bridging PO_4 anions certainly influence magnetic exchange within and between dominant spin dimers. [99] To quantify these vibrational changes, peak centers were plotted as a function of temperature (Fig. 5.4 (b), (d), (f), and (h)). Based upon these results, we identify a weak second-order structural phase transition centered at $\sim$180 K. This gradual transition has no signature in the magnetic susceptibility. As discussed below, this transition is driven by a low-temperature change in hydrogen bonding.

Figure 5.5 shows the low temperature redshift of selected vibrational modes, each of which is intimately connected to the complex hydrogen bonding network in $VOHPO_4 \cdot \frac{1}{2}H_2O$. Here, the 978 and 1956 cm^{-1} features correspond to the vanadyl stretching mode of the distorted VO_6 octahedra and its overtone, with 10 and 20 cm^{-1} redshifts, respectively. The broad H_2O combination mode (1640 cm^{-1} deformation + 3370 cm^{-1} stretching) near 5000 cm^{-1} displays a 23 cm^{-1} redshift between 300 and 4 K. This mode softening occurs through the 180 K transition range, suggesting that a change in hydrogen bonding drives the low-temperature structural phase transition.

The resonance frequency of a vibrational mode goes as $\omega \sim (k/\mu)^{1/2}$, where k is the force constant of the bond and μ is the effective mass of the atoms involved in the vibration. With decreasing temperature, atom-atom and unit cell distances generally contract, thus increasing the size of k. As a result, mode resonance frequencies usually increase with decreasing temperature, an effect that is traditionally called "mode hardening". Here, selected modes display opposite trend with temperature. Although unusual, mode softening has been observed in other magnetic materials. [201–204] $Cu(Pz)(NO_3)_2$ and $Cu(Pz)_2(ClO_4)_2$ are two examples. The overall extent and magnitude of mode softening in $VOHPO_4 \cdot \frac{1}{2}H_2O$ is similar to that in quasi-one-dimensional $Cu(Pz)(NO_3)_2$. In this case, mode softening is attributed to an enhanced electrostatic attraction between pyrazine hydrogens and nitrate oxygens at low temperatures. [203] As the lattice contracts, the distance between oxygens and hydrogens decreases, causing a stronger attractive interaction. Such a competing interaction against the thermal contraction gives rise to an increase in certain bond lengths at low temperature and thus results in the softening of selected vibrational modes. [203] The mode softening in $Cu(Pz)_2(ClO_4)_2$ originates from a similar mechanism, but due to the layered structure, fewer modes in this compound soften. [204] Based upon the presence of complex hydrogen bonding

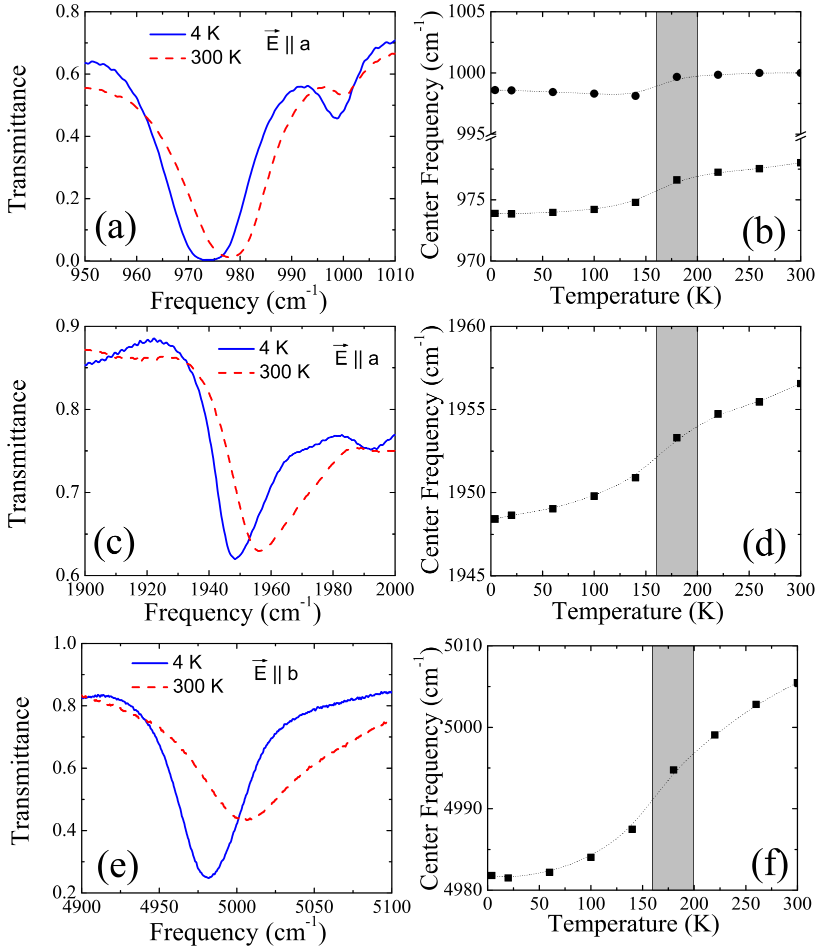

Figure 5.5: Close-up views of the temperature-dependent transmittance spectra (left) and corresponding mode frequencies (right) of $VOHPO_4{\cdot}\frac{1}{2}H_2O$ in selected regions, highlighting the weak transition of the low temperature mode softening transition near 180 K. Error bars are on the order of symbol size. (after Ref. [41])

networks in $VOHPO_4{\cdot}\frac{1}{2}H_2O$ [49,109] and the variable temperature dynamics data in Fig. 5.5, we attribute the observed low-temperature mode softening to a change in hydrogen bonding interactions in this system. Structural studies show that several oxygen and hydrogen positions become ordered at low temperature, [49] a process that affects both vanadyl and hydrogen-oxygen bond lengths. Softening of the V=O stretching modes and H_2O-related vibrational modes demonstrates that these interactions weaken through the transition. In terms of magnetostructural correlations, relaxation of local VO_6 structure will influence magnetic overlap. [99] Note that hydrogen bonding also plays an important role in the topotactic transformation of $VOHPO_4{\cdot}\frac{1}{2}H_2O$ to $(VO)_2P_2O_7$. [109] Hydrogen bonding has been shown to mediate exchange coupling in the quasi-two-dimensional S=1/2 Heisenberg antiferromagnet $Cu(H_2O)_2(C_2H_8N_2)SO_4$ (and many other materials) as well. [205–208]

5.4 Color Properties of $VOHPO_4{\cdot}\frac{1}{2}H_2O$

Figure 5.6 displays the polarized absorption spectra of $VOHPO_4{\cdot}\frac{1}{2}H_2O$ at 10 K. The spectra exhibit a complex color band centered at ∼1.5 eV and a strongly anisotropic absorption edge above 3.1 eV. Based on our electronic structure calculations and comparison with chemically similar model compounds, [37, 38, 144, 209] the 1.5 eV absorption bands are attributed to V^{4+} $d \rightarrow d$ on-site excitations. Significant *p*-*d* covalent mixing is the origin of the strong optical activity. The observed splitting indicates that the 3*d* levels are nondegenerate. In particular, the results demonstrate that $d_{3z^2-r^2}$ is appropriately clustered with the rest of the *d*-levels, different than suggested in previous theoretical work. [48] As shown in the inset, the color band changes subtly with temperature. The features above the 3.1 eV charge transfer gap are assigned as O 2*p* → V 3*d* charge transfer excitations. The shoulder on the leading edge of the absorption band at ∼3.5 eV is a result of the complex joint density of

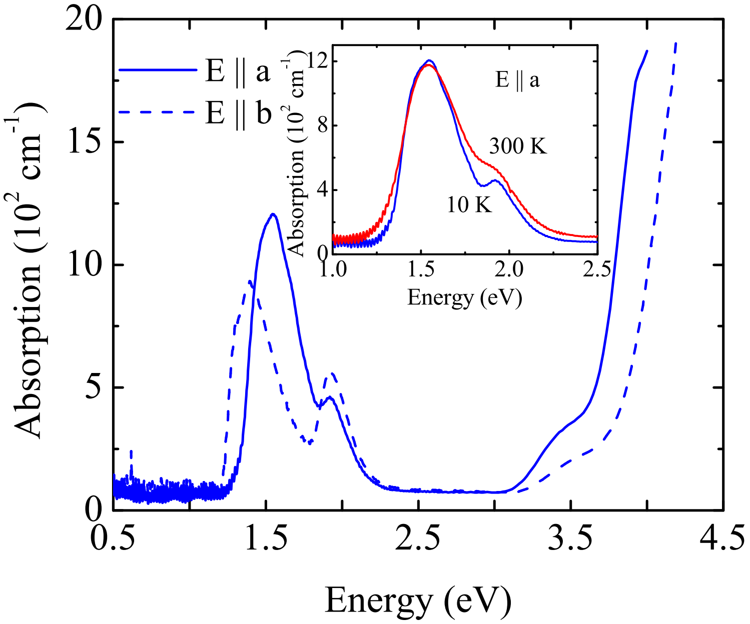

Figure 5.6: 10 K absorption spectra of $VOHPO_4 \cdot \frac{1}{2}H_2O$ for light polarized along the *a* and *b* directions. The inset shows a close-up of view of the color band for light polarized along *a* at 10 and 300 K, respectively. This color band gives $VOHPO_4 \cdot \frac{1}{2}H_2O$ crystals their characteristic appearance. (after Ref. [42])

Table 5.2: Center position (in eV) of model oscillator fits to the color band in $VOHPO_4\cdot\frac{1}{2}H_2O$

Polarization	Temperature (K)	1	2	3	4
E‖a	300	1.305	1.401	1.501	1.740
	10	1.285	1.378	1.506	1.749
E‖b	300	1.180	1.279	1.390	1.750
	10	1.159	1.240	1.357	1.749

states in this compound.

Transition metal *d* to *d* on-site excitations are well-known to be sensitive indicators of the local crystal field environment. As already mentioned, the low temperature crystal structure of $VOHPO_4\cdot\frac{1}{2}H_2O$ contains two independent, low-symmetry vanadium sites per unit cell. Note that the vanadyl bond is very short. Due to the C_s site symmetry at the vanadium center and the strongly distorted VO_6 octahedron, the 3*d* energy levels of the transition metal ion are predicted to be non-degenerate, in agreement with the measured optical properties (Fig. 5.6).

The influence of hydrogen bonding on the electronic structure is of particular interest. In order to asses these trends, we fit the variable temperature absorption spectra (both E‖*a* and E‖*b*) in the color band regime with four model Voigt oscillators. The results are summarized in Table 5.2. Six out of eight excitations display unusual changes, redshifting with decreasing temperature. Redshifted excitations are characteristic indicators of enhanced hydrogen bonding in complex materials. [210–212] As discussed previously, $VOHPO_4\cdot\frac{1}{2}H_2O$ is known to present two types of interlayer hydrogen bonding interactions: (i) hydrogens on shared water molecules can interact with apical oxygen atoms that are bonded to phosphate tetrahedra in a neighboring layer, and (ii) covalently bound hydrogen centers can interact with vanadyl oxygen atoms in an adjacent layer. Examination of the crystal structure indicates that the second type of hydrogen bonding directly influences the local VO_6 crystal field environment. Secondary support for this assignment comes from vibrational property measurements (Fig. 5.5(a-d)). Here, both the fundamental V=O stretching mode ($\sim$980 cm^{-1})and its overtone ($\sim$1960 cm^{-1}) soften through 180 K, providing direct evidence of a weak structural transition driven by enhanced low temperature hydrogen bonding. The data of Table 5.2 demonstrate that the electronic structure is sensitive to subtle changes in the hydrogen bonding pattern as well. First principle electronic structure calculations are in progress to complement this experimental work.

Chapter 6

Infrared and Optical Studies of $(La_{0.4}Pr_{0.6})_{1.2}Sr_{1.8}Mn_2O_7$

6.1 Field Dependence of the Optical Spectra

Figure 6.1(a) displays the *ab* plane optical conductivity of $(La_{0.4}Pr_{0.6})_{1.2}Sr_{1.8}Mn_2O_7$ in the low (spin-glass insulator) and high field (ferromagnetic metal) states at 4.2 K. The dominant effect of the applied field is to redshift the oscillator strength, which is conserved within a few percent. A similar field-induced redshift of the spectral weight has been observed in other manganites. [213–216] In $(La_{0.4}Pr_{0.6})_{1.2}Sr_{1.8}Mn_2O_7$, the electronic excitation near 1 eV in the spin-glass insulator state arises from a combination of Mn^{3+} intra-atomic *d* to *d* excitations superimposed with Mn^{3+} to Mn^{4+} (*d* to *d*) inter-atomic charge transfer excitations. [119, 217, 218] This feature narrows and shifts to 0.4 eV in the high field ferromagnetic metal state. With increasing magnetic field, spectral weight also transfers to the lower energy region, enlarging the bound carrier excitation in the far infrared. This feature is a signature of ferromagnetic domain formation [119] and is discussed in more detail below. Note that the optical conductivity of $(La_{0.4}Pr_{0.6})_{1.2}Sr_{1.8}Mn_2O_7$ does not show typical metallic

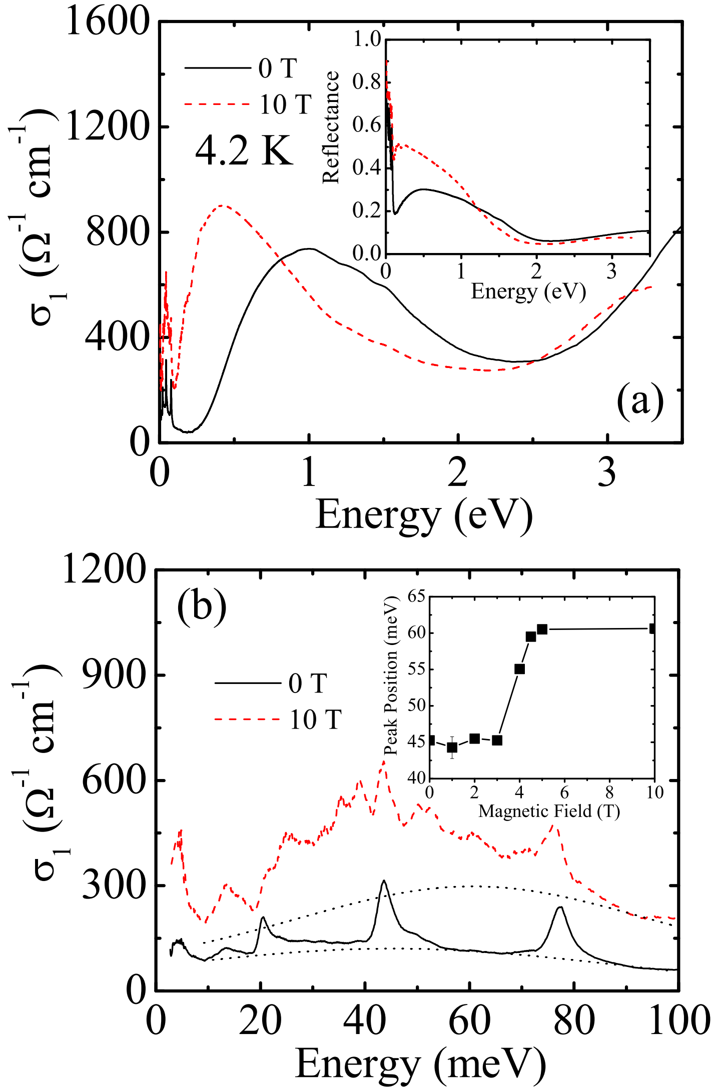

Figure 6.1: (a) Optical conductivity of $(La_{0.4}Pr_{0.6})_{1.2}Sr_{1.8}Mn_2O_7$ within the *ab* plane under 0 (solid line) and 10 T (dashed line) at 4.2 K ($H \parallel c$), extracted from a Kramers-Kronig analysis of the measured reflectance data (inset). (b) Close-up view of the 4.2 K optical conductivity within the *ab* plane under 0 and 10 T magnetic fields ($H \parallel c$). Dotted lines guide the eye to highlight the broad underlying bound carrier localization. The inset shows the development of the bound carrier localization (dotted lines), associated with ferromagnetic domains, upon application of field. (after Ref. [43])

behavior under any circumstances. Even at 10 T, where the system is driven into the ferromagnetic metal state, a far-infrared bound carrier excitation is observed rather than a Drude response. Manganites generally display low dc conductivities, [4, 6, 7] and $(La_{0.4}Pr_{0.6})_{1.2}Sr_{1.8}Mn_2O_7$ is no exception. Transport measurements show that σ_{dc} is $\sim 10^{-5}\ \Omega^{-1}\ cm^{-1}$ in the low temperature insulating state and $\sim 250\ \Omega^{-1}\ cm^{-1}$ in the high field metallic state, [123] in reasonable accord with our optical properties data.

Figure 6.1(b) displays a close-up view of the 4.2 K optical conductivity within the *ab* plane in zero (spin-glass insulator) and high magnetic fields (ferromagnetic metal). Interestingly, the bound carrier excitation is stabilized in the high field state, moving from ∼40 to 60 meV with a substantial increase in oscillator strength. To quantify changes in localization with applied magnetic field, we fit the spectra with several model oscillators over this energy range. Both peak position (inset, Fig. 6.1(b)) and spectral weight show a first-order transition near 4 T, demonstrating that the ferromagnetic domains, which are associated with the bound carrier localization, couple to the field-induced transition. We previously conjectured that the presence of this low-energy bound carrier excitation in $(La_{0.4}Pr_{0.6})_{1.2}Sr_{1.8}Mn_2O_7$ may be connected with the improved magnetoresistance properties. [119] Evidence for domains in the ferromagnetic metal state also comes from recent resistive relaxation studies. [125] Optical imaging techniques provide direct evidence for texture changes with applied magnetic field as well. [121]

In order to gain additional insight into the influence of disorder, it is useful to compare the low-energy dynamics in the field-induced ferromagnetic metal state of $(La_{0.4}Pr_{0.6})_{1.2}Sr_{1.8}Mn_2O_7$ with the temperature-induced ferromagnetic metal state of the double-layer parent compound $La_{1.2}Sr_{1.8}Mn_2O_7$. The latter is obtained from the literature data of Lee *et al.*. [218] It is worthy noticing that neither material is a conventional metal (Fig. 6.2). The optical conductivity of $La_{1.2}Sr_{1.8}Mn_2O_7$ is characteristic of a weak metal, with a small polaron hopping band (Mn^{3+} to Mn^{4+} charge transfer) overlapping the onsite Mn d to d transitions. [218] The high-temperature ~0.15 - 0.3 eV pseudogap in the optical conductivity is attributed to short-range charge/orbital ordering. [218] From a theoretical point of view, pseudogap formation is predicted to be a generic consequence of mixed-phase regimes. [219] This gap begins to fill below T_c and disappears in the low temperature ferromagnetic metal state. [218] The response of the Pr-substituted material is similar, but the far-infrared bound carrier excitation is separated from the asymmetric set of electronic excitations centered at 0.4 eV by a smaller pseudogap near 100 meV. The oscillator strength lost due to pseudogap formation is recovered in the bound carrier peak at 60 meV (Fig. 6.2). We conclude that, although the low temperature state of $La_{1.2}Sr_{1.8}Mn_2O_7$ and the high field state of the Pr-substituted material are both considered to be ferromagnetic metals from the bulk properties point of view, [123, 218] their low-energy electronic response is different. In ARPES, k-space sampling is different and the pseudogap energy scale is more difficult to define because the gap is "soft". Even so, in the high temperature phase, the size of the pseudogap is generally consistent with optical results in $La_{1.2}Sr_{1.8}Mn_2O_7$ and related double layer manganites. [218,220,221] Interestingly, ARPES shows that the pseudogap persists into the low-temperature phase of $La_{1.2}Sr_{1.8}Mn_2O_7$, with an extrapolated value of ~90 meV. [222] This differs from the optical property results for the parent compound below T_c, [218] but is in line with the 100 meV pseudogap in $(La_{0.4}Pr_{0.6})_{1.2}Sr_{1.8}Mn_2O_7$ (Fig. 6.2). Disorder effects in the Pr-substituted material likely break k-space selection rules and change the optical activity of this excitation.

Direct information on how phonons couple with the magnetically driven transition in $(La_{0.4}Pr_{0.6})_{1.2}Sr_{1.8}Mn_2O_7$ is also of interest, especially since stretching modes

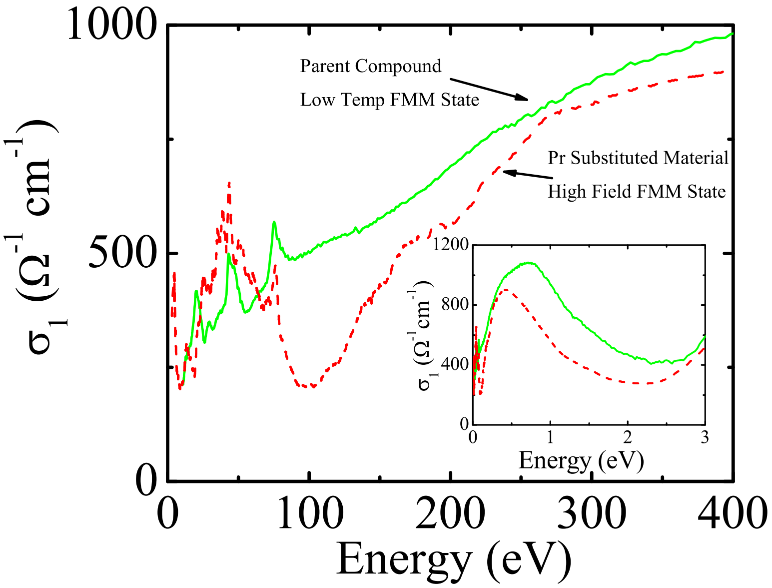

Figure 6.2: *ab* plane optical conductivity of the low temperature (10 K, 0 T) ferromagnetic metal state of $La_{1.2}Sr_{1.8}Mn_2O_7$ and the high field (4.2 K, 10T, $H \parallel c$) ferromagnetic metal state of $(La_{0.4}Pr_{0.6})_{1.2}Sr_{1.8}Mn_2O_7$. The spectrum of the parent compound $La_{1.2}Sr_{1.8}Mn_2O_7$ is from Ref. [218]. (after Ref. [43])

have been implicated in electronic kink formation in recent photoemission studies of a double-layer manganite, [220] and correlation between the Mn-O stretching mode and polaron formation was demonstrated by optics in $La_{1.2}Sr_{1.8}Mn_2O_7$. [218] In addition to the well-known infrared-active modes of the double-layer compounds, [218] the vibrational spectrum of $(La_{0.4}Pr_{0.6})_{1.2}Sr_{1.8}Mn_2O_7$ exhibits a number of new, small modes in the low-field insulating state that are likely derived from the symmetry breaking effects of Pr substitution. [119, 223] Some of these smaller structures become quite prominent in the ferromagnetic metal state, riding on top of the far-infrared bound carrier excitation (Fig. 6.1(b)). Several modes shift with applied field, indicative of a significant structural change between the low-field insulating to high-field metallic phases.

Figure 6.3(a) displays trends in the field-dependent Mn-O stretching and bending modes. Upon increasing field, the 77.4 meV Mn-O stretching mode softens on approaching to the transition, shows a sharp change through H_c, and saturates above 5 T. The 46.3 meV O-Mn-O bending mode is more complicated. It hardens on approaching the transition and then drops suddenly across H_c. Several other modes soften through the spin-glass insulator - ferromagnetic metal transition as well, indicative of a structural change. For comparison, Fig. 6.3(b) displays the temperature dependent trends of the Mn-O stretching mode in both $(La_{0.4}Pr_{0.6})_{1.2}Sr_{1.8}Mn_2O_7$ and $La_{1.2}Sr_{1.8}Mn_2O_7$. [218] Note that the Mn-O stretching mode softens through T_c in the parent compound, [218] whereas it softens through H_c in the Pr-substituted material. We can also compare field-induced modifications in the Mn-O stretching and bending modes with neutron diffraction and magnetostriction results. [122, 224] Neutron diffraction data shows that several bond lengths change with field. For instance, the distance between Mn and O (equatorial bond) is 1.931(8) Å in the spin-glass insulator state and increases to 1.937(2) Å in the ferromagnetic metal

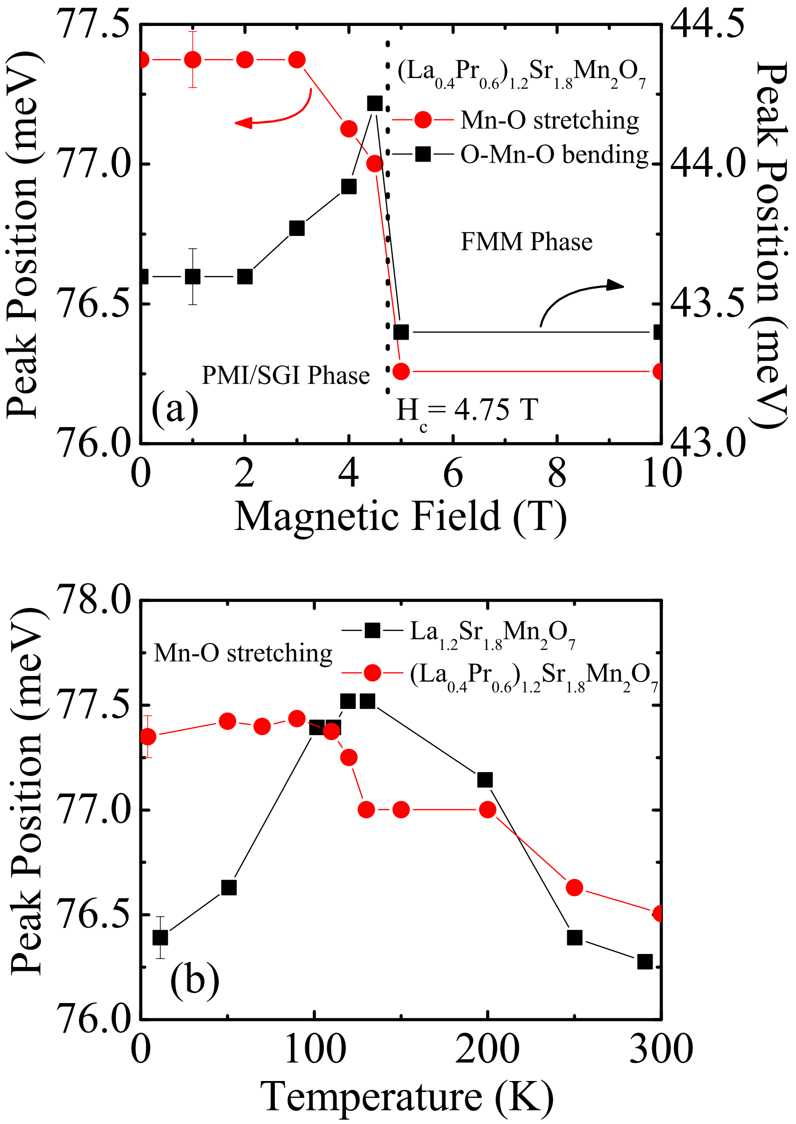

Figure 6.3: (a) Magnetic field dependent Mn-O stretching and bending modes of $(La_{0.4}Pr_{0.6})_{1.2}Sr_{1.8}Mn_2O_7$. (b) Temperature-dependence of the Mn-O stretching modes of $(La_{0.4}Pr_{0.6})_{1.2}Sr_{1.8}Mn_2O_7$ and $La_{1.2}Sr_{1.8}Mn_2O_7$, the double-layer parent compound (T_c=120 K). Data for $La_{1.2}Sr_{1.8}Mn_2O_7$ are from Lee *et al.* in Ref. [218]. (after Ref. [43])

state. [118,122] This trend is consistent with our observation of softer phonon modes in the high field ferromagnetic metal state of $(La_{0.4}Pr_{0.6})_{1.2}Sr_{1.8}Mn_2O_7$ (Fig. 6.3(a)). On the other hand, magnetostriction is a bulk technique. The elastic constants of $(La_{0.4}Pr_{0.6})_{1.2}Sr_{1.8}Mn_2O_7$ soften through the transition and then tighten with applied field as Mn-O bond length disorder is suppressed. [224]

Tomioka and Tokura recently proposed a global phase diagram of perovskite manganites within the plane of effective one-electron bandwidth and quenched disorder. [8] These two parameters are controlled by the average value and the variance of rare earth and alkaline earth ionic radii, respectively. With increasing quenched disorder, the Y-shaped bicritical feature of the phase diagram splits and a spin-glass insulator state emerges, separating the ferromagnetic metal and charge/orbital ordered antiferromagnetic phases. The authors propose that spin-glass character may enhance the colossal magnetoresistance effect in these materials. [8] Reviewing complexity in strongly correlated electronic systems, Dagotto emphasizes that this glassy region is dominated by short-range correlations and a local tendency towards either ferromagnetic metal or antiferromagnetic insulator regimes. [228, 229]

Although the Tomioka-Tokura phase diagram was developed for cubic perovskites, [8] the underlying physics may be useful for understanding the double-layer manganites as well. We therefore investigated trends in $(La_{1-z}Pr_z)_{1.2}Sr_{1.8}Mn_2O_7$ within the general framework of this global electronic phase diagram picture, modified to account for the two distinct perovskite (P) and rock salt (R) sites in the double-layer material. Table 6.1 shows calculated values of the averaged radii (r_A) and the variance of the ionic radii (σ^2) with different Pr substitution. Both P and R sites show the same trend: r_A decreases and σ^2 increases with Pr substitution. Can we understand bulk property trends in $(La_{0.4}Pr_{0.6})_{1.2}Sr_{1.8}Mn_2O_7$ within this picture? Table 6.1 shows the correlation between the paramagnetic insulator to ferromagnetic metal

Table 6.1: The averaged radii r_A and variance of the ionic radii σ^2 of $(La_{1-z}Pr_z)_{1.2}Sr_{1.8}Mn_2O_7$, calculated at the perovskite (P) and rock salt (R) sites

		P Sites		R Sites	
z	T_c (K)	r_A (Å)	σ^2 (Å^2)	r_A (Å)	σ^2 (Å^2)
0	120	1.408	0.00154	1.272	0.00212
0.2	90	1.403	0.00226	1.269	0.00256
0.4	60	1.398	0.00294	1.266	0.00297
0.6	-	1.394	0.00358	1.264	0.00337

[1] The averaged radii r_A and the variance of the radii σ^2 are calculated as $r_A = \sum x_i r_i$ and $\sigma^2 = \sum x_i(r_i^2 - r_A^2)$, where x_i and r_i are the fractional occupancies ($\sum x_i = 1$) and effective ionic radii of rare earth and alkaline earth cations, respectively. [8, 225]

[2] Standard ionic radii are obtained from Refs. [226, 227]. The P site has a coordination number of 12, and the R site has a coordination number of 9.

transition temperature (T_c), [55, 117] electronic bandwidth, and quenched disorder. With increasing Pr substitution, T_c decreases and is eventually quenched. [55, 117] Despite the suppression of T_c at z=0.6, $(La_{0.4}Pr_{0.6})_{1.2}Sr_{1.8}Mn_2O_7$ is still in close proximity to the ferromagnetic metal phase boundary. Thus, a small local structure variation can modify r_A and σ^2, pushing the system back into the ferromagnetic metal state. The measured phonon softening through the H_c (Fig. 6.3(a)) demonstrates that local Mn-O bonding is more relaxed in the high field ferromagnetic metal state, in line with observations by Lee *et al.* of a relaxed lattice in the double-layer parent compound at low temperature. [218] It is therefore probable that the applied field modifies r_A and overcomes substitution-induced disorder effects in σ^2, driving the system back into the ferromagnetic metal state in the Tomioka-Tokura phase diagram. The principal difference between the field-induced ferromagnetic metal state in $(La_{0.4}Pr_{0.6})_{1.2}Sr_{1.8}Mn_2O_7$ and the temperature-induced ferromagnetic metal state in $La_{1.2}Sr_{1.8}Mn_2O_7$ is the presence of the pseudogap in the substituted material (Fig. 6.2). The anticipated curvature of the spin-glass insulator/ferromagnetic metal phase boundary in magnetic field is consistent with this picture and facilitates the magnetically-driven transition. At the same time, the low energy scale of H_c indicates the closely competing nature of the spin-glass insulator and ferromagnetic metal phases in the Pr-substituted double-layer manganite. These results suggest that control of disorder in the proximity of a phase boundary may provide an important route to magnetodielectric materials that are switchable in low magnetic fields.

6.2 Optical Phase Diagram

Our comprehensive magneto-optical measurements allow us to generate the $H-T$ phase diagram of $(La_{0.4}Pr_{0.6})_{1.2}Sr_{1.8}Mn_2O_7$ for $H \parallel c$ (Fig. 6.4). Here, we measured the magneto-optical response of $(La_{0.4}Pr_{0.6})_{1.2}Sr_{1.8}Mn_2O_7$ as a function of temperature and field, and quantified the changes by plotting the absolute value of the integrated intensities of the field-induced feature. The first derivative of this change determined the boundary from the optical perspective. For comparison, we also plotted several points determined from selected resistivity, magnetization, and magnetostriction measurements. [120,123,224] Magnetization measurements indicate two boundaries at ∼2 and 5 T below 50 K, perhaps due to domain rotation. [224] Above 50 K, relaxation effects are more rapid. [123] Here, the phase diagram from both optics (which measures the microscopic nature of the charge degrees of freedom) and magnetization are in good agreement, although the boundary becomes more diffuse with increasing temperature (inset, Fig. 6.4(a)).

It is especially interesting to compare the correspondence of the low temperature phase boundaries in $(La_{0.4}Pr_{0.6})_{1.2}Sr_{1.8}Mn_2O_7$, determined by different techniques. Recently, Matsukawa *et al.* used combined resistivity, magnetization, and magnetostriction measurements to show that the bulk relaxation time of the lattice is two orders of magnitude smaller than that of the resistivity. [125] Extending this analysis

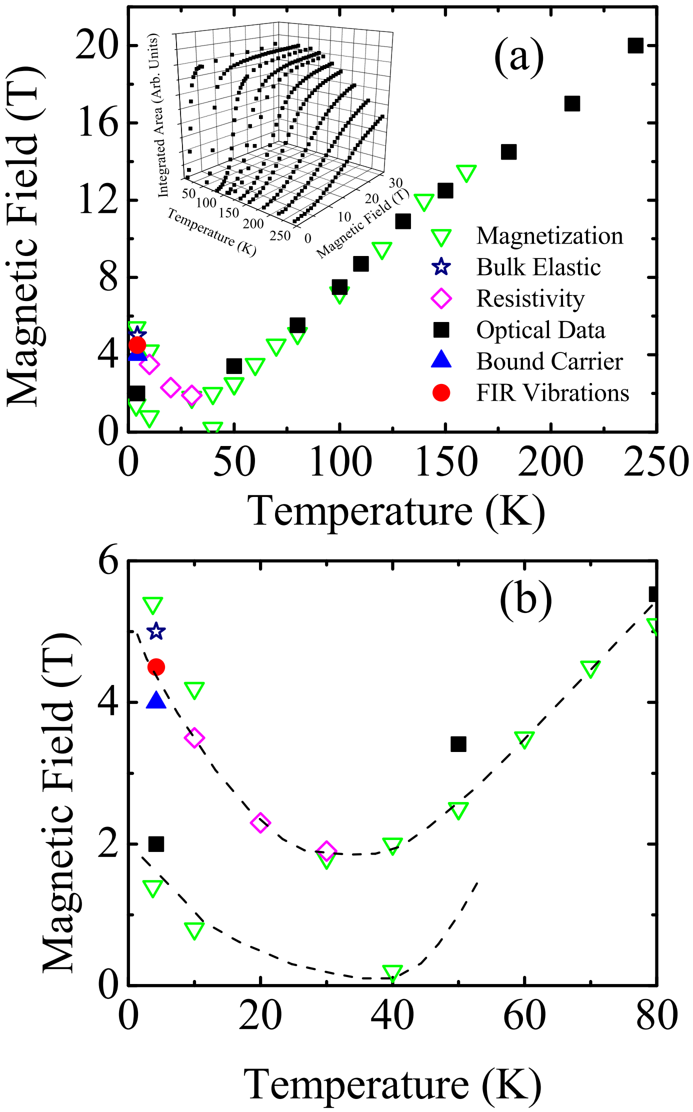

Figure 6.4: (a) $H-T$ phase diagram, extracted from the optical properties data for $H \parallel c$. Data are taken with increasing field. Selected magnetization, magnetostriction, and resistivity results are shown for comparison. [120, 123, 224] The inset displays the absolute value of the integrated area of the reflectance ratio spectra in the color band region as a function of temperature and magnetic field. Inflection points in the data were used to determine phase boundary locations. (b) Close-up of view of the $H-T$ phase diagram in the low temperature region. (after Ref. [43])

to include microscopic trends, we find that the critical field extracted from field-induced changes in Mn^{3+} e_g orbital population is similar to the first magnetization boundary (∼2 T). On the other hand, direct measurements of Mn-O and O-Mn-O stretching and bending vibrational modes (Fig. 6.3(a)) show excellent correspondence with critical fields determined from bulk magnetostriction, resistivity, and the second magnetization boundary (∼5 T). Changes in the far-infrared bound carrier excitation (inset, (Fig. 6.1(b)) are also associated with this lattice distortion. The results demonstrate that the lattice responds more slowly than charge and spin over various length and time scales. The strong hysteresis in the low temperature physical properties [55, 120, 123, 125, 224, 230] of $(\mathrm{La}_{0.4}\mathrm{Pr}_{0.6})_{1.2}\mathrm{Sr}_{1.8}\mathrm{Mn}_2\mathrm{O}_7$ derives from these differences.

6.3 Field-Induced Color Changes at 300 K and Visualization

Controlled disorder near a phase boundary can clearly yield a substantial magnetodielectric response over a wide energy range. However, at this time, most magnetodielectric materials [37, 131, 134, 159, 213, 214, 230–234] display contrast only at low temperatures. Strategic control of spin-lattice interactions or the presence of a magnetically-driven phase transition (and associated change in ground state) offer potential routes to higher transition temperatures. The latter is investigated here. Specifically, we explored whether the remnants of the spin-glass insulator to ferromagnetic metal transition in $(\mathrm{La}_{0.4}\mathrm{Pr}_{0.6})_{1.2}\mathrm{Sr}_{1.8}\mathrm{Mn}_2\mathrm{O}_7$ can be used to drive color property changes at room temperature.

Figure 6.5 displays the 300 K optical conductivity of $(\mathrm{La}_{0.4}\mathrm{Pr}_{0.6})_{1.2}\mathrm{Sr}_{1.8}\mathrm{Mn}_2\mathrm{O}_7$ at 0 and 30 T. The field-induced spectral changes are similar to but smaller than

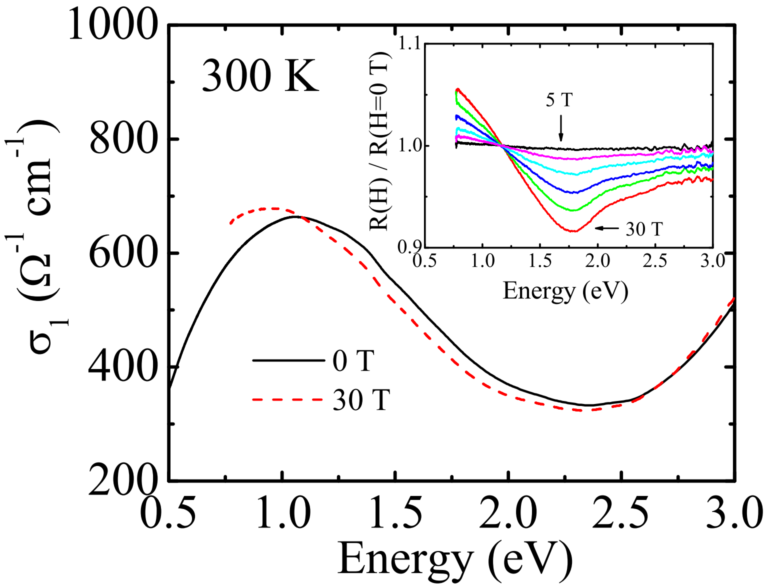

Figure 6.5: 300 K *ab* plane optical conductivity of $(\mathrm{La}_{0.4}\mathrm{Pr}_{0.6})_{1.2}\mathrm{Sr}_{1.8}\mathrm{Mn}_2\mathrm{O}_7$ in 0 (solid line) and 30 T (dashed line) magnetic fields ($H \parallel c$). The inset shows the measured *ab* plane reflectance ratio at 5, 10, 15, 20, 25, and 30 T (top to bottom). The data are taken upon increasing field. (after Ref. [43])

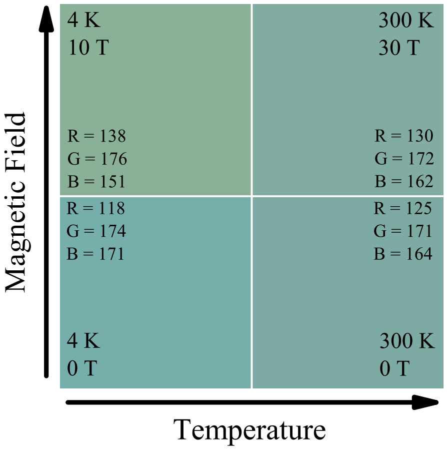

Figure 6.6: Schematic view of the temperature and magnetic field-induced color changes in $(La_{0.4}Pr_{0.6})_{1.2}Sr_{1.8}Mn_2O_7$. A comparison to transmittance data allows an estimated scaling constant of K=1.22x10^{-5} cm to be determined. This K value was used in the calculation of the other colors. The RGB values for each swatch are given as well. (after Ref. [43])

those at base temperature (Fig. 6.1). Under applied magnetic field, the entire visible spectrum redshifts. Given high enough magnetic field, the full spin-glass insulator to ferromagnetic metal transition can likely be realized, inducing magneto-dielectric effects similar to those at 4 K. Recent ^{139}La NMR studies reveal field-induced long-range ferromagnetic order up to 330 K in $La_{1.2}Sr_{1.8}Mn_2O_7$, [235] suggesting that 300 K magnetochromic effects may also be present in the parent compound.

We employed standard color rendering techniques to visualize the magnetochromic and thermochromic effects in $(La_{0.4}Pr_{0.6})_{1.2}Sr_{1.8}Mn_2O_7$ (Fig. 6.6). [65] In the calculation of color, the 300 K (0 T) data were normalized to K=1.22×10^{-5} cm, chosen by a comparison to room temperature transmittance. The same value of K was used to normalize the other data, allowing us to compare overall color changes to those of the 300 K, zero field data. Examination of the color panel shows a distinct color change between the 0 and 10 T data at low temperature, whereas there is only modest thermochromism as temperature is increased. The 300 K data taken at 30 T show a small change in color compared to that of the 0 T room temperature data. This shows that the color change is quenched by temperature although larger fields can probably drive the spin-glass insulator to ferromagnetic metal transition at 300 K. In this case, we anticipate magnetochromic effects similar to those at low temperature. The calculated RGB values are presented (Fig. 6.6) to quantify these color properties.

6.4 High Energy MagnetoDielectric Response

Figure 6.7 (a) displays the real part of the dielectric response as a function of energy at low temperature. At zero field, the dispersive response exhibits typical behavior of a semiconductor, with an overall positive ϵ_1 except for the regions with strong phonon dispersions. The dispersive response of the Pr-substituted compound in the high field state is different due to the change in the ground state. ϵ_1 crosses zero at the screened plasma energy ~1.2 eV, recrosses into positive territory at ~0.6 eV, and crosses zero several times again at low energy due to the dispersive phonon behavior (inset, Fig. 6.7 (a)). To emphasize the difference between the zero and high field dielectric response of $(La_{0.4}Pr_{0.6})_{1.2}Sr_{1.8}Mn_2O_7$, we plot the dielectric contrast $\Delta\epsilon_1/\epsilon_1 = [\epsilon_1(E,H) - \epsilon_1(E,0)]/\epsilon_1(E,0)$ (Fig. 6.7 (b)). The size of the dielectric contrast depends on energy. It is as large as ~100% near 0.8 eV. This is the range of Mn charge transfer and on-site excitations. In selected phonon regimes (near 6, 60, 77, 90 meV), the dielectric contrast is enormous, on the order of 10000%. The 4.2 K dielectric contrast is a direct consequence of the robust low temperature spin-glass insulator to ferromagnetic metal transition and strong spin-lattice-charge cross coupling in $(La_{0.4}Pr_{0.6})_{1.2}Sr_{1.8}Mn_2O_7$.

It is clearly desirable to design and assemble multifunctional devices that operate

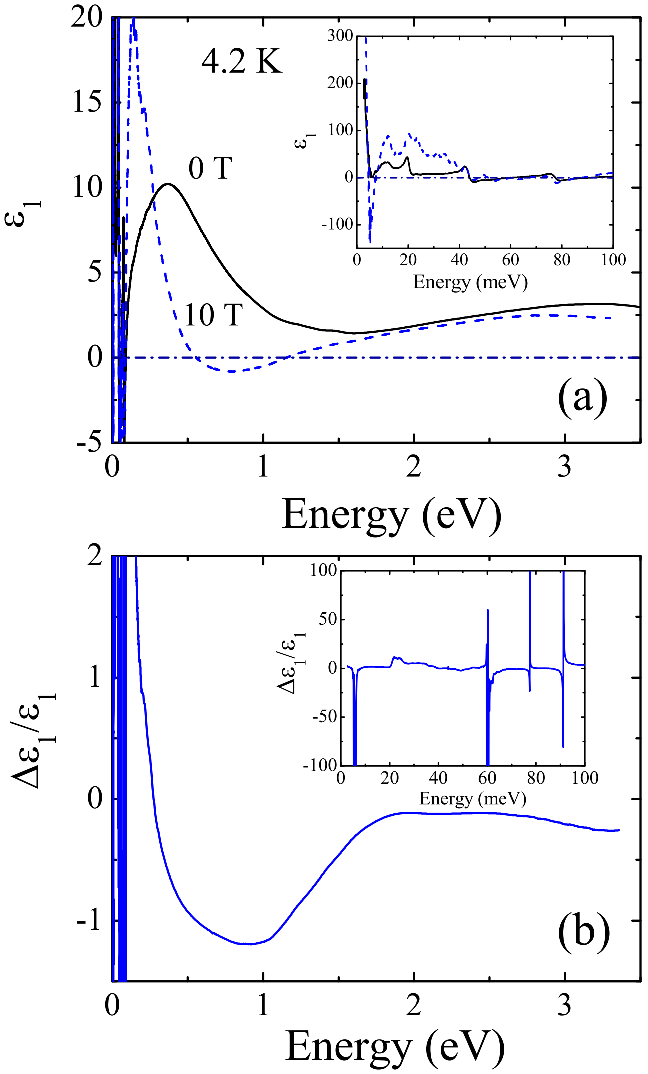

Figure 6.7: (a) Dielectric response of $(La_{0.4}Pr_{0.6})_{1.2}Sr_{1.8}Mn_2O_7$ for H=0 (solid line) and 10 T (dashed line) ($H \parallel c$) at 4.2 K, as determined by Kramers-Kronig analysis of the measured reflectance . (b) The high-energy dielectric contrast, $\Delta\epsilon_1/\epsilon_1$, for H=0 and 10 T. (after Ref. [44])

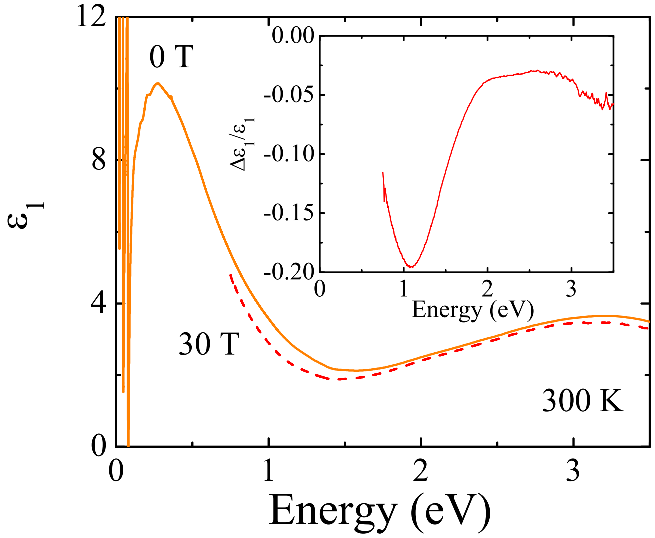

Figure 6.8: Dielectric response of $(La_{0.4}Pr_{0.6})_{1.2}Sr_{1.8}Mn_2O_7$ for H=0 (solid line) and 30 T (dashed line) ($H \parallel c$) at 300 K, as determined by Kramers-Kronig analysis of the measured reflectance. The inset displays the high-energy dielectric contrast, $\Delta\epsilon_1/\epsilon_1$, for H=0 and 30 T. (after Ref. [44])

at higher temperatures. Materials that exhibit room temperature magnetoelectric coupling are therefore needed. To this end, we have employed the remnants of the spin-glass insulator to ferromagnetic metal transition in $(La_{0.4}Pr_{0.6})_{1.2}Sr_{1.8}Mn_2O_7$ to achieve a 300 K high energy magnetodielectric effect. Figure 6.8 displays the room temperature dielectric properties of $(La_{0.4}Pr_{0.6})_{1.2}Sr_{1.8}Mn_2O_7$ at 0 and 30 T. The dispersive response shifts to lower energy in applied magnetic field, consistent with the previous observation of redshifted oscillator strength in the ferromagnetic metal state. [43] Strikingly, the dielectric contrast displays a 20% change near 1.1 eV (inset of Fig. 6.8). The high energy magnetodielectric effect in the far and middle infrared region could not be assessed in our experiments at the NHMFL. We anticipate that the dielectric contrast will be larger based upon its low temperature behavior. Although weaker than that at 4.2 K, this finding demonstrates that electronic transitions can be harnessed for 300 K high energy magnetodielectric effects.

The high energy magnetodielectric effect in $(La_{0.4}Pr_{0.6})_{1.2}Sr_{1.8}Mn_2O_7$ is substantially larger than that in mixed-valent $K_2V_3O_8$, Kagomé staircase compound $Ni_3V_2O_8$, and frustrated $HoMnO_3$, oxides where magnetoelastic/magnetoelectric coupling is important. [9, 37, 138] As mentioned previously, this stronger dielectric contrast is directly related to exploiting the field-induced insulator to metal transition. Reviewing the Tomioka-Tokura global phase diagram in complex perovskites, [8] the double layer manganite $(La_{0.4}Pr_{0.6})_{1.2}Sr_{1.8}Mn_2O_7$ is sitting in close proximity to the phase boundary and is therefore susceptible to physical tuning - even when the transition itself is no longer well-defined. Control of disorder therefore provides an important route for tuning the high energy magnetodielectric effect. [8, 43]

It is interesting to compare the high energy magnetodielectric effect in double layer manganite $(La_{0.4}Pr_{0.6})_{1.2}Sr_{1.8}Mn_2O_7$ with static results. Due to the large DC conductivity of these single crystal samples, we investigate the low frequency magnetic response in terms of the impedance rather than ϵ_1. [236, 237] The inset of Fig. 6.9 displays the low frequency (30 kHz) impedance as a function of magnetic field at 4.2 K. The high impedance insulating state at 0 T is suppressed with increasing magnetic field, leading to a large change in impedance between 0 and 5 T. As the field decreases towards 0 T, there is a small increase in impedance, but the sample remains trapped in the metastable low impedance state. The phase of the complex impedance displays similar behavior. Field-induced transitions and trapping in a metastable state have been observed in resistivity measurements of $(La_{0.4}Pr_{0.6})_{1.2}Sr_{1.8}Mn_2O_7$, [125] and were attributed to the strong magnetoresistive coupling in this system. This static spin-charge coupling persists to higher temperatures. The main panel of Fig. 6.9 displays the 300 K magneto-impedance contrast as a function of magnetic field. The impedance of the sample changes up to 2.5% in a 5 T applied field. This magneto-impedance is completely non-hysteretic, different from that at low temperatures. Similar magneto-impedance has been observed close to the ferromagnetic ordering temperature in other manganites, [236, 237] and was attributed to the dependence of the skin depth on both magnetic field and frequency. Clearly, these room temperature effects represent significant spin-charge coupling persisting to temperatures well above the magnetic transition temperature, in line with the 300 K high energy magnetodielectric effect.

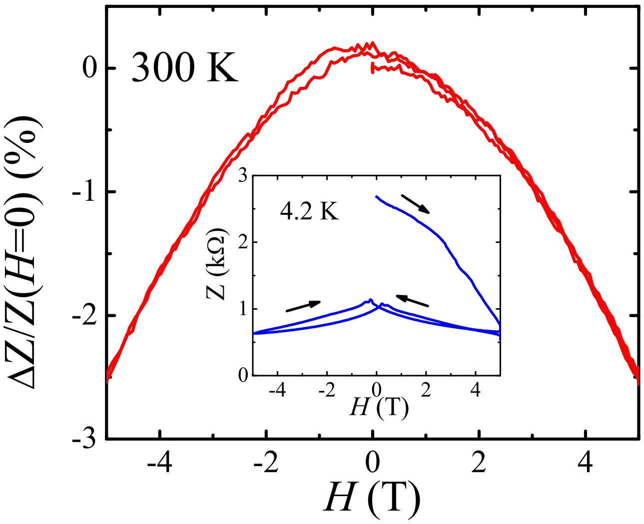

Figure 6.9: The magneto-impedance contrast of $(La_{0.4}Pr_{0.6})_{1.2}Sr_{1.8}Mn_2O_7$ as a function of magnetic field ($H \parallel c$) at 300 K. The inset displays the magnitude of the impedance as a function of magnetic field ($H \parallel c$) at 4.2 K. The sample was zero-field cooled. (after Ref. [44])

Chapter 7

Conclusion

In this dissertation, I present spectroscopic studies of three different types of transition metal oxides: VO_x nanoscrolls, $VOHPO_4 \cdot \frac{1}{2}H_2O$, and $(La_{0.4}Pr_{0.6})_{1.2}Sr_{1.8}Mn_2O_7$. My analysis of the experimental results concentrates on optical gap tuning, lattice and charge dynamics, hydrogen bonding, spin-lattice-charge coupling, and high energy magnetodielectric effects.

Work on the VO_x nanoscrolls focused on the chemical structure-physical property correlations as well as charge and lattice dynamics. The sheet distance was adjusted with various amine templates, allowing us to alter the scroll size. Thus, the effect of sheet distance on the optical properties could be examined. In the pristine nanoscrolls, the electronic structure strongly resembles that of other bulk, low-dimensional, and molecular vanadates. [38] The 1.2 eV band is assigned as a superposition of V^{4+} $d \rightarrow d$ and $V^{4+} \rightarrow V^{5+}$ charge transfer excitations, and the features above 3 eV are attributed to O $2p \rightarrow$ V $3d$ charge transfer excitations. Evidence for the dual character of the 1.2 eV band comes from both spectral and structural data, in particular, the band shape as well as trends with decreasing temperature. The 5 eV excitation shows a modest sheet distance dependence, redshifting with increasing tube diameter. This suggests that it is a radially-directed excitation. We find that the optical gap is ∼0.56 eV at room temperature and ∼0.65 eV at 4.2 K. Although it varies with temperature, the optical gap does not depend systematically on tube size. At the same time, selected V-O-V stretching modes sharpen and redshift with increasing sheet distance. We attribute these trends to the microscopic manifestations of strain, which changes with curvature. A low frequency mode is observed at 113 cm^{-1}, which is assigned as the screw-like motion of the scrolls. We also measured the variable temperature optical spectra of metal ion substituted vanadate nanoscrolls to understand the charge dynamics and test the applicability of the rigid band model in these compounds. [40] We unexpectedly observe a bound carrier excitation in the metal substituted nanoscrolls rather than a metallic response that was predicted by theory. This bound carrier excitation is localized in the far infrared due to a combination of inhomogeneous charge disproportionation, electron-electron correlation, and chemical disorder effects. We propose an alternate band filling picture that accounts for the charge localization. Analysis of the vibrational properties shows that the 575 cm^{-1} V-O-V equatorial stretching mode redshifts with ion substitution, indicating that ion exchange modifies both the local curvature and charge environment. Charge effects also redshift 3.9 and 5.0 eV electronic excitations.

In order to understand the structure-property relationships in $VOHPO_4 \cdot \frac{1}{2}H_2O$, we investigated the low-energy magnetic susceptibility, electron spin resonance, and lattice dynamics of this $S = 1/2$ Heisenberg antiferromagnet. [41] A pair of peaks in the far infrared spectral response are of interest as possible magnetic excitations. We propose that a dynamic Dzyaloshinskii-Moriya mechanism may explain the activation and directional dependence of the singlet to triplet excitation in the far infrared, and we identify two low-energy lattice modes that may facilitate this coupling. Future high magnetic field investigations will be required to confirm the magnetic character of these peaks and conclusively distinguish these features from conventional phonons.

The spin gap values are compared with those obtained from magnetic susceptibility, electron spin resonance, and neutron scattering. Although the V-O-P-O-V interaction dominates the magnetic properties of $VOHPO_4 \cdot \frac{1}{2}H_2O$, our model fits of the susceptibility show that weak interdimer coupling is on the order of a few percent. Variable temperature spectral results also highlight a subtle structural phase transition near 180 K. A low temperature enhancement of hydrogen bonding drives this weak local distortion. The low lattice symmetry is important for activating the proposed magnetoelastic coupling. We also investigate the variable temperature color properties of $VOHPO_4 \cdot \frac{1}{2}H_2O$. [42] $VOHPO_4 \cdot \frac{1}{2}H_2O$ displays a strong color band centered at ~1.5 eV that derives from excitations between crystal field split $3d$ levels of the V^{4+} centers. These features also redshift with decreasing temperature, indicative of enhanced low temperature hydrogen bonding between layers. First principle electronic structure calculations are in progress to complement this experimental work.

We report a comprehensive optical investigation of $(La_{0.4}Pr_{0.6})_{1.2}Sr_{1.8}Mn_2O_7$, undertaken to examine the microscopic aspects of spin, lattice, charge, and orbital coupling through the spin-glass insulator to ferromagnetic metal transition. [43] Overall, spectral weight shifts to lower energy with applied magnetic field, although the material displays far-infrared charge localization and a pseudogap due to ferromagnetic domain formation and modest dc conductivity in the high field ferromagnetic metallic state, different from that in the double-layer parent material. Several Mn-O and O-Mn-O stretching and bending vibrational modes soften through the field-driven transition, indicative of a structural change. Using the Tomioka-Tokura phase diagram picture, [8] we find that the ferromagnetic metallic state, although quenched by chemical doping, is revived in a modified form by the application of magnetic field by driving the system from the disordered spin-glass insulator phase into the ferromagnetic metal regime. The optical properties were also used to map the $H-T$ phase diagram, and we find that the lattice response to the field is slower than that of spin and charge. We also observed a large high energy magnetodielectric contrast in this bilayer manganite, a direct consequence of field driven spin-glass insulator to ferromagnetic metal transition. [44] The remnants of the transition can be used to achieve dielectric contrast at room temperature. This discovery suggests that electronic mechanisms such as the metal-insulator transition, charge ordering, and orbital ordering can be exploited to give substantial dielectric contrast in other materials.

Bibliography

Bibliography

[1] *Transition Metal Oxides*, edited by C.N.R. Rao (John Wiley & Sons, Inc., 1998).

[2] K. J. Choi, M. Biegalski, Y. L. Li, A. Sharan, J. Schubert, R. Uecker, P. Reiche, Y. B. Chen, X. Q. Pan, V. Gopalan, L. Q. Chen, D. G. Schlom, C. B. Eom, Science **306**, 1005 (2004).

[3] A. Earnshaw and N. Greenwood, *Chemistry of the Elements, Second Edition* (Elsevier Butterworth-Heinemann, New York, 2005).

[4] *Colossal Magnetoresistive Oxides*, edited by Y. Tokura (Gordon and Breach Science Publishers, New York, 2000).

[5] A. Moreo, S. Yunoki, and E. Dagotto, Science **283**, 2034 (1999).

[6] E. Dagotto, *Nanoscale Phase Separation and Colossal Magneto-resistance*, (Springer, 2003).

[7] *Colossal Magnetoresistive Manganites*, edited by T. Chatterji (Kluwer Academic Publishers, 2004).

[8] Y. Tomioka, and Y. Tokura, Phys. Rev. B **70**, 014432 (2004).

[9] R. C. Rai, J. Cao, S. Brown, J. L. Musfeldt, D. Kasinathan, D. J. Singh, G. Lawes, N. Rogado, R. J. Cava, and X. Wei, Phys. Rev. B **74**, 235101 (2006).

[10] P. Schiffer, A. P. Ramirez, W. Bao and S.-W. Cheong, Phys. Rev. Lett. **75**, 3336 (1995).

[11] S. Lefebvre, P. Wzietek, S. Brown, C. Bourbonnais, D. Jrome, C. Mzire, M. Fourmigu, and P. Batail, Phys. Rev. Lett. **85**, 5420 (2000).

[12] R. Tenne, L. Margulis, M. Genut, G. Hodes, Nature **360**, 444 (1992).

[13] M. Remskar, A. Mrzel, Z. Skraba, A. Jesih, M. Ceh, J. Demšar, P. Stadelmann, F. lévy, and D. Mihailovic, Science **292**, 479 (2001).

[14] R. Rosentsveig, A. Margolin, Y. Feldman, R. Popovitz-Biro, and R. Tenne, Chem. Mater. **14**, 471 (2002).

[15] Y. Feldman, E. Wasserman, D. J. Srolovitz, and R. Tenne, Science **267**, 222 (1995).

[16] R. S. Lee, J. Gavillet, M. Lamy de la Chapelle, A. Loiseau, J. -L. Cochon, D. Pigache, J.Thibault, and F. Willaime, Phys. Rev. B **64**, 121405 (2001).

[17] N. G. Chopra, R. J. Luyken, K. Cherrey, V. H. Crespi, M. L. Cohen, S. G. Louie, and A. Zettl, Science **269**, 966 (1995).

[18] P. Hoyer, Langmuir **12**, 1411 (1996)

[19] T. Kasuga, M. Hiramatsu, A. Hoson, T. Sekino, and K. Niihara, Adv. Mater. **11**, 1307 (1999).

[20] S. M. Liu, L. M. Gan, L. H. Liu, W. D. Zhang, and H. C. Zeng, Chem. Mater. **14**, 1391 (2002).

[21] Y. R. Hacohen, E. Grunbaum, R. Tenne, J. Sloan, and J. L. Hutchison, Nature **395**, 336 (1998).

[22] M. Nath and C. N. R. Rao, J. Am. Chem. Soc. **123**, 4841(2001).

[23] X. Shi, S. Han, R. J. Sanedrin, F. Zhou, and M. Selke, Chem. Mater. **14**, 1897 (2002).

[24] B. A. Hernandez, K. -S. Chang, E. R. Fisher, and P.K. Dorhout, Chem. Mater. **14**, 480 (2002).

[25] R. Tenne, Nature Nanotechnology, **1**, 103 (2006).

[26] F. Krumeich, H.-J. Muhr, M. Niederberger, F. Bieri, B. Schnyder, and R. Nesper, J. Am. Chem. Soc. **121**, 8324 (1999).

[27] H. -J. Muhr, F. Krumeich, U. P. Schönholzer, F. Bieri, M. Niederberger, L. J. Gauckler, and R. Nesper, Adv. Mater. **12**, 231 (2000)

[28] X. Y. Zhang, C. W. Lai, X. Zhao, D. Y. Wang, and J. Y. Dai, Appl. Phys. Lett. **87**, 143102 (2005).

[29] F. Wooten, *Optical Properties of Solids* (Academic Press, New York, 1972).

[30] J. Choi, Z. T. Zhu, J. L. Musfeldt, G. Ragghianti, D. Mandrus, B. C. Sales, and J. R. Thompson, Phys. Rev. B **65**, 054101 (2001).

[31] A. B. Sushkov, B. R. Jones, J. L. Musfeldt, Y. J. Wang, R. M. Achey, and N. S. Dalal, Phys. Rev. B **63**, 214408 (2001).

[32] Martin Dressel and Natalia Drichko, Chem. Rev. **104**, 5689 (2004).

[33] E. J. Singley, K. S. Burch, R. Kawakami, J. Stephens, D. D. Awschalom, and D. N. Basov, Phys. Rev. B **68**, 165204 (2003).

[34] L. Degiorgi, Rev. Mod. Phys., **71**, 687 (1999).

[35] G. Grüner, Rev. Mod. Phys., **60**, 1129 (1988).

[36] D. N. Basov, S. I. Woods, A. S. Katz, E. J. Singley, R. C. Dynes, M. Xu, D. G. Hinks, C. C. Homes, and M. Strongin, Science **283**, 49 (1999).

[37] R. C. Rai, J. Cao, J. L. Musfeldt, D. J. Singh, X. Wei, R. Jin, Z. X. Zhou, B. C. Sales, and D. Mandrus, Phys. Rev. B **73**, 075112 (2006).

[38] J. Cao, J. Choi, J. L. Musfeldt, S. Lutta, and M. S. Whittingham, Chem. Mater. **16**, 731 (2004).

[39] J. Cao, J. Choi, J. L. Musfeldt, S. Lutta, and M. S. Whittingham, Nanoscale Materials: From Science to Technology, Ch. 21, Nova Science Publishers, ISBN: 1-59454-910-9 (2006).

[40] J. Cao, J. L. Musfeldt, S. Mazumdar, N. Chernova, and M. S. Whittingham, to be published.

[41] J. Cao, J. T. Haraldsen, S. Brown, J. L.Musfeldt, J. R. Thompson, S. Zvyagin, J. Krzystek, M.-H. Whangbo, T. Barnes, S. E. Nagler, and C. C. Torardi, Phys. Rev. B **72**, 214421 (2005).

[42] J. Cao, J. L. Musfeldt, B. Rahaman, T. Saha-Dasgupta, D. J. Singh, C. C. Torardi, and B. C. Sales, to be published.

[43] J. Cao, J. T. Haraldsen, R. C. Rai, S. Brown, J. L. Musfeldt, X. Wei, Y.-J. Wang, M. Apostu, R. Suryanarayanan, and A. Revcolevschi, Phys. Rev. B **74**, 045113 (2006).

[44] J. Cao, R.C. Rai, S. Brown, J.L. Musfeldt, R. Tackett, G. Lawes, X. Wei, Y.J. Wang, M. Apostu, R. Suryanarayanan, and A. Revcolevschi, to be published.

[45] P.Y. Zavalij and M.S. Whittingham, Acta. Cryst. B **55**, 627 (1999).

[46] X. Wang, L. Liu, R. Bontchev, and J. Jacobson, Chem. Commun., 1009 (1998).

[47] L. Krusin-Elbaum, D. M. Newns, H. Zeng, V. Derycke, and J. Z. Sun, Nature **431**, 672 (2004).

[48] P. Amorós, R. Ibáñez, E. Martínez-Tamayo, A. Beltrán-Porter, and D. Beltrán-Porter, Mat. Res. Bull. **24**, 1347 (1989).

[49] C. C. Torardi and J. C. Calabrese, Inorg. Chem. **23**, 1308 (1984).

[50] J. W. Johnson, D. C. Johnston, A. J. Jacobson, and J. F. Brody, J. Am. Chem. Soc. **106**, 8123 (1984).

[51] D. Beltrán-Porter, A. Beltrán-Porter, P. Amoros, R. Ibañez, E. Martinez, A. Le Bail, G. Ferey, and G. Villeneuve, Eur. J. Solid State Inorg. Chem. **28**, 131 (1991).

[52] G. Villeneuve, K. S. Suh, P. Amorós, N. Casañ-Pastor, and D. Beltrán-Porter, Chem. Mater. **4**, 108 (1992).

[53] G. W. Coulston, S. R. Bare, H. Kung, K. Birkeland, G. K. Bethke, R. Harlow, N. Herron, and P. L. Lee, Science **275**, 191 (1997).

[54] M. Kubota, H. Fujioka, K. Hirota, K. Ohoyama, Y. Moritomo, H. Yoshizawa, and Y. Endoh, J. Phys. Soc. Jpn. **69**, 1606 (2000).

[55] M. Apostu, R. Suryanarayanan, A. Revcolevschi, H. Ogasawara, M. Matsukawa, M. Yoshizawa, and N. Kobayashi, Phys. Rev. B **64**, 012407 (2001).

[56] H. J. Lee, K. H. Kim, M. W. Kim, T. W. Noh, B. G. Kim, T. Y. Koo, S.-W. Cheong, Y. J. Wang, and X. Wei, Phys. Rev. B **65**, 115118 (2002).

[57] B. Lorenz, A. P. Litvinchuk, M. M. Gospodinov, and C. W. Chu, Phys. Rev. Lett. **92**, 087204 (2004).

[58] A. S. Alexandrov and A. M. Bratkovsky, J. Appl. Phys. **87**, 5016 (2000).

[59] A. S. Alexandrov and A. M. Bratkovsky, Phys. Rev. B. **60**, 6215 (1999).

[60] H. K. Ng, Y. J. Wang, *In Physics Phenomena at High Magnetic Field-II*;Z. Fisk, L. Gor'kov, D. Meltzer, R. Schrieffer, Eds.; World Scientific: Singapore, 1995.

[61] G.-F. Li, *FTIR Spectroscopic Studies of Spin-Peierles Materials*, Master's Thesis, State University of New York at Binghamton, 1997.

[62] Z.-T. Zhu, *Spectroscopic Studies of Charge Density Wave Bronzes and Fullerene Polymers*, Ph. D Dissertation, State University of New York at Binghamton, 2001.

[63] M. Niederberger, H.-J. Muhr, F. Krumeich, F. Bieri, D. Günther, and R. Nesper, Chem. Mater. **12**, 1995 (2000).

[64] S. Lutta, A. Dobley, K. Ngala, S. Yang, P.Y. Zavalij, and M.S. Whittingham, Mater. Res. Soc. Symp. **703**, V8.3 (2002).

[65] F. W. Billmeyer and M. Saltzman, *Principles of Color Technology, 3rd Ed.*, Wiley, New York (2000).

[66] J. L. Musfeldt, D. B. Tanner, and A. J. Paine, J. Opt. Soc. Am. A **10** 2648 (1993).

[67] C.N. Rao, G.V. Subba Rao, National Bureau of Standards Report No. NSRDS-NBS49, 1974.

[68] L. Krusin-Elbaum and M. Wittmer, J. Electrochem. Soc. **135**, 2610 (1998).

[69] M. DiDomenico, Jr. and S. H. Wemple, Phys. Rev. **166**, 565 (1968).

[70] L. L. Chase, Phys. Rev. B **10**, 2226 (1974).

[71] J. A. Borchers, R. W. Erwin, S. D. Berry, D. M. Lind, J. F. Ankner, E. Lochner, K. A. Shaw, and D. Hilton, Phys. Rev. B **51**, 8276 (1995).

[72] S. Iijima, Nature **354**, 56 (1991).

[73] M. Côté, M. L. Cohen, and D. J. Chadi, Phys. Rev. B **58**, R4277 (1998).

[74] G. Seifert, H. Terrones, M. Terrones, G. Jungnickel, and T. Frauenheim, Phys. Rev. Lett. **85**, 146 (2000).

[75] G. Seifert, Th. Köhler, H. M. Urbassek, E. Hernández, and T. Frauenheim, Phys. Rev. B **63**, 193409 (2001).

[76] G. Seifert, E. Hernández, Chem. Phys. Lett. **318**, 355 (2000).

[77] G. Seifert, H. Terrones, M. Terrones, and T. Frauenheim, Solid State Commun. **115**, 635 (2000).

[78] G. Seifert, H. Terrones, M. Terrones, G. Jungnickel, and T. Frauenheim, Solid State Commun. **114**, 245 (2000).

[79] S. M. Lee, Y. H. Lee, Y. G. Hwang, J. Elsner, D. Porezag, and T. Frauenheim, Phys. Rev. B **60**, 7788 (1999).

[80] A. Rubio, J. L. Corkill, and M. L. Cohen, Phys. Rev. B **49**, 5081 (1994).

[81] D. Sánchez-Portal and E. Hernández, Phys. Rev. B **66**, 235415 (2002).

[82] G. L. Frey, S. Elani, M. Homyonfer, Y. Feldman, and R. Tenne, Phys. Rev. B **57**, 6666 (1998).

[83] J.-F. Xu, R. Czerw, S. Webster, and D. L. Carroll, J. Ballato, R. Nesper, Appl. Phys. Lett. **81**, 1711 (2002).

[84] R. D. Luttrell, S. Brown, J. Cao, J. L. Musfeldt, R. Rosentsveig, and R. Tenne, Rev. B **73**, 035410 (2006).

[85] C. Wu, W. Qin, G. Qin, D. Zhao, J. Zhang, S. Huang, S. Lü, H. Liu, and H. Lin, Appl. Phys. Lett. **82**, 520 (2003).

[86] P. V. Teredesai, F. L. Deepak, A. Govindaraj, C. N. R. Rao and A. K. Sood, J. Nanosci. Nanotechno. **2**, 495 (2002).

[87] C. N. R. Rao and M. Nath, Dalton Trans., 1 (2003).

[88] M. Wörle, F. Krumeich, F. Bieri, H.-J. Muhr, R. Nesper, Z. Anorg. Allg. Chem. **628**, 2778 (2002).

[89] C. O'Dwyer, D. Navas, V. Lavayen, E. Benavente, M. A. Santa Ana, G. González, S. B. Newcomb, and C. M. Sotomayor Torres, Chem. Mater. **18**, 3016 (2006).

[90] Y. Wang and G. Cao, Chem. Mater. **18**, 2787 (2006).

[91] J. M. Reinoso, H. -J. Muhr. F. Krumeich, F. Bieri, and R. Nesper, Helv. Chim. Acta **83**, 1724 (2000).

[92] S. Nordlinder, L. Nyholm, T. Gustafsson, and K. Edstrom, Chem. Mater. **18**, 495 (2006).

[93] E. Vavilova, I. Hellmann, V. Kataev, C. Täschner, B. Büchner, and R. Klingeler, Phys. Rev. B **73**, 144417 (2006).

[94] A. G. Souza Filho, O. P. Ferreira, E. J. G. P. Santos, J. Mendes Filho, and O. L. Alves, Nano Lett. **4**, 2099 (2004).

[95] M. S. Whittingham, Chem. Rev. **104**, 4271 (2004).

[96] D. J. Singh, G. E. Jellison Jr., and L. A. Boatner (unpublished).

[97] G. E. Jellison Jr., L. A. Boatner, and C. Chen, Opt. Mater. **15**, 103 (2000).

[98] M. Morcrette, J-B. Leriche, S. Patoux, C. Wurm, and C. Masquelier, Electrochem. Solid-State Lett. **6**, A80 (2003).

[99] M. Roca, P. Amorós, J. Cano, M. D. Marcos, J. Alamo, A. Beltrán-Porter, and D. Beltrán-Porter, Inorg. Chem. **37**, 3167 (1998).

[100] D. A. Tennant, S. E. Nagler, A. W. Garrett, T. Barnes, and C. C. Torardi, Phys. Rev. Lett. **78**, 4998 (1997).

[101] A. W. Garrett, S. E. Nagler, T. Barnes, and B. C. Sales, Phys. Rev. B **55**, 3631 (1997).

[102] A. W. Garrett, S. E. Nagler, D. A. Tannant, B. C. Sales, and T. Barnes, Phys. Rev. Lett. **79**, 745 (1997).

[103] D. C. Johnston, J. W. Johnson, D. P. Goshorn, and A. J. Jacobson, Phys. Rev. B **35**, 219 (1987).

[104] R. S. Eccleston, T. Barnes, J. Brody, and J. W. Johnson, Phys. Rev. Lett. **73**, 2626 (1994).

[105] S. Petit, S. A. Borshch, and V. Robert, J. Am. Chem. Soc. **124**, 1744 (2002).

[106] G. S. Uhrig and B. Normand, Phys. Rev. B. **58**, R14705 (1998).

[107] J. Kikuchi, K. Motoya, T. Yamauchi, and Y. Ueda, Phys. Rev. B **60**, 6731 (1999).

[108] A.V. Prokofiev, F. Büllesfeld, W. Assmus, H. Schwenk, D. Wichert, U. Löw, and B. Lüthi, Eur. Phys. J. B **5**, 313 (1998).

[109] C. C. Torardi, Z. G. Li, H. S. Horowitz, W. Liang, and W.-H. Whangbo, J. Solid State Chem **119**, 349 (1995).

[110] G. S. Uhrig and B. Normand, Phys. Rev. B **63**, 134418 (2001).

[111] U. Kuhlmann, C. Thomsen, A. V. Prokofiev, F. Büllesfeld, E. Uhrig, M. Anton, C. Gross, and W. Assmus, Phys. Rev. B **66**, 064420 (2002).

[112] L. M. L. Daku, S. Borshch, V. Robert, and B. Bigot, Phys. Rev. B **63**, 174439 (2001).

[113] P. W. Anderson and H. Hasegawa, Phys. Rev. **100**, 675 (1955).

[114] Y. Moritomo, A. Asamitsu, H. Kuwahara, and Y. Tokura, Nature (London) **380**, 141 (1996).

[115] J. F. Mitchell, D. N. Argyriou, J. D. Jorgensen, D. G. Hinks, C. D. Potter, and S. D. Bader, Phys. Rev. B **55**, 63 (1997).

[116] T. G. Perring, G. Aeppli, Y. Moritomo, and Y. Tokura, Phys. Rev. Lett. **78**, 3197 (1997).

[117] M. Matsukawa, M. Narita, T. Nishimura, M. Yoshizawa, M. Apostu, R. Suryanarayanan, A. Revcolevschi, K. Itoh, and N. Kobayashi, Phys. Rev. B **67**, 104433 (2003).

[118] F. Wang, A. Gukasov, F. Moussa, M. Hennion, M. Apostu, R. Suryanarayanan, and A. Revcolevschi, Phys. Rev. Lett. **91**, 047204 (2003).

[119] J. D. Woodward, J. Choi, J. L. Musfeldt, J. T. Haraldsen, M. Apostu, R. Suryanarayanan, and A. Revcolevschi, Phys. Rev. B **69**, 104415 (2004).

[120] M. Matsukawa, M. Chiba, A. Akasaka, R. Suryanarayanan, M. Apostu, A. Revcolevschi, S. Nimori, and N. Kobayashi, Phys. Rev. B **70**, 132402 (2004).

[121] Y. Tokunaga, M. Tokunaga, and T. Tamegai, Phys. Rev. B **71**, 012408 (2005).

[122] A. Gukasov, F. Wang, B. Anighoefer, L. He, R. Suryanarayanan, and A. Revcolevschi, Phys. Rev. B **72**, 092402 (2005).

[123] I. Gordon, P. Wagner, V. V. Moshchalkov, Y. Bruynseraede, M. Apostu, R. Suryanarayanan, and A. Revcolevschi, Phys. Rev. B **64**, 092408 (2001).

[124] P. Wagner, I. Gordon, V. V. Moshchalkov, Y. Bruynseraede, M. Apostu, R. Suryanarayanan, and A. Revcolevschi, Europhys. Lett **58**, 285 (2002).

[125] M. Matsukawa, K. Akasaka, H. Noto, R. Suryanarayanan, S. Nimori, M. Apostu, A. Revcolevschi, and N. Kobayashi, Phys. Rev. B **72**, 064412 (2005).

[126] F. Moussa, M. Hennion, F. Wang, A. Gukasov, R. Suryanarayanan, M. Apostu, and A. Revcolevschi, Phys. Rev. Lett. **93**, 107202 (2004).

[127] J. Hemberger, P. Lunkenheimer, R. Fichtl, H.-A. Krug von Nidda, V. Tsurkan, and A. Loidl, Nature (London) **434**, 364 (2005).

[128] P. Lunkenheimer, R. Fichtl, J. Hemberger, V. Tsurkan, and A. Loidl, Phys. Rev. B **72**, 060103(R) (2005).

[129] S. Weber, P. Lunkenheimer, R. Fichtl, J. Hemberger, V. Tsurkan, and A. Loidl, Phys. Rev. Lett. **96**, 157202 (2006).

[130] T. Kimura, T. Goto, H. Shintani, K. Ishizaka, T. Arima, and Y. Tokura, Nature **426**, 55 (2003).

[131] N. S. Rogado, J. Li, A. W. Sleight, and M. A. Subramanian, Adv. Mater. **17**, 2225 (2005).

[132] M. A. Subramanian, T. He, J. Chen, N. S. Rogado, T. G. Calvarese, and A. W. Sleight, Adv. Mater. **18**, 1737 (2006).

[133] N. Hur, S. Park, P. A. Sharma, S. Guha, and S-W. Cheong, Phys. Rev. Lett. **93**, 107207 (2004).

[134] B. Lorenz, Y. Q. Wang, Y. Y. Sun, and C. W. Chu, Phys. Rev. B **70**, 212412 (2004).

[135] C.-H. Yang, T.Y. Koo, and Y.H. Jeong, Solid State Commun. **134**, 299 (2005).

[136] C. Zhou and D. M. Newns, J. Appl. Phys. **82**, 3081 (1997).

[137] M. Stengel and N. A. Spaldin, Nature **443**, 679 (2006).

[138] R. C. Rai, J. Cao, J. L. Musfeldt, S.B. Kim, S.-W. Cheong, and X. Wei (unpublished).

[139] W. J. Padilla, D. Mandrus, and D. N. Basov, Phys. Rev. B **66**, 035120 (2002).

[140] R. Rückamp, E. Benckiser, M. W. Haverkort, H. Roth, T. Lorenz, A. Freimuth, L. Jongen, A. Möller, G. Meyer, P. Reutler, B. Büchner, A. Revcolevschi, S-W. Cheong, C. Sekar, G. Krabbes, and M. Grüninger, New J. Phys. **7**, 144 (2005).

[141] V. C. Long, Z. Zhu, J. L. Musfeldt, X. Wei, H.-J. Koo, M.-H. Whangbo, J. Jegoudez, and A. Revcolevschi, Phys. Rev. B **60**, 15721 (1999).

[142] C. Presura, D. Van der Marel, M. Dischner, C. Geibel, and R. K. Kremer, Phys. Rev. B **62**, 16522 (2000).

[143] H. W. Verleur, A. S. Barker, Jr., and C. N. Berglund, Phys. Rev. **172**, 788 (1968).

[144] S. Shin, S. Suga, M. Taniguchi, M. Fujisawa, H. Kanzaki, A. Fujimori, H. Daimon, Y. Ueda, K. Kosuge, and S. Kachi, Phys. Rev. B **41** 4993 (1990).

[145] J. Choi, J. L. Musfeldt, Y. J. Wang, H. -J. Koo, M. -H. Whangbo, J. Galy, and P. Millet, Chem. Mater. **14**, 924 (2002).

[146] J. Choi, L. A. W. Sanderson, J. L. Musfeldt, A. Ellern and P. Kögerler, Phys. Rev. B **68**, 064412 (2003).

[147] A. B. Sushkov, J. L. Musfeldt, X. Wei, S. A. Crooker, J. Jegoudez, and A. Revcolevschi, Phys. Rev. B. **66**, 054439 (2002).

[148] P. Chen, X. Wu, X. Sun, J. Lin, W. Ji, and K. L. Tan, Phys. Rev. Lett. **82**, 2548 (1999).

[149] J. E. Riggs, D. B. Walker, D. L. Carroll, and Y. -P. Sun, J. Phys. Chem. B **104**, 7071 (2000).

[150] M. N. Popova, A. B. Sushkov, S. A. Golubchik, B. N. Mavrin, V. N. Denisov, B. Z. Malkin, A. L. Iskhakova, M. Isobe, and Y. Ueda, J. Exp. theor. Phys. **88**, 1186 (1999).

[151] R. Lopez, T.E. Haynes, L.A. Boatner, L.C. Feldman, and R.F. Haglund, Phys. Rev. B., **65**, 224113 (2002).

[152] L. Abello, E. Husson, Y. Repelin, and G. Lucazeau, Spectrochim. Acta **39A**, 641 (1983).

[153] J. Kürti, G. Kresse, and H. Kuzmany, Phys. Rev. B **58**, R8869 (1998).

[154] F.J. Morin, Phys. Rev. Lett., **3**, 34 (1959).

[155] H. S. Choi, J. S. Ahn, J. H. Jung, T. W. Noh, and D. H. Kim, Phys. Rev. B., **54**, 4621 (1996).

[156] R. Lopez, L. A. Boatner, T. E. Haynes, R. F Haglund, and L. C. Feldman, Appl. Phys. Lett., **79**, 3161 (2001).

[157] U. Fano, Phys. Rev. **124**, 1886 (1961).

[158] H. L. Liu, D. B. Tanner, H. Berger, and G. Margaritondo, Physica C **311**, 197 (1998).

[159] J. Choi, J. L. Musfeldt, J. He, R. Jin, J. R. Thompson, D. Mandrus, X. N. Lin, V. A. Bondarenko, and J. W. Brill, Phys. Rev. B **69**, 085120 (2004).

[160] Z.-T. Zhu, J. L. Musfeldt, Z. S. Teweldemedhin, and M. Greenblatt, Phys. Rev. B **65**, 214519 (2002).

[161] E. Cazzanelli, G. Mariotto, S. Passerini, and F. Decker, Solid State Ionics **70-71**, 412 (1994).

[162] J. Choi, J. L. Musfeldt, G. Yu. Rudko, J. Jegoudez, and A. Revcolevschi, Solid State Commun. **123**, 167 (2002).

[163] B. Bleaney and K. D. Bowers, Proc. R. Soc. London, **A214**, 451 (1952).

[164] D. C. Johnston, R. K. Kremer, M. Troyer, X. Wang, A. Klümper, S. L. Bud'ko, A. F. Panchula, and P. C. Canfield, Phys. Rev. B **61**, 9558 (2000).

[165] J.N. McElearney, D.B. Losee, S. Merchant, and R.L. Carlin, Phys. Rev. B **7**, 3314 (1973).

[166] W. E. Hatfield, J. Appl. Phys. **52**, 1985 (1981).

[167] A. W. Garrett, Ph.D. thesis, University of Florida, 1998.

[168] Y. Furukawa, A. Iwai, K. Kumagai, and A. Yakubovsky, J. Phys. Soc. Jpn. **65**, 2393 (1996).

[169] S. Petit, S. A. Borshch, and V. Robert, Inorg. Chem. **43**, 4210 (2004).

[170] J. Krzystek and J. U. von Schütz, Advances in Chemical Physics, v. LXXXVI, pp. 167-329, Edited by I. Prigogine and S. A. Rice, 1993 John Willey & Sons, Inc.

[171] There must be a change in dipole moment during the vibration for a material to absorb infrared radiation.

[172] T. Rõõm, D. Hüvonen, U. Nagel, Y. -J. Wang, and R. K. Kremer, Phys. Rev. B **69**, 144410 (2004).

[173] T. Rõõm, U. Nagel, E. Lippmaa, H. Kageyama, K. Onizuka, and Y. Ueda, Phys. Rev. B **61**, 14342 (2000).

[174] T. Rõõm, D. Hüvonen, U. Nagel, J. Hwang, T. Timusk, and H. Kageyama, Phys. Rev. B **70**, 144417 (2004).

[175] J.B. Torrance and M. Tinkham, Phys. Rev. **187**, 587 (1969).

[176] J.B. Torrance and M. Tinkham, Phys. Rev. **187**, 595 (1969).

[177] A. Brun, P. Meyer, and B. Briat, J. Phys. C: Solid St. Phys. **13**, 5775 (1980).

[178] A. B. Sushkov, J. L. Musfeldt, Y. J. Wang, R. M. Achey, and N. S. Dalal, Phys. Rev. B **66**, 144430 (2002).

[179] A. A. Mukhin, V. D. Travkin, A. K. Zvezdin, S. P. Lebedev, A. Caneschi, and D. Gatteschi, Europhys. Lett. **44**, 778 (1998).

[180] M. Dressel, B. Gorshunov, K. Rajagopal, S. Vongtragool and A. A. Mukhin Phys. Rev. B. **67**, 060405(R) (2003).

[181] I. E. Dzyaloshinskii, Soviet Phys. JETP **5**, 1259 (1957).

[182] T. Moriya, Phys. Rev. **120**, 91 (1960).

[183] Y. Tanabe, T. Moriya, and S. Sugano, Phys. Rev. Lett. **15**, 1023 (1965).

[184] Y. R. Shen and N. Bloembergen, Phys. Rev. **143**, 372 (1966).

[185] P. A. Fluery and R. Loudon, Phys. Rev. **166**, 514 (1968).

[186] J. Lorenzana and G. A. Sawatzky, Phys. Rev. B **52**, 9576 (1995).

[187] O. Cépas, K. Kakurai, L. P. Regnault, T. Ziman, J. P. Boucher, N. Aso, M. Nishi, H. Kageyama, and Y. Ueda, Phys. Rev. Lett. **87**, 167205 (2001).

[188] O. Cépas and T. Ziman, Phys. Rev. B **70**, 024404 (2004).

[189] P. M. Champion and A. J. Sievers, J. Chem. Phys. **66**, 1819 (1977).

[190] W. Duffy and K.P. Barr, Phys. Rev. **165**, 647 (1968).

[191] T. Barnes, J. Riera, and D. A. Tennant, Phys. Rev. B **59**, 11384 (1999).

[192] T. Barnes, Phys. Rev. B **67**, 024412 (2003).

[193] M. Grove, P. Lemmens, G. Güntherodt, B.C. Sales, F. Büllesfeld, and W. Assmus, Phys. Rev. B. **61**, 6126 (2000).

[194] C. Ederer and N.A. Spaldin, Phys. Rev. B. **71**, 060401(R) (2005).

[195] M. A. Gîrtu, C.M. Wynn, W. Fujita, K. Awaga, and A.J. Epstein, Phys. Rev. B. **57**, R11058 (1998).

[196] A. A. Tsvetkov, F. P. Mena, P. H. M. van Loosdrecht, D. van der Marel, Y. Ren, A. A. Nugroho, A. A. Menovsky, I. S. Elfimov, and G. A. Sawatzky, Phys. Rev. B **69**, 075110 (2004).

[197] W. G. Fateley, F. R. Dollish, N. T. McDevitt, and F. F. Bentley, "Infrared and Raman Selection Rules for Molecular and Lattice Vibrations: The Correlation Method", Wiley-Intersience, New York (1972).

[198] G. Busca, F. Cavani, G. Centi, and F. Trifiro, J. Catal. **99**, 400 (1986).

[199] P. F. Miquel, E. Bordes, and J. L. Katz, J. Solid State Chem **124**, 95 (1996).

[200] N. Hiyoshi, N. Yamamoto, Y. Kamiya, E. Nishikawa, and T. Okuhara, Catal. Today **71**, 129 (2001);

[201] K. H. Kim, J. Y. Gu, H. S. Choi, G. W. Park, and T. W. Noh, Phys. Rev. Lett. **77**, 1877 (1996).

[202] E. B. Wilson, J. C. Decius, and P. C. Cross, Molecular Vibrations (The Theory of Infrared and Raman Vibrational Spectra), Dover Publications, Inc. New York, 1955.

[203] B. R. Jones, P. A. Varughese, I. Olejniczak, J. M. Pigos, J. L. Musfeldt, C. P. Landee, M. M. Turnbull, and G. L. Carr, Chem. Mater. **13**, 2127 (2001).

[204] J. Choi, J. D. Woodward, J. L. Musfeldt, C. P. Landee, and M. M. Turnbull, Chem. Mater. **15**, 2797 (2003).

[205] We note that ^{1}H NMR is also an excellent probe of hydrogen bonding strengths, as demonstrated for the $W_6S_8L_6$ clusters (where L is a pyridine-based ligand) [206].

[206] C. M. Oeretel, R. D. Sweeder, S. Patel, C. M. Downie, and F. J. DiSalvo, Inorg. Chem. **44**, 2287 (2005).

[207] M. Kajňaková, M. Orendáč, A. Orendáčová, A. Vlček, J. Černák, O. V. Kravchyna, A. G. Anders, M. Bałanda, J. -H. Park, A. Feher, and M. W. Meisel, Phys. Rev. B **71**, 014435 (2005).

[208] S.A. Baudron, P. Batail, C. Coulon, R. Clérac, E. Canadell, V. Laukhin, R. Melzi, P. Wzietek, D. Jérome, P. Auban-Senzier, and S. Ravy, J. Am. Chem. Soc. **127**, 11785 (2005).

[209] K. Morikawa, T. Mizokawa, K. Kobayashi, A. Fujimori, H. Eisaki, S. Uchida, F. Iga, and Y. Nishihara, Phys. Rev. B **52**, 13711 (1995).

[210] A. Vimont, J.-M. Goupil, J.-C. Lavalley, M. Daturi, S. Surblé, C. Serre, F. Millange, G. Férey, and N. Audebrand, J. Am. Chem. Soc. **128**, 3218 (2006).

[211] A. P. Monkman, L.-O. Pålsson, R. W. T. Higgins, C. Wang, M. R. Bryce, A. S. Batsanov, and J. A. K. Howard, J. Am. Chem. Soc. **124**, 6049 (2002).

[212] A. Dey, T. Okamura, N. Ueyama, B. Hedman, K. O. Hodgson, and E. I. Solomon, J. Am. Chem. Soc. **127**, 12046 (2005).

[213] J. H. Jung, H. J. Lee, T. W. Noh, E. J. Choi, Y. Moritomo, Y. J. Wang, and X. Wei, Phys. Rev. B **62**, 481 (2000).

[214] J. H. Jung, H. J. Lee, T. W. Noh, Y. Moritomo, Y. J. Wang, and X. Wei, Phys. Rev. B **62**, 8634 (2000).

[215] Y. Okimoto, Y. Tomioka, Y. Onose, Y. Otsuka, and Y. Tokura, Phys. Rev. B **57**, R9377 (1998).

[216] Y. Okimoto, Y. Tomioka, Y. Onose, Y. Otsuka, and Y. Tokura, Phys. Rev. B **59**, 7401 (1999).

[217] T. Ishikawa, T. Kimura, T. Katsufuji, and Y. Tokura, Phys. Rev. B **57**, R8079 (1998).

[218] H. J. Lee, K. H. Kim, J. H. Jung, T. W. Noh, R. Suryanarayanan, G. Dhalenne, and A. Revcolevschi, Phys. Rev. B **62**, 11320 (2000).

[219] A. Moreo, S. Yunoki, and E. Dagotto, Phys. Rev. Lett. **83**, 2773 (1999).

[220] Z. Sun, Y. -D Chuang, A. V. Fedorov, J. F. Douglas, D. Reznik, F. Weber, N. Aliouane, D. N. Argyriou, H. Zheng, J. F. Mitchell, T. Kimura, Y. Tokura, A. Revcolevschi, and D. S. Dessau, arXiv:cond-mat/0510255 v1, 10 Oct 2005.

[221] N. Mannella, W. L. Yang, X. J. Zhou, H. Zheng, J. F. Mitchell, J. Zaanen, T. P. Devereaux, N. Nagaosa, Z. Hussain, and Z.-X. Shen, Nature **438**, 474 (2005).

[222] Y.-D. Chuang, A. D. Gromko, D. S. Dessau, T. Kimura, and Y. Tokura, Science **292**, 1509 (2001).

[223] D. B. Romero, V. B. Podobedov, A. Weber, J. P. Rice, J. F. Mitchell, R. P. Sharma, and H. D. Drew, Phys. Rev. B **58**, R14737 (1998).

[224] Y. Nakanishi, K. Shimomura, T. Kumagai, M. Matsukawa, M. Yoshizawa, M. Apostu, R. Suryanarayanan, A. Revcolevcschi, and S. Nakamura, (unpublished).

[225] L. M. Rodriguez-Martinez and J. P. Attfield, Phys. Rev. B **54**, R15622 (1996).

[226] E. Pollert, S. Krupička, and E. Kuzmičová, J. Phys. Chem. Solids **43**, 1137 (1982).

[227] R. D. Shannon, Acta Crystallogr. Sec. A **32**, 751 (1976).

[228] J. Burgy, M. Mayr, V. Martin-Mayor, A. Moreo, and E. Dagotto, Phys. Rev. Lett. **87**, 277202 (2001).

[229] E. Dagotto, Science **309**, 257 (2005).

[230] J. Choi, J. D. Woodward, J. L. Musfeldt, J. T. Haraldsen, X. Wei, M. Apostu, R. Suryanarayanan, and A. Revcolevschi, Phys. Rev. B **70**, 064425 (2004).

[231] C. dela Cruz, F. Yen, B. Lorenz, Y. Q. Wang, Y. Y. Sun, M. M. Gospodinov, and C. W. Chu, Phys. Rev. B **71**, R060407 (2005).

[232] T. Goto, T. Kimura, G. Lawes, A. P. Ramirez, and Y. Tokura, Phys. Rev. Lett. **92**, 257201 (2004).

[233] J. D. Woodward, J. Choi, J. L. Musfeldt, J. T. Haraldsen, X. Wei, H. -J. Koo, D. Dai, M. -H. Whangbo, C. P. Landee, and M. M. Turnbull, Phys. Rev. B **71**, 174416 (2005).

[234] R. S. Freitas, J. F. Mitchell, and P. Schiffer, Phys. Rev. B **72**, 144429 (2005).

[235] Y. Shiotani, J. L. Sarrao, and G. -Q. Zheng, Phys. Rev. Lett. **96**, 057203 (2006).

[236] H. Qin, J. Hu, J. Chen, Y. Wang, and Z. Wang, J. Appl. Phys. **91**, 10003 (2002).

[237] G. M. B. Castro, A. R. Rodrigues, F. L. A. Machado, A. E. P. de Araujo, R. F. Jardim, and A. K. Nigam, J. Alloys and Compounds **369**, 108 (2004).

Vita

Jinbo Cao was born in Huadian City, Jilin Province, China. He attended University of Science and Technology of China in Anhui between 1997 and 2002, where he received B.S. degrees majoring in Chemistry and Computer Science. In August 2002, he enrolled as a graduate student at the Chemistry Department of the University of Tennessee, Knoxville. He joined Dr. Janice Musfeldt's group to begin research in the field of spectroscopic investigations of complex transition metal oxides. Jinbo Cao received a Doctor of Philosophy Degree in Chemistry from the University of Tennessee in May 2007.